TRANSFORMATION TOUGHENING IN PHOSPHOCARBIDE-STRENGTHENED AUSTENITIC STEELS

BY

CHUNE-CHING YOUNG

B. S., NATIONAL TAIWAN UNIVERSITY, TAIWAN, R. O. C.
(1975)
M. S., NATIONAL TAIWAN UNIVERSITY, TAIWAN, R. O. C.
(1977)

Submitted to the Department of
Materials Science and Engineering
in Partial Fulfillment of the Requirement of
the Degree of

DOCTOR OF PHILOSOPHY

at the
MASSACHUSETTS INSTITUTE OF TECHNOLOGY
May 1988

Signature of Author ______________________________
Department of Materials Science and Engineering
April 29, 1988

Certified by ______________________________
Dr. Gregory B. Olson
Thesis Supervisor

Certified by ______________________________
Professor Morris Cohen
Thesis Supervisor

Accepted by ______________________________
Professor John B. Vander Sande
Chairman, Departmental Committee on Graduate Studies

TRANSFORMATION TOUGHENING IN PHOSPHOCARBIDE-STRENGTHENED AUSTENITIC STEELS

by

Chune-Ching Young

Submitted to the Department of Materials Science and Engineering on April 29,1988 in partial fulfillment of the requirements for the degree of Doctor of Philosophy in Metallurgy

ABSTRACT

The influence of deformation-induced martensitic transformation on mechanical behavior is studied in two novel metastable austenitic steels with compositions 16Cr-10Ni-(0.5,3.5)Mn-0.3C-0.33P prepared by rapid solidification. Reduced lattice misfit between the austenite and carbide with the incorporation of phosphorus results in the precipitation of uniformly dispersed coherent phosphocarbide particles, $(CrFeP)_{23}C_6$, with diameter less than 80Å. The austenitic matrix can be effectively strengthened up to a yield stress of 1250 Mpa at room temperature. Properly selected aging treatments significantly alter the transformational volume change ($\Delta V/V_\gamma$) and the hardness difference (ΔH_v) between α' and γ phases at a given γ-phase strength level. This provides an opportunity to study the contributions of $\Delta V/V_\gamma$ and ΔH_v in the enhancement of ductility and toughness by deformation-induced martensitic transformation.

Compressive, tensile, and fracture toughness tests using the single-specimen J-integral technique were performed in the temperature range of -196°C to 300°C for the evaluation of mechanical properties and transformation kinetics. Although alumina contamination introduced during the rapid solidification processing limits the toughness of the parent phase (J_{IC}=50 ~ 75 KJ/m^2), the transformation can increase J_{IC} by 100 to 120 KJ/m^2 in both underaged and overaged alloys.

A quantitative rationale for the uniform and fracture strains of the overaged 0.5Mn alloy is obtained by calculating the influence of strain-induced transformation on the strain-hardening rate and applying suitable criteria governing the onset of flow instability and void-softening-induced shear localization. Good agreement between the predicted and the observed values was found. A higher strain-hardening rate accompanying the transforming alloy delays the occurrence of necking and ductile fracture.

The ductility enhancement depends on the shape of strain-hardening rate vs. plastic strain and is mainly controlled by the transformation kinetics. Maximum enhancement corresponding to the optimum transformation rate exists at a certain temperature. Compared to the effect of dilatation, the hardness difference provides most of the ductility enhancement under the moderate triaxiality encountered in the tensile test.

The enhancement of fracture toughness is found to be proportional to the third power of the transformation volume change according to measurements of transformation zone height. Both dilatation and hardness difference can be important in transformation toughening. For a given alloy, dilatation becomes more important as triaxiality increases . For example, in the case of the overaged 0.5Mn alloy, dilatation contributes only 30% of the fracture- strain enhancement, but 83% of toughness increment. Using this analysis, the potential highest ΔJ_{Ic} of the studied alloy is expected to reach 325 KJ/m^2 if not circumvented by intergranular fracture.

Microstructural observation using TEM after tensile deformation further confirms the benefit of transformation in retarding the microscopic processes of ductile fracture. Microvoid formation is suppressed even after severe deformation due to the formation of fine martensitic laths preferentially at the interfaces of alumina particles.

Thesis Supervisor : Dr. Gregory B. Olson
Title : Senior Research Associate

Thesis Supervisor : Dr. Morris Cohen
Title : Institute Professor, Emeritus

Table of Contents

Chapter Page

Title Page---------- 1

Abstract---------- 2

Table of Contents---------- 4

List of Figures---------- 6

List of Tables---------- 13

Acknowledgements---------- 14

1. Introduction---------- 15

2. Literature Review
   - 2-1. Deformation-Induced Martensite and Transformation Plasticity---------- 18
     - 2-1-1. Stress-Assisted vs. Strain-Induced Transformation---------- 18
     - 2-1-2. Transformation Kinetics and Constitutive Relations---------- 20
     - 2-1-3. Enhancement of Ductility and Toughness---------- 28
   - 2-2. Ductile Fracture and Shear Instability---------- 31

3. Preparation of Materials
   - 3-1. Chemical Composition---------- 37
   - 3-2. Alloy Preparation---------- 38
   - 3-3. Solution Treatment---------- 42
   - 3-4. Warm-Rolling and Aging Treatment---------- 48
   - 3-5. Hardness Difference and Transformation Volume Change---------- 55

4. Experimental Procedures
   - 4-1. Mechanical Testng---------- 58
     - 4-1-1. Uniaxial Tensile Tests---------- 58
     - 4-1-2. Fracture Toughness Tests---------- 59
     - 4-1-3. Uniaxial Compressive Tests---------- 66
     - 4-1-4. Microhardness Measurements---------- 67
   - 4-2. Transformation Kinetics Measurements---------- 67

Chapter Page

4-3. Microscopy---69

5. Results and Discussions
5-1. Microstructure Characterization---72
5-2. Transformation Stability---89
5-2-1. Temperature Dependence of Yield Stress and Transformation Temperature---89
5-2-2. Transformation Kinetics---105
5-3. Mechanical Behavior and Deformation-Induced Martensitic Transformation
5-3-1. Tensile Properties---119
a. Overaged Alloy---119
b. Underaged Alloys---123
c. Tensile Fracture---126
5-3-2. Fracture toughness---132
a. J_{Ic} and Transformation Morphology---132
b. Temperature Dependence of $dJ/d\Delta a$---142
5-3-3. Quantitative Assessment of Ductility---148
a. Flow Relations---148
b. Criteria for Plastic-Flow Instability and Shear-Instability-Controlled-Fracture---155
c. Predicted Uniform Strain and Fracture Strain-159
d. Microstructure Evidence of Transformation in Delaying Void-Formation---164
5-3-4. Roles of Strength Difference and Dilatation in the Transformation Toughening---171

6. Conclusions---182

7. Recomendations for Future Research---185

References---187

Biographical Note---194

List of Figures

Figure	Caption	Page
2-1	Schematic representation of interrelationships between stress-assisted and strain-induced martensitic transformation [3].	19
2-2	Comparison of calculated and observed true stress-strain curves for a high strength TRIP steel when stress-assisted transformation occurs [26].	23
2-3	Derivation of the Narutani flow relation for strain-induced transformation [30].	27
2-4	Ductility and toughness enhancements in γ'-strengthened metastable auetente [1].	27,30
2-5	Schematic processes of crack growth [41].	32
3-1	Schematic representation of the Pratt and Whitney centrifugal atomization unit [57].	39
3-2	Optical micrographs of 0.5Mn rapidly solidified powders, showing fine solidification structure and presence of porosity	41
3-3	SEM micrograph of the as-extruded 0.5Mn alloy and x-ray spectra from the matrix and chromium carbides.	43
3-4	Optical micrograph showing carbide dissolution, grain growth and void-formation occurred during solution treatment at high temperature.	45
3-5	SEM fractograph of the 0.5Mn alloy without warm-rolling, showing intergranular fracture caused by helium bobbles.	47
3-6	Hardness distribution in the thickness direction of a warm-rolled bar before and after aging.	49
3-7	Metallograph of the warm-rolled 0.5Mn alloy. Pores formed during 1150°C/2hr solution treatment were successfully closed.	51

3-8 Aging behavior of the warm-rolled alloys, and the selected aging conditions. a). 0.5Mn alloy, b). 3.5Mn alloy. 53,54

4-1 Schematic diagram of temperature control setup in tensile test. 60

4-2 Dimensions and shape of tensile specimen. 61

4-3 Arrangement of electric cords used to heat the specimen during fatigue precracking. 63

4-4 Dimensions and shape of three-point bend specimen for J_{Ic} test. 64

5-1 TEM micrographs illustrating the general matrix precipitation in the 0.5Mn alloy, solution treated at 1150°C for 2 hours and aged at 680°C for 14 hours. a). Bright-field image, b). Dark-field image of phophocarbides, c). and d). are diffraction pattern and its indexing. 73

5-2 TEM micrograph showing plate-like carbide precipitates in the 0.5Mn alloy, solution treated at 1150°C for 2 hours and aged at 680°C for 14 hours. 74

5-3 Microstructure of the solution treated and warm-rolled 0.5Mn alloy showing the presence of shear bands and high-density dislocations. 74

5-4 No precipitate -free zones were found in the vicinity of grain-boundaries in the overaged 0.5Mn alloy. 77

5-5 TEM micrographs showing the morphology and distribution of carbide precipitates in the underaged 3.5Mn alloy. a). Bright-field image, c). Dark-field image of phophocarbides, b). and d). are diffraction pattern and its indexing. 78

5-6 TEM micrographs showing the morphology and distribution of carbide precipitates in the underaged 0.5Mn alloy. a). Bright-field image, b). Dark-field image of phophocarbides, c). and d). are diffraction pattern and its indexing. 80

5-7 a). SEM secondary electron image recorded from an electro-polished surface of the 0.5Mn-O alloy, showing the distribution of grain refining alumina particles with diameter 0.1 to 0.5 μm. b). x-ray spectrum of particles. 85

5-8 TEM micrographs identify the structure of grain refining particles as α-Al_2O_3. a). Bright-field image, b). Dark-field image of α-Al_2O_3 particle, c). and d). are SADP and its indexing. 86

5-9 SEM secondary electron image showing alumina colony in the 0.5Mn-O alloy. 87

5-10 Temperature dependence of 0.2% tensile yield stress of the 3.5Mn-U, 0.5Mn-U, and 0.5Mn-O alloys at a strain rate of 0.02 min^{-1}. 91

5-11 Comparison of temperature dependence of yield stress in tension and compression tested at the same strain rate of 0.02 min^{-1}. Yield stresses below M_s^σ at lower strain rate 0.0002 min^{-1} are also indicated. 93

5-12 M_s^σ temperature in a tensile neck (M_s^σ(N)) is determined from the extrapolation of M_s^σ(UT) and M_s^σ(UC) by calculating the stress-state corresponding to the fracture strain. 96

5-13 Temperature dependence of chemical free-energy (ΔG_{ch}) and critical free energy (ΔG_{crit}) at strain rates of 0.02 and 0.0002 min^{-1} for the 0.5Mn-O alloy. 99

5-14 Observed temperature dependence of tensile yield stress and Calculated stress for the stress-assisted transformation for the 0.5Mn-O alloy at two strain rates. 103

5-15 Calculated transformation stress and measured yield stress for the 0.5Mn-O alloy under different stress-states. 104

5-16 Transformation curves for the 0.5Mn-O alloy in uniaxial compression. 107

5-17 Transformation curves for the 0.5Mn-O alloy in uniaxial tension. 108

5-18 Morphology of martensite transformed below M_S^σ temperature in tension and compression. 110

5-19 Typical morphology of the strain-induced martensite formed at 65°C in tension. 111

5-20 The α-parameter obtained by fitting the transformation curves of the 0.5Mn-O alloy to the Olson-Cohen model. 114

5-21 Temperature dependence of the β-parameter in tension and compression obtained by fitting the transformation curves of the 0.5Mn-O alloy to the Olson-Cohen model. 115

5-22 All values of the β-parameter are plotted vs. temperature interval, T-M_S^σ, and form a single exponential curve. 116

5-23 Temperature dependence of theuniform and fracture plastic strains for the 0.5Mn-O alloy along with the relevant transfomation temperatures. The estimated fracture strain of austenite is also shown. 121

5-24 Temperature dependence of the uniform and fracture plastic strains for the 0.5Mn-U an 3.5Mn-U alloys along with the relevant transformation temperatures. 125

5-25 Mixed fracture mode in the 0.5Mn-O alloy tested at -6°C in tension. 127

5-26 Dimpled rupture in the 0.5Mn-O alloy tested at 65°C in tension. The specimen failed by shear on a plane with 45° to the loading axis. 128

5-27 Delamination occurred in the 0.5Mn-O alloy tested at 115°C in tension. Elongated dimples are found in the high magnification micrograph. 129

5-28 Typical cup-and-cone fracture surface with dimpled topography in the 0.5Mn-O alloy tested at 250°C in tension. 130

5-29 Equiaxed alumina particles are commonly found to sit in the dimples. 133

5-30 J values vs. crack extension at various temperatures. a). 0.5Mn-O alloy, b). 0.5Mn-U alloy, c). 3.5Mn-U alloy. 134

5-31 Temperature dependence of fracture toughness J_{Ic} for the 0.5Mn-O, 0.5Mn-U, and 3.5Mn-U along with the transformation temperatures. 139

5-32 Fracture toughness of the austenitic phase estimated from the measured J_{Ic} values of the 3.5Mn-U alloy above M_d. 140

5-33 Enhancement of fracture toughness vs. temperature interval , $T-M_s^{\sigma}$. 141

5-34 Optical micrograph showing a large amount of plate martensite in the vicinity of crack, extended during bend test for the 0.5Mn-O alloy at -30°C. 143

5-35 Lath martensite formed around the crack in the 0.5Mn-O alloy during bend test at 125°C. 144

5-36 Only few martensitic laths are found in a very small region around a crack in the 0.5Mn-O alloy tested 200°C. 145

5-37 Temperature dependence of dJ/dΔa. 147

5-38 Compressive true stress-strain curves of the austenite and martensite of the 0.5Mn-O alloy at 160°C. 150

5-39 Temperature dependence of 0.2% compressive yield stress of the martensite and austenite of the 0.5Mn-O alloy. 152

5-40 The observed true stress-strain curve of the 0.5Mn-O alloy at 65°C is fitted to the Narutani relation. The strain-hardening rate is also calculated from the fitted curve. 154

5-41 Normalized strain-hardening rate vs. plastic strain at θ=0.6 and 1 for a γ'-strengthened steel 31Ni(L) along with the criteria for necking and void-softening-induced shear localization demonstrates the predictions of uniform and fracture strains. 156

5-42 The effect of triaxiality increment due to necking on the transformation curves of the 0.5Mn-0 alloy at 65, 115, and 150°C. 160

5-43 The calculated values of the normalized strain-hardening rate for the 0.5Mn-0 alloy at temperatures from 100 to 250°C. Fracture strains are predicted from the intersection of each h/σ curve and a critical $(h/\sigma)_C$ curve defined the onset of shear localization. 161

5-44 Comparison of the predicted and observed temperature dependence of uniform and fracture strains for the 0.5Mn-0 alloy. 163

5-45 The contour of thr tensile neck becomes less localized due to the deformation-induced martensitic transformation. a). 0.5Mn-0 alloy at 115°C, b). 0.5Mn-0 alloy at 250°C. 165

5-46 TEM micrographs showing the preferential formatiom of martensite around an alumina particle in the tensile deformed 0.5MN-0 alloy (ε_{pu}=0.09 at 115°C) with 0.029 martensite volume fraction. a). Bright-field image, b). Dark-field image of martensite, c). and d). are SADP and its analysis. 168

5-47 Directional martensitic laths formed between two alumina particles. The foil with about 0.15 martensite volume fraction was cut from a tensile neck of the 0.5Mn-0 alloy tested at 150°C along the loading axis. 169

5-48 Void-formation was found at the interface of an alumina particle in the 0.5Mn-0 alloy with high martensite volume fraction (0.75). a). Bright-field image, b). Dark-field image of martensite, c). and d). are SADP and its analysis. 170

5-49 Optical micrograph revealing the martensitic transformation near the crack initiation position of 3.5Mn-U bend tested at 0ºC is used to demonstrate the measurement of transformation-zone height. 173

5-50 Half-height of transformation zone vs. nondimensional temperature, θ. 175

5-51 Half-height of transformation zone vs. J increment (=J-$J_{aust.}$) corresponding to a very small crack extension (=2J_{Ic}/1.6σ_y). a). phosphocarbide-strengthed steels, b). γ'-strengthed steels. 177

5-52 Slopes of half-height of transformation zone vs. J increment lines are plotted vs. transformation volume change for both high-ΔHv and low-ΔHv alloys, and fitted to power equations. 178

List of Tables

Table	Caption	Page
3-1	Chemical Compositions of Alloys.	38
3-2	Effect of Solution Treatment.	46
3-3	Hardness Difference and Transformation Volume Change.	57
5-1	Composition and Lattice Parameter of Carbide.	82
5-2	Transformation Temperatures.	98
5-3	Transformation Kinetic Data and Fitting Parameters.	106
5-4	Tensile Properties.	120
5-5	Predicted Temperatures Corresponding to the Peak Uniform and Fracture Strains of the Underaged Alloys.	124
5-6	Fracture Toughness J_{Ic} and Slopes $dJ/d\Delta a$	136
5-7	Half-Height of Transformation Zone, J Increment, and Nondimensional Temperature.	174
5-8	Contributions of Hardness Difference and Dilatation to Toughness Enhancement.	180

ACKNOWLEDGEMENTS

I would like to express my deepest appreciation to Dr. Gregory Olson and Prof. Morris Cohen for their guidance and support throughout my tenure in M.I.T. Without their invaluable advice and constant encouragement, this research in the potentially embrittling alloy would not have been possible. Their kindness and friendship helped me get through the most difficult times in M.I.T.

I am grateful to Prof. Walter Owen and Prof. David Parks for serving on my thesis committee and for their helpful criticisms and suggestions.

A special thanks to Ms. Marge Meyer for her assistance in solving so many administrative problems and her encouragement given to me. Sincere appreciation is extented to many working in the Olson/Cohen's research group including; Dr. Dennis Haezebrouck for helpful discussions in many aspects of martensitic transformation; Ms. Yin-Lin Xie and Mrs. Mim Rich for laboratory support in the early stage of mechanical testing and heat treatments; Dr. John Watton for valuable discussions in the areas of rapid solidification processing; Dr. Fu-Rong Chen for assistance in electron microscopy; Messrs. Mark Gore, Greg Haidemenpolous, Frode Stavehaug and Min-Fa Lin for technical and non-technical conversations.

Thanks to the Chun-Shan Institute of Science and Technology for the generous financial support of my graduate education at M.I.T. and to D.O.E. for support the research project. Additional gratitude is given to Dr. Shu-En Hsu, adviser of my graduate study at N.T.U., for his support and several visitings.

The occasional group meetings at Eastgate on Saturday evening with Chinese fellows Messrs. Jeng-Yih Juang, YuangChing Chou, Pin-Hu Kao, and Yu-Hao Huang provided a necessary contribution to the success of this work.

Very special appreciation is given to my wife, Mara, for her unending love, support, patience, and encouragement throughout the years and distance. This thesis is dedicated to her.

Chapter I. Introduction

The influence of deformation-induced martensitic transformation on the mechanical behavior of two rapidly solidified austenitic steels with compositions 16Cr-10Ni-(0.5, and 3.5)Mn-0.3C-0.33P are studied in this work. The selection of these novel compositions originated from an initial attempt to develop a high-strength metastable austenitic steel (yield stress >180 ksi) without applying a severe warm-working operation that greatly limits the commercial application of TRIP steels. Alternatively, precipitation hardening is another way to achieve such high strength. In addition to γ'-$Ni_3(Ti,Al)$ precipitates, as commonly used to strengthen Ni-base superalloys and also applied to austenitic steels with high Ni content [1], carbide precipitation is another choice. In the 300-series austenitic stainless steels, widely dispersed $M_{23}C_6$ carbides with particle sizes in tenths μm normally tend to precipitate along grain boundaries. They are not effective in strengthening unless refined and uniformly distributed. Until the late 1960s, Banerjee et al. [2] found that the addition of phosphorus in 18-8 stainless steels can decrease the lattice parameter of $M_{23}C_6$ carbide and improve the lattice matching between the matrix and carbide phases. The reduced misfit favors the matrix nucleation of coherent phosphocarbides during aging and hence results in the formation of finely dispersed precipitates with a diameter of ~200Å. A hardness of Rc47 was reported [2] for the high phosphorus-containing austenitic steel after solution and aging treatments. The strength of this alloy system seems to meet our requirement.

The system is also of interest from the standpoint of another principal purpose of this work, exploring the influence of dilatation ($\Delta V/V_\gamma$) and hardness difference (ΔH_V) between the austenite and martensite on the enhancement of ductility and toughness due to transformation. These two parameters can be controlled by adjusting the alloy content of the matrix, carbon in particular, through aging treatments. However, phosphorus is a well-known embrittling impurity in high strength steels and has a strong tendency for microsegregation during solidification, and so a rapid solidification process is necessary to minimize the inhomogeneity of chemical composition. RSP material also allows a high temperature solution treatment without causing severe grain-coarsening due to the pinning effect of very finely dispersed inclusion particles such as oxysulfides or oxides. Both fine grain size and uniform composition are beneficial for avoiding brittle intergranular fracture.

In this study, the phosphocarbide-strengthened steels are suitably aged to reach a preset hardness, but with different values of $\Delta V/V_\gamma$ (2.69 to 5.08%) and ΔH_V (H_V 46 to 90). Not only are the temperature dependence of mechanical properties (strength, ductility, and toughness) measured for all the aged coditions, but also the transformation kinetics and the flow relations of the austenite and martensite for the overaged 0.5Mn alloy. The latter findings are then used to calculate the constitutive relations and hence the strain-hardening rates of the transforming alloy in the temperature regime at which the strain-induced transformation dominates. Combining the strain-hardening curves and suitable criteria for flow instability and void-softening-induced shear localization, the enhancement of uniform and fracture strains, including the effect of dilatation, at various temperatures are predicted. Microstructural characterization has been also determined for these RSP alloys before and after tensile testing to explain the fracture behavior and to further understand the benefit of transformation in retarding the microscopic processes of ductile fracture. The contributions of $\Delta V/V_\gamma$ and ΔH_V to the enhancement of fracture toughness are empirically estimated from the observed transformation-zone height, including previous results of some γ'-strengthened alloys [1].

This overall research aims to provide a more quantitative interpretation of the relationships between mechanical properties and deformation-induced martensitic transformation, and can be regarded as providing the experimental foundation for further analysis through continuum-mechanics modeling.

Chapter 2 Background and Literature Review

2-1. Deformation-Induced Martensitic Transformation and Transformation Plasticity

2-1-1. Stress-Assisted vs. Strain-Induced Transformation

It has been well-known that the formation of martensite can be stimulated by elastic and/or plastic deformation. According to the schematic stress-temperature diagram in Fig.2-1, two types of deformation-induced martensitic transformation -- stress-assisted and strain-induced -- can be distinguished [3,4]. On cooling below M_s, the free energy difference between martensite and austenite is sufficiently large to trigger the operation of the pre-existing nucleation sites and martensite starts forming spontaneously. At temperatures between M_s and M_s^{σ}, elastic stress (strain) is required to initiate the nucleation of martensite at the same sites responsible for the spontaneous transformation. This is called the stress-assisted transformation and initial yielding is controlled by the macroscopic plastic strain associated with the transformation. At the M_s^{σ} temperature, the stress required for nucleation reaches the yield stress of the parent phase and starts to cause plastic deformation by slip. Since the plastic deformation can introduce more potent sites for nucleation, the required stress between M_s^{σ} and M_d is much lower than that of the stress-assisted nucleation (extension of line AB) and follows line BC in Fig.2-1. This nuceation is termed strain-induced. At temperatures above M_d, the nucleation can not be induced by plastic deformation because of the small chemical driving force. As experimentally demonstrated by Leal [1], both

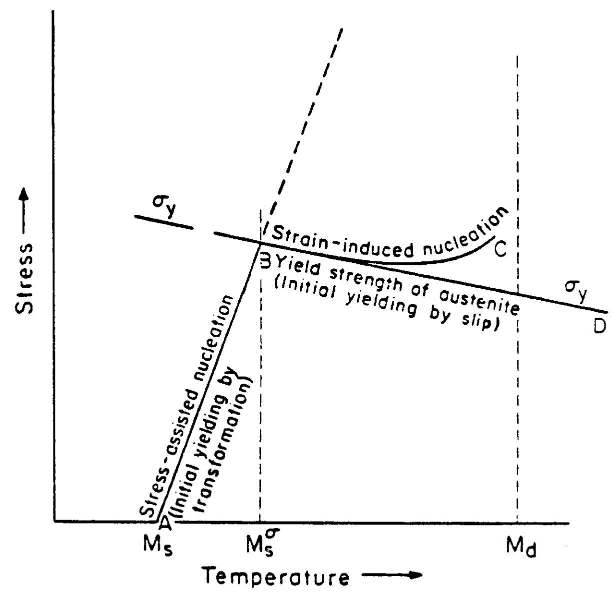

Fig.2-1. Schematic representation of interrelationships between stress-assisted and strain induced martensitic transformation [1].

the M_s^σ and M_d temperatures of a given metastable austenitic steel change with stress-state. Although the origin of the nucleation site need not influence the martensitic morphology, the plastic flow by slip in the strain-induced regime certainly inhibits the martensitic growth and the morpholgy is changed. In general, the stress-assisted martensite has a fairly coarse plate morphology, while the strained-induced martensite shows a much finer lath morphology formed at the shear-band intersections [5,6].

2-1-2. Transformation Kinetics and Constitutive Relations

When the martensitic transformation occurs under stress, a macrosopic strain, termed transformation plasticity, accompanies the transformation. Transformation plasticity arises from stress biasing of the accomodation plastic flow which takes place around the martensitic plates, triggered by both the volume change and the transformation shear, and from the martensitic transformation shape strain as a results of stress biasing of the martensitic-plate variants [7]. Utilizing the beneficial influence of macroscopic strain, ultrahigh strength metastable austenitic steels, named TRIP steels (TRansformation-Induced-Plasticity), were developed by Zackay et al. [8]. At temperatures below the M_d temperature, enhancement in ductility [8-14], fracture toughness [15-19], and resistance of fatigue crack growth [20-22] has been observed in TRIP steel, but is strongly temperature-dependent. In order to analyze the resulting mechanical properties, transformation kinetics and the influence of deformation-induced martensitic transformation on the flow behavior of metastable austenite have to be understood [5].

Stress-Assisted Transformation

When the transformation is entirely stress-assisted, the plastic strain only results from the macroscopic strain associated with martensitic transformation because the imposed stress is lower than the yield stress of austenite. In this case, the martensite volume fraction, $f_{\alpha'}$, is linearly proportional to the measured plastic strain, ε_p, i.e. $f_{\alpha'} = k\ \varepsilon_p$. The measurements of both $f_{\alpha'}$ and ε_p in a TRIP steel [5] has verified this relation at temperature far below M_s^{σ}.

Based on the well-established kinetics of isothermal martensitic nucleation and the thermodynamic effect of applied stress, the stress-strain relation in the stress-assisted temperature regime has been derived [26]. Since the kinetics of isothermal martensitic transformation is controlled by nucleation, the rate of transformation can be expressed as an exponential function of activation energy (Q), which is linearly related to the applied driving force (ΔG) as indicated by kinetic experiments [23,24] :

$$\begin{aligned} \dot{f}_{\alpha'} &= n_s V \nu \exp(-Q/RT) \\ &= n_s V \nu \exp[-(A+B\Delta G)/RT] \qquad (2\text{-}1) \end{aligned}$$

where n_s is the density of nucleation sites, V is the instantaneous martensitic mean volume, ν is the nucleation-attempt frequency, A and B are constants. The density of nucleation sites varies with progress of the transformation and is described as [23,24] :

$$n_s = (n_i + p f_{\alpha'} - N_v)\,(1 - f_{\alpha'}) \qquad (2\text{-}2)$$

where n_i is the initial density of nucleation site, p is autocatalytic factor, and N_v is the number of martensitic plates per unit volume. In the case of the stree-assisted transformation, the driving force (ΔG) must take into account both the chemical free-energy change (ΔG_{ch}) and the thermodynamic effect of applied stress (ΔG_{mech}) . Adopting the Patel and Cohen analysis [25], the thermodynamic contribution per unit stress ($\partial\Delta G/\partial\sigma$) can be calculated for the most favorably oriented martensitic plate and is regarded as a constant under a given stress-state. Substituting Eq.2-2 and $\Delta G_{mech} = \sigma\cdot(\partial\Delta G/\partial\sigma)$ into Eq.2-1, the flow stress during stress-assisted transformation can be expressed as :

$$\sigma(f_{\alpha'},\dot{f}_{\alpha'},T) = -(B\cdot\partial\Delta G/\partial\sigma)^{-1}\cdot\{A+B\Delta G_{ch}+RT \ln [f_{\alpha'} / ((n_i+p\dot{f}_{\alpha'}-N_v)(1-f_{\alpha'}) V_v)]\} \tag{2-3}$$

Substitution of $f_{\alpha'} = k\,\varepsilon_p$ then provides a flow relation $\sigma(\varepsilon_p,\dot{\varepsilon}_p,T)$. The shape of the $\sigma-\varepsilon_p$ curve is determined by the behavior of the denominator in the last term of Eq.2-3. The yield stress is controlled by n_i, a stress drop is produced by the $pf_{\alpha'}$ term, and the stress rises rapidly as the site is depleted. The calculated and observed true stress-strain curves for a TRIP steel [5] are compared in Fig.2-2, in which the flow stresses are well below the stress for the general yielding by slip. Eq.2-3 accurately predicts the initial stress drop which reflects the dynamic softening contribution of transformation plasticity. The curvature of the σ - ε_p curve at low strains thus changes to upward.

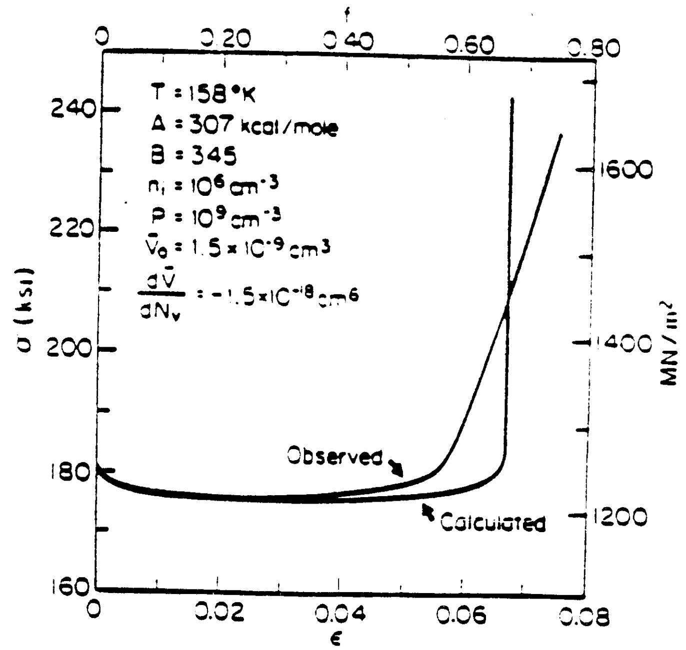

Fig.2-2. Comparison of calculated and observed stress-strain curves for high-strength TRIP steel when the stress-assisted transformation is dominant [26].

Strain-Induced Transformation

When the strain-induced transformation is dominant at temperatures above M_s^{σ}, the observed transformation curve ($f_{\alpha'}$ vs. ε_p) is sigmoidal in shape. Angel [27] proposed an equation of the log autocatalytic type, $\ln (x/1-x) = C \ln\varepsilon + D$, to fit the $f_{\alpha'}$ vs. ε_p curve of 18-8 stainless steel, where x represents the ratio $f_{\alpha'}/f_{\alpha',max.}$, ε is true strain, C and D are constants. On the other hand, Gerberich et al. [28] used a parabolic equation, $f_{\alpha'} = m\, e^{1/2}$, to describe the transformation kinetics of Ni-Cr-C TRIP steels, where e is engineering strain, and m is an index related to the austenite stability. Both equations can not accurately fit the kinetic data over a wide range of strain and are also lack of theoretical basis.

Olson and Cohen [29] developed a quantitative model for the strain-induced martensitic nucleation based on the fact that the intersections of shear bands are the dominant nucleation sites. They relate the volume fraction of shear bands, f^{sb}, to ε_p by assuming a constant rate of consumption of shear-band-free volume. This gives :

$$f^{sb} = 1 - \exp(-\alpha\, \varepsilon_p) \qquad (2\text{-}4)$$

where depends on stacking fault energy and strain rate. The number of shear band intersection, N_v^I, is related to the number of shear band, N_v^{sb}, by a simple power law :

$$N_v^I = K\, (N_v^{sb})^n \qquad (2\text{-}5)$$

where K and n are constants. The incremental number of martensitic embryo per unit austenite volume, $dN_V^{\alpha'}$, is then related to an increase in the number of shear-band intersection by :

$$dN_V^{\alpha'} = p\, dN_V^{I} \qquad (2\text{-}6)$$

where p is the probability that a shear-band intersection will form a martensite embryo. These assumptions lead to a relation to express the volume fraction of strain-induced martensite as a function of plastic strain :

$$f_{\alpha'} = 1 - \exp\{-\beta\,[1-\exp(-\alpha\varepsilon_p)]^n\} \qquad (2\text{-}7)$$

where n is a fixed exponent larger than 2, the α parameter is temperature dependent through the temperature dependence of stacking fault energy, and the β parameter ($=(v^{\alpha'})/(v^{sb})^n K\cdot p$, $v^{\alpha'}$ is the volume of a martensite plate, and v^{sb} is the average volume of shear band) is both temperature and triaxiality dependent through the dependence of the probability p on thermodynamic driving force, ΔG. Eq.2-7 predicts that the curve of volume fraction martensite as a function of strain has a sigmoidal shape, in agreement with the data of Angel [27].

In the strain-induced transformation regime, an empirical flow relation of a transforming alloy was derived by Narutani et al. [30]. Although much attention has been given to the static-hardening effect contributed by the stronger martensic phase forming during strain-induced transformation, careful comparison of stress-strain curves has demonstrated that the dynamic softening is also important [5]. As summarized in Fig.2-3, the measured true stress-strain curves of martensite, stable austenite, and metastable austenite are lebeled $\sigma_{\alpha'}$, σ_{γ}, and σ_{exp}, respectively. The RM curve is obtained from a simple rule of mixture using the $\sigma_{\alpha'}$, σ_{γ} data and the measure martensite volume fraction $f_{\alpha'}$. Because the transformation plasticity arising from biasing of the transformation shape-strain does not contribute to the strain in either phase, the RM curve represents an upper limit to the static-hardening behavior. A strain-corrected rule of mixture is then proposed to estimate the static-hardening effect, σ_S, by :

$$\sigma_S = [1 - f_{\alpha'}] \cdot \sigma_{\gamma}(\varepsilon_p - \alpha' \cdot f_{\alpha'}) + f_{\alpha'} \cdot \sigma_{\alpha'}(\varepsilon_p - \alpha' \cdot f_{\alpha'}) \tag{2-8}$$

where $\alpha' \cdot f_{\alpha'}$ corrects for the transformation shape-strain contribution to the measured total plastic strain ε_p. An upper limit of the coefficient α' can be measured fron the slope of the transformation line in the stress-assisted regime. As indicated in Fig.2-3, the stress difference ($\Delta\sigma_d$) between σ_S and σ_{exp} is considered as the consequence of dynamic softening. With a series of prestrain tensile testing, the ratio between $\Delta\sigma_d$ and σ_S was found to be linearly proportional to the slope of the corresponding transformation curve. This gives :

$$\Delta\sigma_d/\sigma_S = \beta' \cdot df_{\alpha'}/d\varepsilon_p \tag{2-9}$$

where the coefficient β' is assumed to be independent of temperature and plstic strain. Combining Eqs.2-8 and 2-9, the flow relation of metastable austenite in the temperature range of strain-induced transformation is given by :

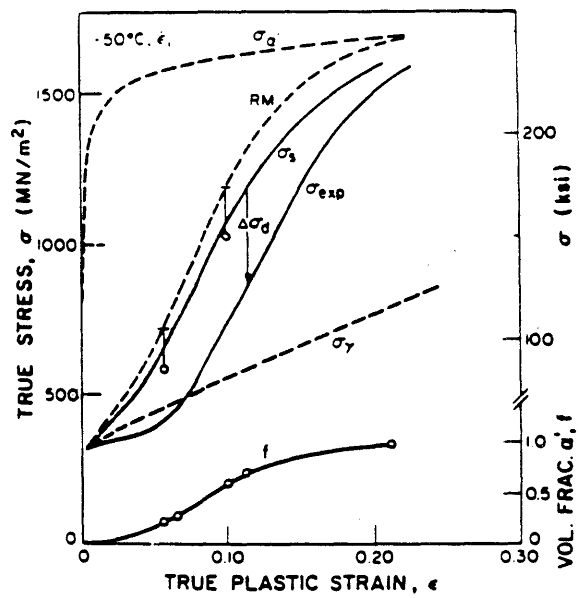

Fig.2-3. Experimental flow stress, σ_{exp}, and volume fraction martensite, f, vs plastic strain, ε, for metastable austenitic steel at −50°C, $\dot{\varepsilon}_1 = 2.2 \times 10^{-4}\ s^{-1}$. Dashed curves represent the stable austenite flow stress, σ_γ, the martensite flow stress, $\sigma_{\alpha'}$, and the prediction of the rule of mixtures for two-phase hardening, RM. Solid curve, σ_s, is prediction of strain-corrected rule-of-mixtures model.

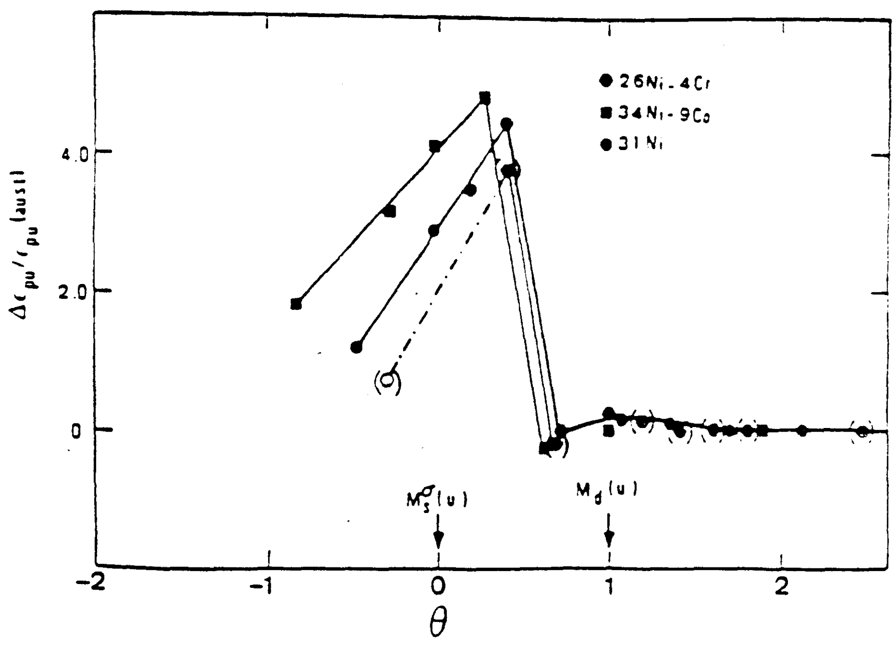

Fig. 2-4(a) Relative enhancement in uniform strain vs. nondimensional temperature θ for γ'-strengthened TRIP steels [1].

$$\sigma = \sigma_s - \Delta\sigma_d$$
$$=\{[1 - f_{\alpha'}] \cdot \sigma_{\gamma}(\varepsilon_p - \alpha' \cdot f_{\alpha'}) + f_{\alpha'} \cdot \sigma_{\alpha'}(\varepsilon_p - \alpha' \cdot f_{\alpha'})\} \cdot (1 - \beta' \cdot df_{\alpha'}/d\varepsilon_p) \quad (2\text{-}10)$$

Through the $f_{\alpha'}$-ε_p relation in Eq. 2-7, σ can be expressed as a function of ε_p, $\dot{\varepsilon}_p$, and T in the temperature range of strain-induced transformation. This provides the basis for a quantitative analysis of the mechanical behavior shown by metastable austenite above M_s^{σ} and will be applied in the present work.

2-1-3. Enhancement of Ductility and Toughness

The beneficial effect of deformation-induced martensitic transformation on the tensile ductility and fracture toughness of metastable austenite is well demonstrated by a recent study in a series of γ'-strengthened steels [1]. The increments of uniform elongation, fracture strain, and fracture toughness due to transformation are sensitive to the austenite stability which is represented by a normalized temperature, θ, as summarized in Fig.2-4(a)-(c). θ is defined as $[(T-M_s^{\sigma})/(M_d-M_s^{\sigma})]$ with M_d and M_s^{σ} measuring under the relevant stress-state. The position θ=0 corresponds to T=M_s^{σ}, while θ=1 corresponds to T=M_d.

A 3- to 4- fold increase in uniform elongation is obtained as compared to stable austenite and is qualitatively interpretated as a consequence of the curve-shaping effect of transformation. An optimum transformation stability corresponding to the peak increment in uniform elongation occurs between the M_s^{σ} and M_d tempertures in Fig.2-4(a). As can seen in Fig.2-4(b) and (c), an optimum transformation stability gives a substantial increment in ductility and toughness. However, the maxima in fracture strain and toughness take place at M_s^{σ} for the respective stress-states because of the brittleness of coarse stress-assisted martensite. In addition to the curve-shaping effect, reducing stress triaxiality by dilatation is also used to explain enhancement in fracture strain and toughness. Alloys with high volume change (lebeled Hv in Fig.2-4(b),(c)) correspond to higher increments in both fracture strain and toughness. An empirical relation shows that relative toughening increases linearly with volume change as the transformation amount around the crack tip is considered. Despite the strong temperature dependence of mechanical properties, excellent combination of toughness and strength ($K_{Ic,max.}$ = 255 Mpa·m$^{1/2}$ at a yield strength of 1300 Mpa) can be obtained via deformation-induced martensitic transformation in this alloy system.

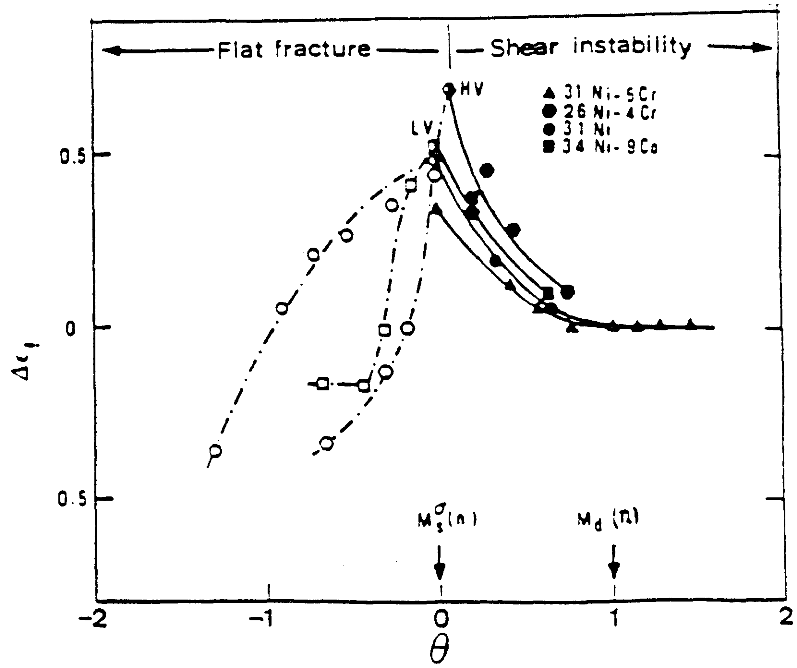

Fig. 2-4(b) Absolute enhancement in fracture strain vs. nondimensional temperature θ for γ'-strengthened TRIP steels [1].

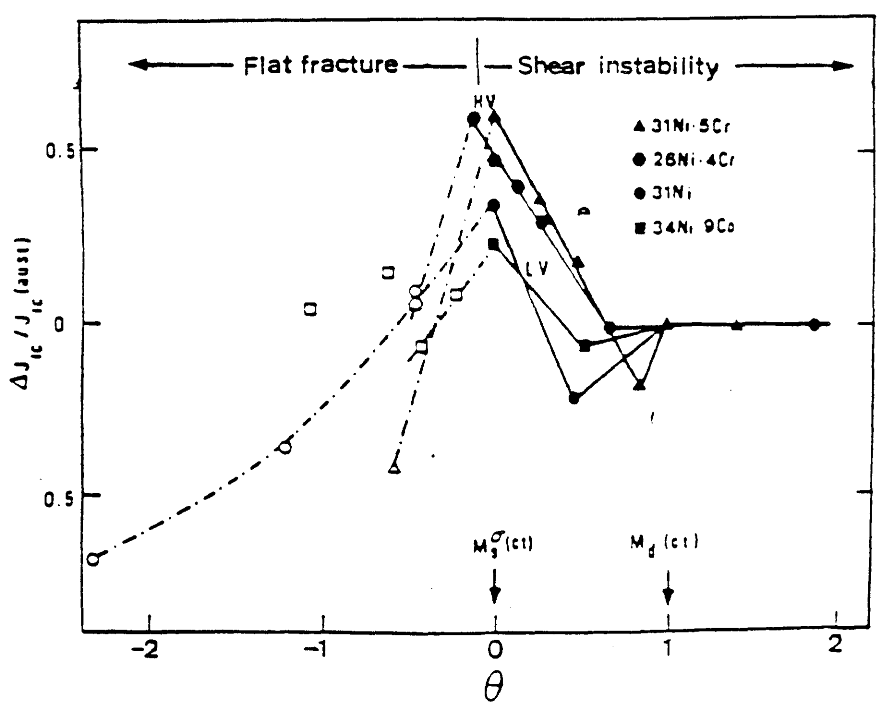

Fig. 2-4(c) Relative enhancement in fracture toughness vs. nondimensional temperature θ for γ'-strengthened TRIP steels [1].

2.2. Ductile Fracture and Shear Instability

The micromechanism of ductile fracture involves nucleation and growth of voids to the point where voids link by coalescence or by the formation of shear bands between them. The occurrence of ductile fracture usually requires the presence of second-phase particles, such as nonmetallic inclusions, carbides, or precipitates which promote the formation of voids.

The nucleation of voids arises from either particle cracking or interface decohesion, depending on the property of particle (brittle or soft), the interfacial cohesion between particle and matrix (strong or weak), and the shape of particle (high or low aspect ratio). Theories of nucleation have been developed based on an energy criterion [31,32], local strain criterion [33,34], or local stress criterion [35,36]; all of them assume that the particles are equiaxed, rigid, and plastically nondeformable. Brown and Stobbs [31] proposed a nucleation model based on the assumption that the elastic energy released by a spherical particle is equal to the surface energy of the cavity formed during deformation, and obtained the critical strain, γ_n, for the onset of plastic cavitation in terms of surface energy of the crack, particle radius and shear modulus of the particle as $\gamma_n = (6\,\sigma / r\ G\,)^{1/2}$. This equation shows that void formation first occurs at the largest particles. The energy criterion overestimates the required strain. McClintock [33] suggested that cavity formation at interfaces may obey a critical local strain criterion, or alternatively a combination of a critical interfacial shearing strain and an interfacial normal stress. On the other hand, Argon et al. [35,36] formulated a nucleation model based essentially on continuum plasticity and incorportated a dislocation punching mechanism proposed by Ashby [37]. They concluded that void nucleation occurs at the interfacee of particles larger than 100 Angstroms when the interfacial stress reaches a critical value. The effects of particle shape, stress-state, particle distribution as well as temperature are still in need of further study.

Once the voids nucleate, they grow immediately by further plastic straining. Void growth rate under idealized conditions has been analyzed by McClintock [387], and Rice and Tracy [39]. Both models show a similar exponential amplification of void growth by the stress state and this is particularly important in the region around a crack tip or a notch root because of the high triaxility. Tracey [40] also studied the growth of long cylindrical pores in a rigid plastic, strain-hardening material, taking pore interaction into account. He found that strain hardening decelerates void growth, whereas pore interaction accelerates void growth.

The final stage of ductile fracture is caused by the linkage of voids-to-voids or voids-to-crack tip and then the crack propagates. According to the observation of crack profiles of some high strength steels, Knott et al. [41,421] proposed three possible ways for crack initiation, as schematically shown in Fig.2-5 : (1) For high strain-hardening material, void coalescence occurs due to the internal necking between a blunt crack tip and a large void forming ahead of the crack from a loosely bonded inclusion. Rice and Johnson [43] developed a theoretical model for this case employing the Rice and Tracey analysis of void growth [39]. They predicted the critical

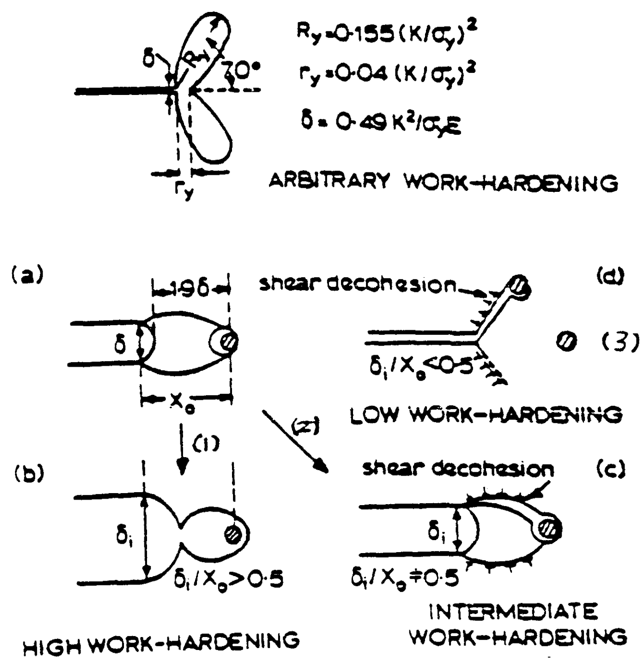

Fig. 2-5. Schematic process of crack growth : (1). (a)-(b) void coalescence; (2). (a)-(c) shear decohesion along spiral slip-lines; (3). (d) shear decohesion along straight slip-lines [41].

crack opening displacement (COD) at fracture initiation in terms of the ratio between initial void size and its position w.r.t. the crack tip. (2) For a material with intermediate strain-hardening capability, an initially sharp crack tip is blunted and then follows the logarithmic spiral slip-line to envelop the void. (3) When the work-hardening capability is very low such as in prestrained steels, the sharp crack extends, without being blunted, along the 45^0 straight slip-line ahead of it.

The onset of ductile fracture in both case (2) and (3) results from shear localization and may lead to a zig-zag fracture pattern which has been observed in many high-strength steels [44,45]. Rice and Johnson's model [43] breaks down if the shear localization or the formation of shear bands causes the fracture initiation instead of necking down of the ligament between voids, and thus overestimates the critical CODs at crack initiation for many high strength steels. The phenomenon of flow localization into narrow shear bands has been regarded as a significant precursor for the initiation of ductile fracture. The onset of flow localization can be viewed as a bifurcation of an originally uniform plastic flow occurring at a critical strain and is usually associated with the formation of shear bands. Above that critical strain , the imposed macroscopic strain will accumulate in the shear bands and finally lead to fracture. Experimental observation of void nucleation and growth within shear bands is not uncommon, although whether void formation on particles causes shear-band localization or merely results from it has not been conclusively established from experimental observations. For a ductile multiphase material, an initial imperfection like voids could be formed during processing or voids may nucleate and grow during straining. Such imperfections surely change the flow relation of the material and consequently affect the condition of shear localization as concluded by Rice [46]. Flow localization occurs as the result of two competitive processes during further straining : (1) matrix surrounding voids is continuously strain hardened, (2) growth of voids reduces the load-carrying capacity. If factor (2) is larger than factor (1), then high strain can be localized into a shear band.

Needleman and Rice [47], Saje at el. [48,49] and Tvergarrd [50] have used the yield condition for a porous ductile material proposed by Gurson [51] as well as void nucleation and growth theories to derive the shear instability criteria in porous plastic solids with a power strain-hardening behavior. In the case of strain-controlled void nucleation, a critical strain-hardening rate normalized by the equivalent stress, $(h/\sigma)_c$, in axisymmetric and plain-strain tension is derived by Needleman and Rice [47] :

$$(h/\sigma)_c = 3/2 \cdot f \cdot \mathrm{Cosh}(1.5 \cdot \sigma_h/\sigma) \cdot \mathrm{Sinh}(1.5 \cdot \sigma_h/\sigma) + F \cdot \mathrm{Cosh}(1.5 \cdot \sigma_h/\sigma) \tag{2-12}$$

where h is the effective strain-hardening rate, f is the current void-volume fraction, σ_h is the hydrostatic stress, σ is the effective stress, and the coefficient F is related to the volume fraction of voids which are nucleated during straining. When the normalized strain-hardening rate of material, h/σ, is less than the value of $(h/\sigma)_{crit}$, shear localization takes place. Once the constitutive relation of the matrix material and the nucleation parameter are known, the critical strain for shear localization or fracture initation under tension can be determined from Eq.2-12. Saje et al. [48]

have assumed that void nucleation follows a normal distribution about some mean critical plastic strain and illustrated the destabilizing effect of void nucleation on shear localization. They also appropriately selected parameters to fit experimental data and showed that the predicted fracture strain is in good agreement with the observation.

Unfortunately, the model described above is developed only for the case of a uniform stress state. The non-uniform distribution of stress/strain or triaxiality as well as the interaction between void and crack tip has been proved to significantly affect the formation kinetics of voids [52] with respect to the imposed strain, especially the growth rate, and consequently the critical COD for shear band localization. Furthermore, the Needleman and Rice model only accounts for the total volume fraction of voids f, not for the size , shape and distribution of voids, because the continuum-mechanics approach ignores the detailed microstructural features. In addition to the complex stress/strain fields and triaxiality, appropriate material-size parameters, such as the ratio of particle size and spacing, have to be included in the criterion to predict the failure initiation in a crack tip. This is the key problem in establishing quantitative structure-property relationships for a ductile material [53].

Chapter 3. Preparation of Materials

3-1. Chemical Composition

Two rapidly solidified 16 Cr - 10 Ni austenitic steels with 0.3% carbon, 0.33% phosphorus and different manganese contents were designed according to a previous study [54] on a steel with similar composition but higher phosphorus content (0.42%) and without addition of manganese. Tensile testing at room temperature showed that the latter steel failed in a brittle intergranular mode associated with a large amount of deformation-induced martensitic transformation. Despite the influence of processing, the brittle nature could partly result from an excess of phosphorus, which is expected to tie up mostly with carbon and form phosphocarbides [2], but the phosphorus level remaining in the matrix may lead to the grain-boundary embrittlement. The austenitic phase of the manganese-free steel is also too unstable to measure the properties of the austenitic phase, which is required in order to evaluate the contribution of the mechanically-induced martensitic transformation on the mechanical properties. Therefore, the present investigation is directed to compositions with less phosphorus and with the addition of manganese.

Table 3-1 lists the chemical compositions of the newly designed alloys, designated by 3.5Mn and 0.5Mn, respectively. The 3.5Mn alloy is intended for measuring the properties of the austenite since Mn is a good austenite-stabilizer. Phosphorus is the only element, known at present, which can promote effective precipitation hardening of austenitic steels via complex carbides [2]. However, phosphorus is also a well-known embrittling impurity in high strength steels and its severe segregation could limit the fracture ductility and fabricability of a conventionally melted ingot. Hence, rapid solidification processing was employed to minimize segregation and avoid potential danger of brittle fracture.

Table 3-1. Chemical Compositions (wt.%)

Materials	Cr	Ni	Mn	P	C	Al	Fe
3.5 Mn Alloy	15.7	9.91	3.56	0.33	0.254	0.022	Bal.
0.5 MN Alloy	16.0	10.0	0.46	0.33	0.286	0.032	Bal.

In this chapter, the processing of the selected alloys, including atomization, consolidation, heat treatment, and warm-rolling, to produce the desirable combination of strength and transformation behavior will be described.

3.2. Alloy Preparation

Master billets with the desired compositions were produced by vacuum induction melting at the Republic / LTV Steel Corporation, and then remelted and atomized by the Pratt and Whitney centrifugal process [55,56]. Fig. 3-1 [57] is a schematic diagram of this system, showing the melting and the atomizing chamber. The melting chamber contains a 15 kg-capacity induction furnace with an alumina crucible and stopper rod positioned over the pour-tube nozzle which passes through the intermediate plate. The atomizing chamber contains a centrifugal disc, which rotates at 20,000

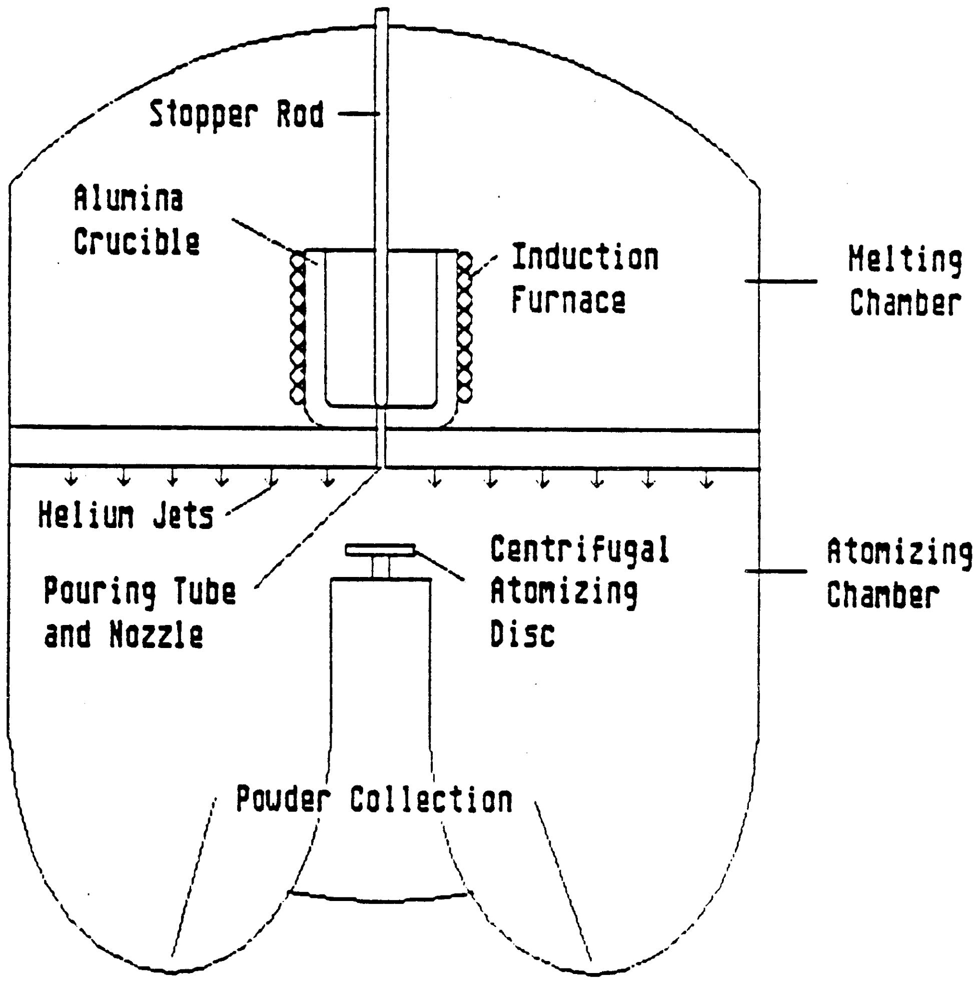

Fig. 3-1. Schematic representation of the Pratt and Whitney centrifugal atomization unit [57].

rpm, and collection buckets for the atomized powders. Helium jets spray downwards from the intermediate plate for cooling the atomized droplets. The melt was first killed by a small amount of aluminum to reduce the oxygen content and was then atomized by withdrawing the stopper rod and allowing the melt stream to strike the rotating disc. Droplets were formed on contact with the rotating disc and solidified while passing the field of helium jets.

Spherical powders 20 to 70 μm in diameter are produced by this process. A very fine casting structure with submicron dendritic arm spacing or cell diameter, as shown in Fig.3-2, facilitates homogenizing the alloys. However, porosity is usually found inside the powder particles (also see Fig.3-2) and is believed to result from mechanical entrapment of the atomizing helium gas. Similar observations have been made on atomized steel powders [58]. A study recently done by Libera [59] found that the porosity in Fe-Ni powders is a strong function of particle size and atomization technique. He concluded that larger particles contain more pores than smaller ones, and the centrifugally - atomized powder made by Pratt and Whitney has a significantly higher amount of porosity than the conventional argon gas - atomized powder by Alloy Metals, Inc. Such porosity is generally undesirable as it can degrade the mechanical properties of consolidated products [60]. This helium contamination introduced an unexpected problem concerning the fracture behavior after heat treatment and will be discussed later.

The powder was then sealed in 1008 low-carbon steel containers for the subsequent consolidation; this was accomplished by hot extrusion at high

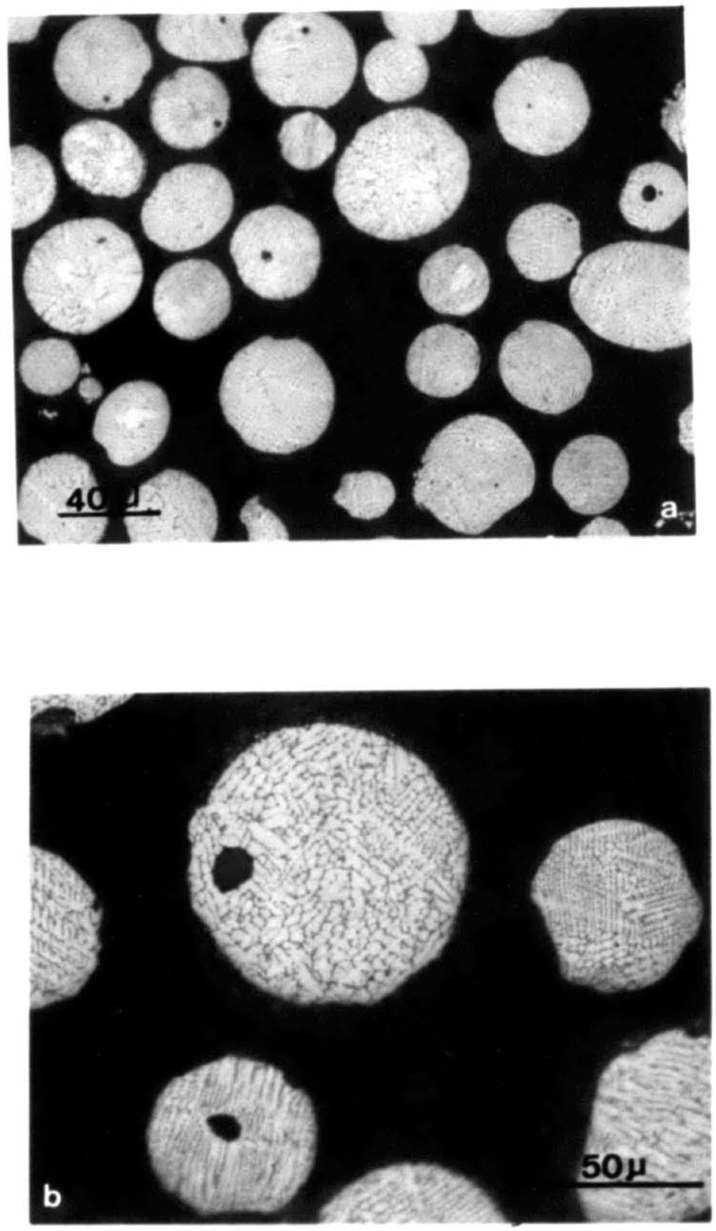

Fig.3-2. Optical micrographs of 0.5Mn rapidly solidified powders, showing fine solidification structure and presence of porosity; (a). low magnification, (b). high magnification. Etchant : Fry's reagent.

temperature, 1235^{o}C , with an extrusion ratio of 25 : 1. The final product was in the form of cylindrical bar, with a diameter of 19.05 mm (0.75 inch), including 1 mm thick can material. Because of the extensive deformation involved in the extrusion and the effect of the high working temperature, the powders were successfully consolidated. No voids or lack of bonding were found. SEM metallography of the as-extruded material, Fig.3-3(a), verified that the cast structure has been broken down and replaced by an equiaxed grain structure, with a grain size of 24 μm, decorated by Cr-enriched carbides according to the X-ray spectrum Fig.3-3(b). Since the strengthening of the selected alloy system mainly comes from carbide precipitation, the carbides formed during the extrusion had to be dissolved in the austenitic matrix through solution treatment .

3-3. Solution Treatment

The desired solution treatment for the present alloys should, first, dissolve all carbides and, second, not cause severe grain coarsening. A systematic search for the appropriate solution condition was carried out for both alloys. The extruded bars were hung in a vertical tube furnace by molybdenum wires and heated under the protection of argon gas at temperatures ranging from 950 ^{o}C to 1300 ^{o}C for 1 and 2 hours, and then directly dropped in a cold water bath along their axial direction. The microstructure corresponding to each solution treatment was examined. The hardening response aged at 700 ^{o}C was also measured to further confirm the completeness of carbide dissolution during the prior solution treatment.

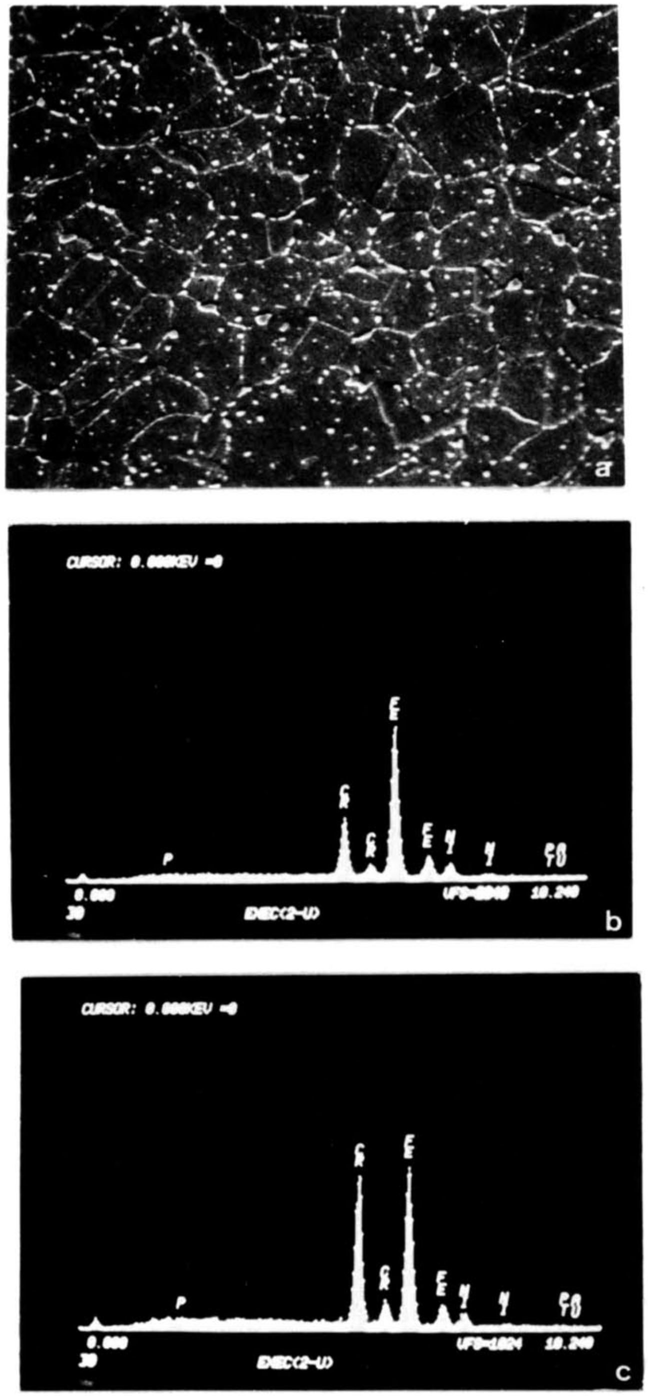

Fig. 3-3. (a). SEM micrograph of the as-extruded 0.5Mn alloy, showing many particles distributed in the fully dense matrix. Microanalysis indicates these particles are chromium carbides by comparing (b) the x-ray spectrum from the matrix with (c) that from the particle (c). Etchant : Fry's reagent.

It should be noted that, besides the expected grain growth and carbide dissolution, void formation also occurred as a side effect of the high-temperature solution treatment, as shown in Fig. 3-4. This indicates that the entrapped helium bubbles in the powders were not eliminated but simply sealed off during extrusion. Due to the high plastic deformation and hydrostatic pressure caused by extrusion, the helium gas bubbles were compressed and confined in very tiny spaces. On heating, the helium is capable of opening up voids against the softened material at the solution temperature, known as "thermal-induced porosity". In general, most of these voids were found to be distributed along grain boundaries or grain corners.

Table 3-2 lists the microstructural features and the aging response at various solution temperatures. The carbides were not completely dissolved until 1150^{o}C, where grain growth and void formation began to occur. Beyond 1200^{o}C, both grain size and porosity rapidly increased with temperature. The optimun solution treatment was 1150^{o}C for 2 hours or 1200^{o}C for 1 hour, but the former was selected.

Fig.3-5 shows an SEM fractograph of the 0.5 Mn alloy, solution treated at 1150^{o}C for 2 hours and aged at 680 ^{o}C for 14 hours, then tested in tension at room temperature. The specimen was ruptured before the onset of necking and displayed a very flat fracture surface, normal to the loading axis, with low reduction in area. As can be seen in the higher magnification picture Fig.3-5(b), completely intergranular rupture occurred on the fracture surface which is decorated with a great amount of voids formed during the solution treatment. Apparently, the preexsiting pores contributed to premature fracture.

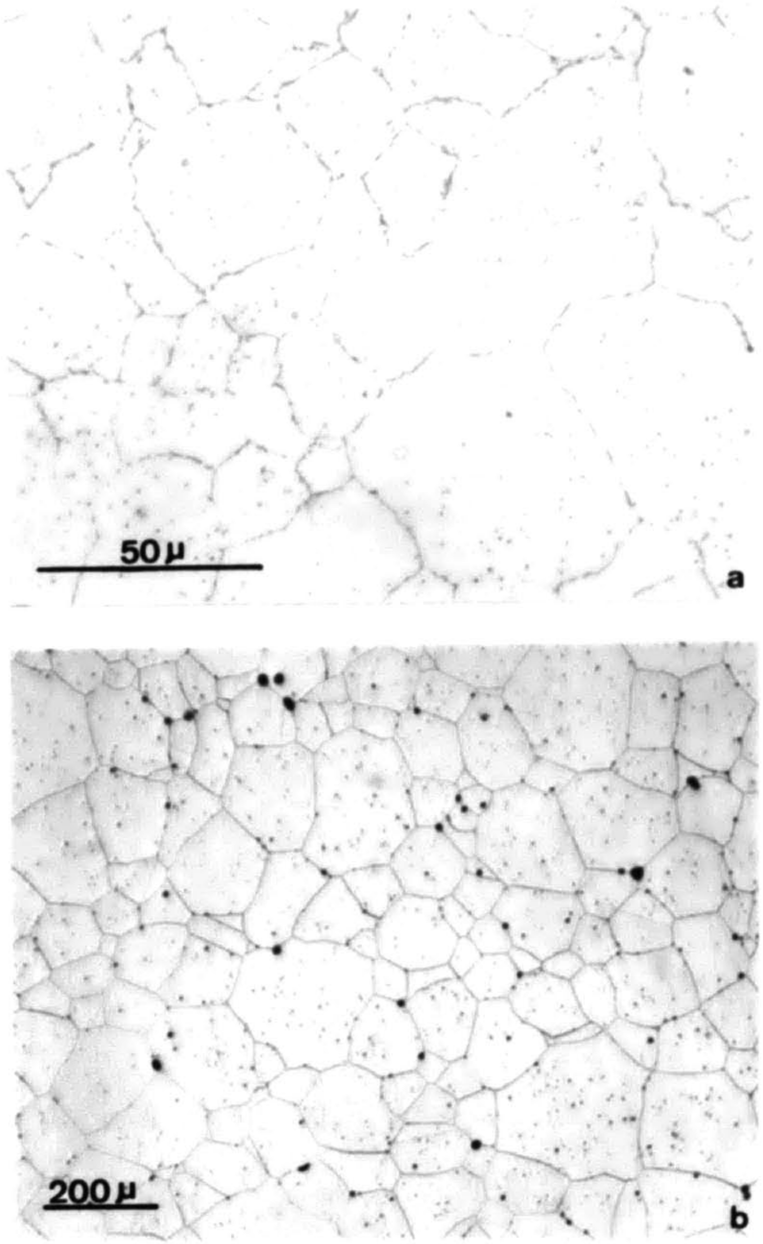

Fig. 3-4. Carbide dissolution, grain growth, and void formation occurred during solution treatment at high temperature; (a). optical micrograph of the as-extruded 0.5Mn alloy, showing no voids but residual Cr-carbides in the matrix; (b). optical micrograph of the 0.5Mn alloy solution treated at 1300°C for 1 hour; showing large pores on grain corners. Note difference in magnification between (a) and (b). Etchant : 33 cc Hcl, 67 cc HNO_3.

Table 3-2 Effect of Solution Treatment

Solution Treatment (°C/Hr)	Degree of Carbide Dissolution	Mean Intercept Length (μm)	Porosity (%)	Aging Response 700°C/6Hr
As-extruded	-----	16.9	~0	-----
1100/1	Partial	17.1	.008	Hv 347
1100/2	Partial	17.3	.01	Hv 353
1150/1	Almost	30.8	.09	Hv 394
1150/2	Complete	43.1	.24	Hv 410
1200/1	Complete	48.7	.53	Hv 414
1250/1	Complete	72.0	.68	Hv 417
1300/1	Complete	101.5	.98	Hv 425

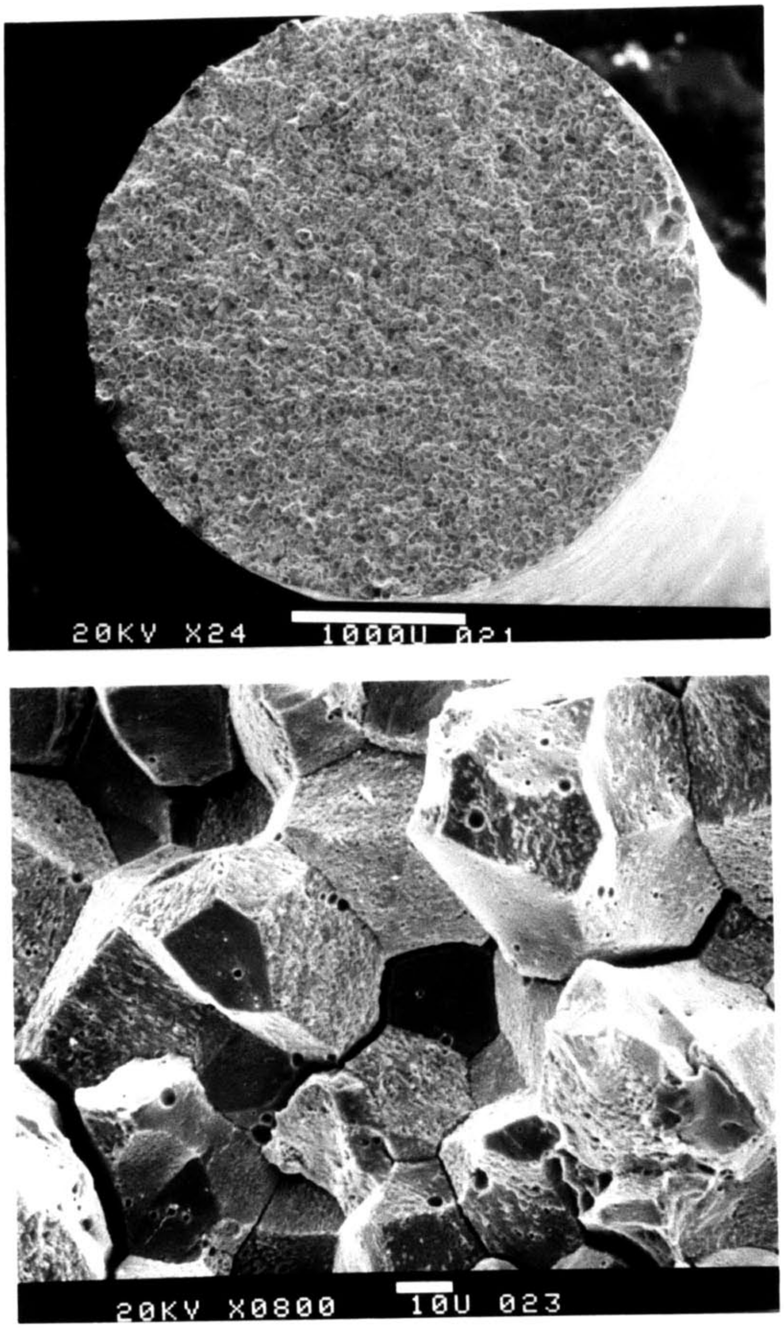

Fig. 3-5. SEM fractograph of 0.5Mn alloy without warm-rolling (1150^{o}C/2hr. solution-treated and 680^{o}C/14hr. aged), tensile tested at 25^{o}C; (a). overview of fracture surface which is flat and normal to the loading axis; (b). microscopic observation revealing intergranular fracture with the distribution of pores on the grain surfaces.

One of the initial objectives in this work was to design a TRIP steel which is able to achieve high yield strength (> 180 ksi or 1250 Mpa) via carbide precipitation hardening and to avoid the severe mechanical working of austenite that is typically used for raising the strength of conventional TRIP steels. The phosphorus-containing alloys do exhibit good age-hardening ability without the aid of mechanical working. The hardness can be raised to Rc45 simply by aging the solution-treated material at 680°C. However, the void formation during solution treatment due to the helium gas contamination interfered with this goal. Warm-rolling after solution treatment turned out to be the most convenient remedy for eliminating or reducing the detrimental effect of helium bubbles.

3-4. Warm-Rolling and Aging Treatment

The main purpose of warm-rolling in this work was to reseal the voids formed during the solution treatment. Other effects on the strength and aging kinetics, and intergranular fracture resistance were also expected. Single direction, multi-pass rolling with 40 pct reduction in thickness was conducted at 450°C to obtain transformation-free material.

Preliminary study indicated that direct rolling of the round bars (original shape of the hot-extruded material) brought about an inhomogeneous hardness distribution across the thickness direction, as shown in Fig.3-6(a). Because of the workpiece geometry and light reduction, the central region was less deformed than the surface. Although the subsequent aging treatment reduced most of the mechanical inhomogeneity

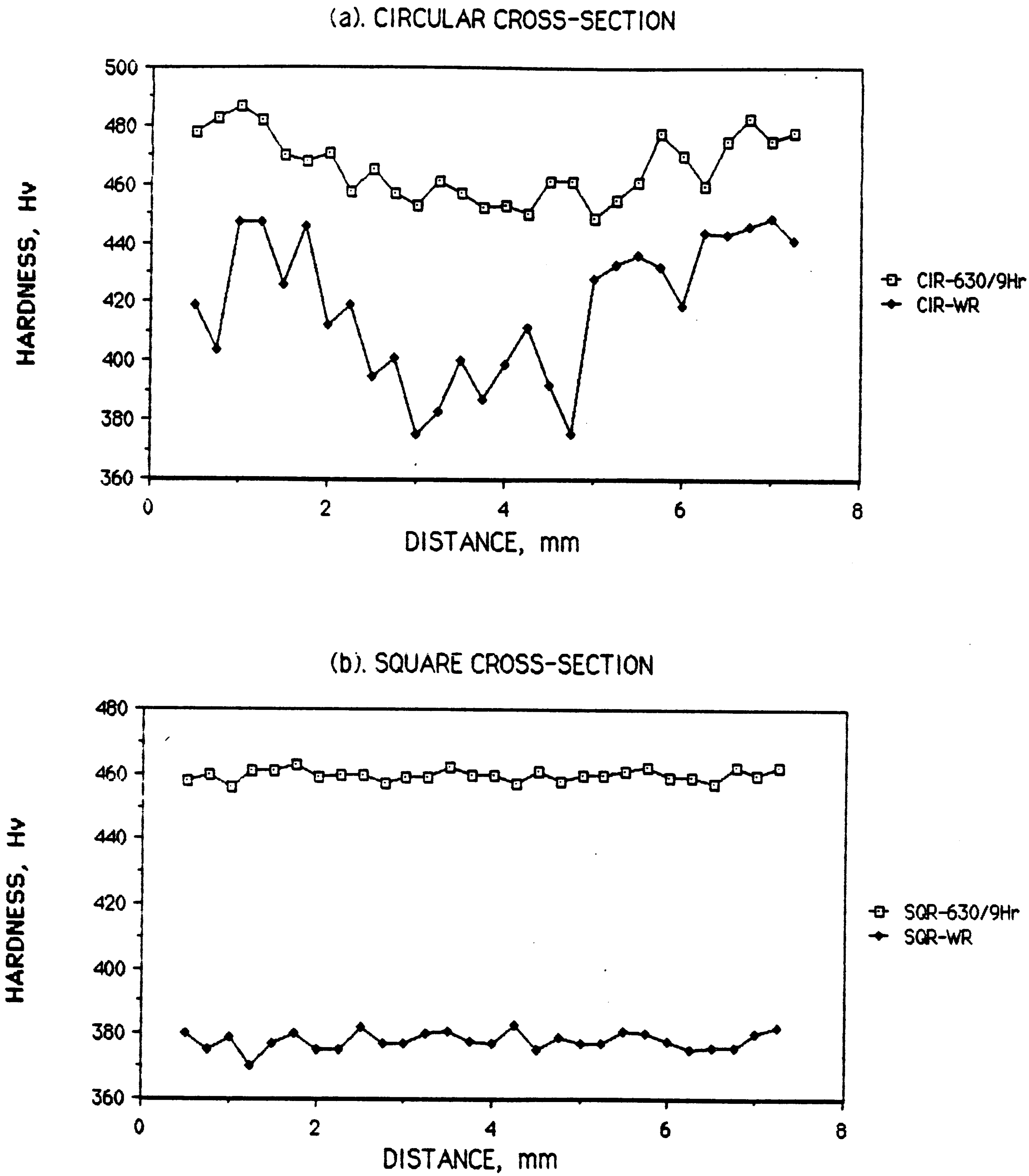

Fig. 3-6. Homogeneity of hardess distribution in the thickness direction of a warm-rolled bar before and after aging was better by using a prerolled workpiece with a square cross-section (b) rather than a circular one (a).

between the center and the surface, chemical inhomogeneity, which changes the stability of austenite, could still exist since more deformation produced a higher aging rate. Therefore, after solution treatment, a cylindrical bar was milled to form a rectangular bar with square cross section of 14 by 14 mm, and then warm-rolled. The hardness distribution before and after aging was quite uniform as shown in Fig.3-6(b). Warm-rolling was also successful in closing the voids without causing martensite formation, as can be seen in Fig.3-7, and reduced the brittleness of alloys that will be discussed in Chapter 5.

For the carbide-precipitation hardening austenitic steels, the aging treatment turns out to be a powerful way of controlling the alloy properties, mechanically and physically : 1). The stability of the austenite. As the precipitation reaction proceeds, the austenitic matrix becomes depleted of carbon and other alloying elements and consequently becomes less stable by raising the transformation temperature under a fixed stress state. 2). The strength difference and the relative transformation volume change ($\Delta V/V_\gamma$). Since carbon and phosphorus atoms provides more effective solution strengthening of the martensite than the austenite, less carbon and phosphorus remaining in the austenitic matrix due to more phosphocarbide precipitation will reduce the strength difference between these two phases and also alter the transformation volume change. Both parameters are believed to affect the transformation toughening [61]. 3). The strength level of the austenite. When a pricipitation-hardening alloy is aged at a given temperature, its strength first increases with time, reaches a peak, and then falls. That allows us to control the austenite at a given strength level, but with other different properties mentioned in 1). and 2). by underaging

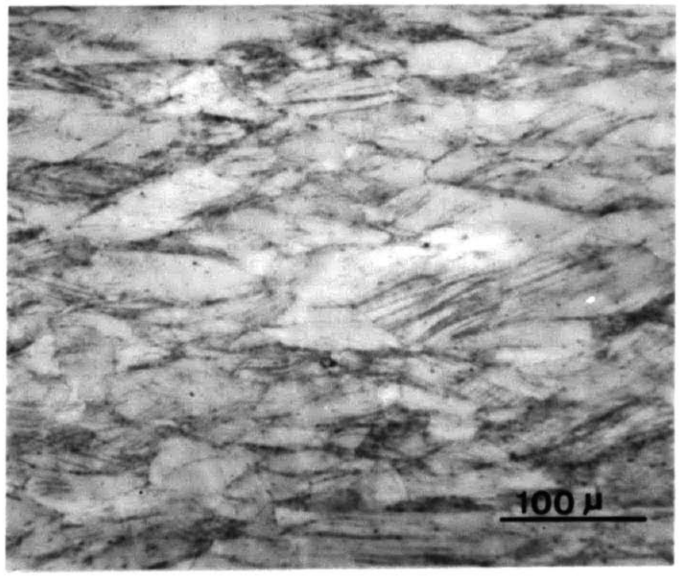

Fig. 3-7. Metallograph of the warm-rolled 0.5Mn alloy. Pores formed during 1150ºC/2hr solution treatment were successfully closed. Etchant : 33 cc Hcl, 67 cc HNO_3.

and overaging. This is the guideline used to establish the appropriate aging conditions.

Aging behavior was studied for both alloys with and without warm-rolling. It is well-known that the peak hardness of aging increases as the aging temperature decreases, but then longer holding times are needed. Spending a day to reach the desirable hardness would be tolerable and this provides one criterion for choosing the aging treatments. Besides aging at a fixed temperature, a sequential process, in which the alloy was first aged at quite low temperature for a short period to nucleate more precipitates and then held at a higher temperature for faster growth of the precipitates, was employed. As a result, the sequential process effectively shortens the necessary aging period and raises the peak hardness, particularly for the solution-annealed alloy. Mechanical working increases the nucleation sites for precipitation by introducing a high dislocation density so that the aging kinetics are accelerated. In fact, warm-rolling is able to lower the usable aging temperature about 100^{o}C for the present case.

Because of the embrittlement due to void formation, the aging behavior of the solution-annealed materials will not be presented here. Fig.3-8(a) and (b) summarize the aging response of the warm-rolled 0.5 Mn and 3.5 Mn steels, respectively. All curves exhibit an inverted " V " shape and thus the alloys can be treated to reach a preset hardness level by either an underaging or an overaging condition. In order to compare with the transformation enhancements of ductility and toughness in the γ'-strengthened metastable austenites [1] at the same strength, the studied alloys are intendedly aged to reach a hardness of Hv 465 or Rc 46.5, similar

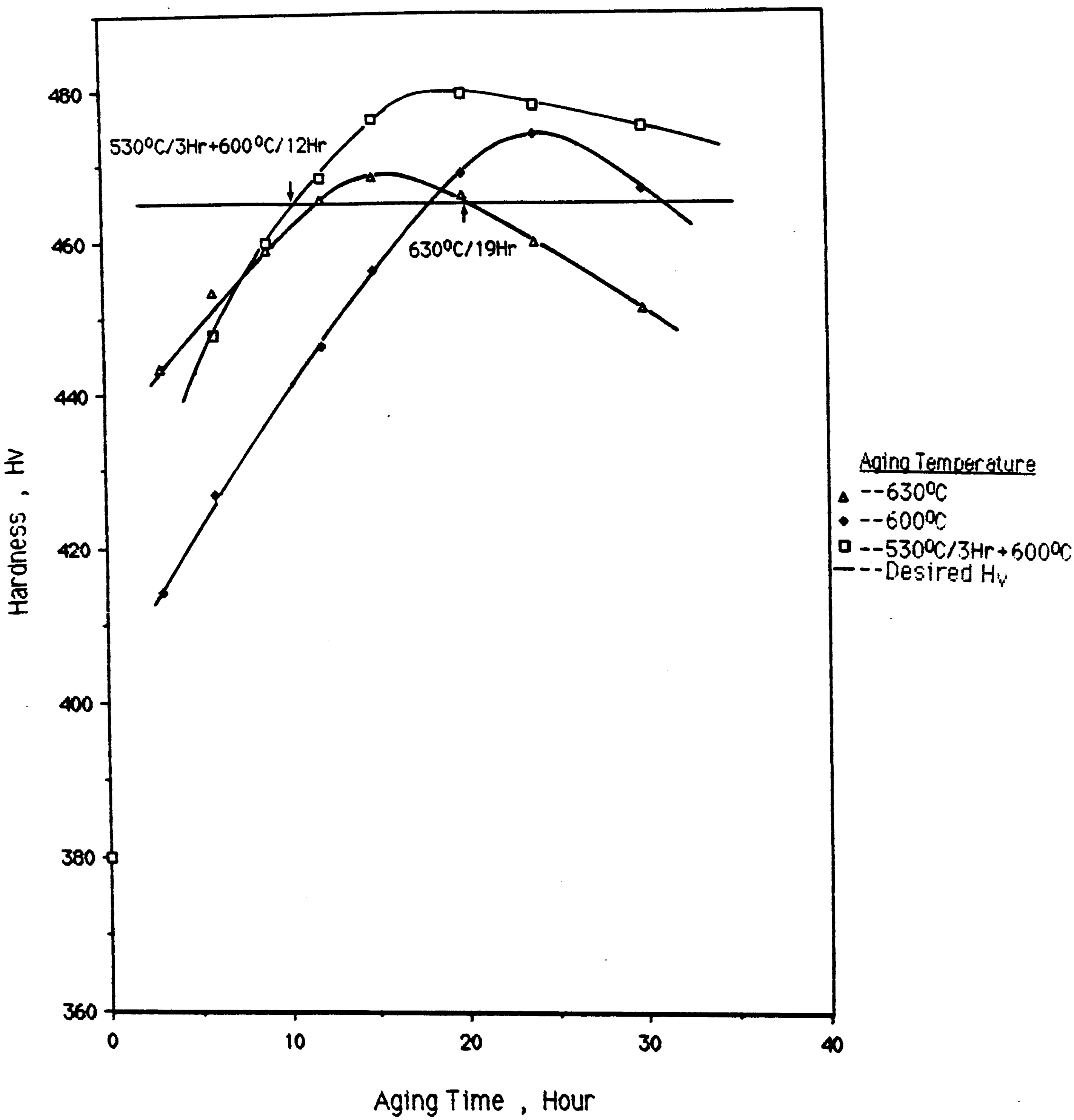

Fig. 3-8(a). Aging behavior of the warm-rolled 0.5Mn alloy. Arrows indicate the selected underaging and overaging conditions.

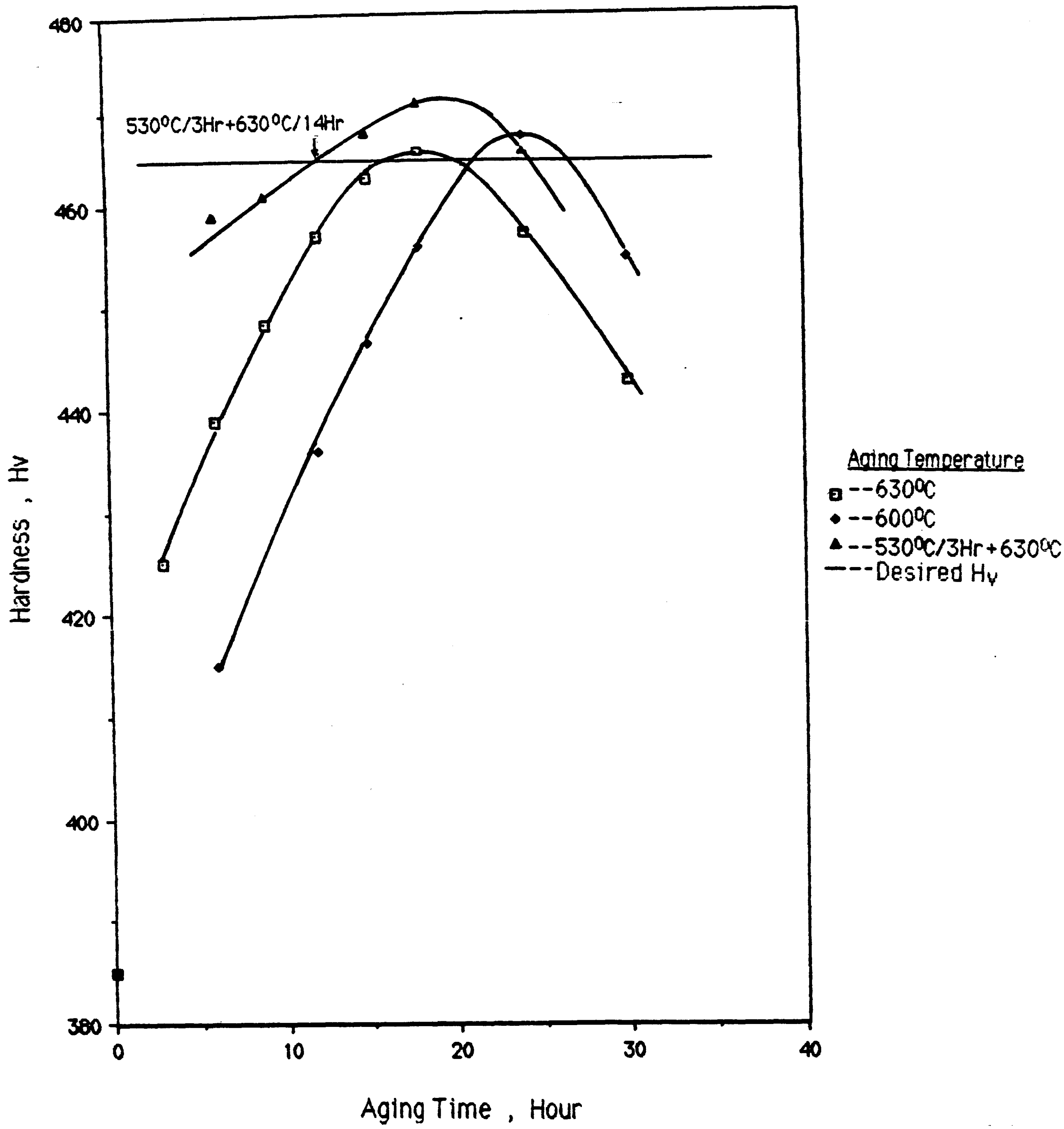

Fig. 3-8(b). Aging behavior of the warm-rolled 3.5Mn alloy. Only an underaging treatment was selected as indicated by the arrow.

to the former alloys. Two intersection points between each curve and the straight line representing the chosen hardness level. The desired aging conditions indicated by arrows are listed in Fig.3-8. Underaging and overaging treatments were selected for the 0.5 Mn alloy to vary the transfomation volume change and the strength difference between α' and γ phases. For the 3.5 Mn alloy, only the underaging treatment which can produce the most stable state was needed. Henceforth, these three treated conditions will be designated 0.5Mn-U, 0.5Mn-O and 3.5Mn-U, respectively.

3-5. Hardness Difference and Transformation Volume Change

The hardness difference $\Delta Hv(= Hv,\alpha' - Hv,\gamma)$ and relative transformation volume change $(\Delta V/V_\gamma)_{atom}$ were determined by measuring the microhardness values and lattice parameters of the austenite and the martensite at room temperature after aging, and listed in Table 3-3 along with the values for two γ'-strenghthened TRIP steels studied by Leal [1]. Since all the M_S temperatures of aged phosphorus-containing steels are below $-196^{o}C$, no martensite was formed even after holding in liquid nitrogen for 24 hours. Before measuring the hardness, a tensile stress was imposed on the alloys at liquid nitrogen temperature until a Luders band propagated through the whole gage length of the specimen. The austenite was thus transformed in the stress-assisted mode with negligible strain-hardening, as confirmed by comparing the austenite hardness values before and after loading with that of martensitic plates large enough for the microhardness measurements. From the results shown in Table 3-3, the hardness values of the austenitic phase for the aged 0.5Mn and 3.5Mn alloys are close to the preset level (Hv465) in Fig.3-8, while the hardness of the martensitic phase and hence the hardness difference, $Hv_{,\alpha'}-Hv_{,\gamma}$, markedly decrease for the overaged condition as expected due to less alloying elements remaining in the matrix, especially carbon and phosphorus. The γ'-strenghthened 31Ni(L) steel showed the same, low ΔHv as the overaged 0.5Mn alloy, although it was slightly underaged. Again, this can be explained by the very low content of interstitial atoms for further strengthening the martensitic phase. On the basis of similar considerations, the hardness difference ΔHv of another γ'-strenghthened steel 31Ni-5Cr(L) is expected to be the same.

For the 0.5Mn alloy, Table 3-3 shows that the lattice parameters of the α' and γ phases as well as the relative transformation volume change $(\Delta V/V_{\gamma})_{atom}$ decreased when the alloying elements were progressively rejected from the matrix to the carbides. The underaged 3.5Mn alloy exhibited a surprisingly low value of $(\Delta V/V_{\gamma})_{atom}$ compared to the underaged 0.5Mn alloy. The substantial effect of maganese additon on $(\Delta V/V_{\gamma})_{atom}$ is unclear, but it is beneficial for present purposes because very different volume changes can then be obtained at the same ΔHv.

In summary, the alloys in Table 3-3 can be divided into two groups according to ΔHv : 1). low ΔHv alloys with $(\Delta V/V_{\gamma})_{atom}$ from 2.44 to 3.65 %, consisting of 0.5Mn-O, 31Ni(L),and 31Ni-5Cr(L); 2). high ΔHv alloys with $(\Delta V/V_{\gamma})_{atom}$ from 2.69 to 5.08 %, including 0.5Mn-U and 3.5Mn-U. Using these alloys with the parent phase held at a similar strength level, we can compare the transformation toughening effects arising from the dilatation and from the increment of strain-hardening ability.

Table 3-3 Microhardness Difference Between α' and γ Phases and Transformation Volume Change in the Phosphocarbide- and the γ'-Strengthened Austenitic Steels.

	3.5Mn-U	0.5Mn-U	0.5Mn-O	0.5Mn-O**	31Ni(L)*	31Ni-5Cr(L)*
Hv,α'	543	557	516	----	512	----
Hv,γ	457	467	470	----	463	----
$Hv,\alpha'-Hv,\gamma$	86	90	46	----	49	----
$a_{\alpha'}$(A)	2.8816	2.8903	2.8643	2.8426	2.8748	2.8861
a_{γ}(A)	3.5986	3.5822	3.5660	3.5412	3.5930	3.6139
$(\Delta V/V_{\gamma})_{atom}$,%	2.69	5.08	3.64	3.45	2.44	3.55

**---Aged at 630°C for 30 hours.

*----γ' strengthened austenic steel studied in Ref. [1].

Chapter 4. Experimental Procedures

In order to understand the influence of mechanically-induced martensitic transformation on the properties of this new class of TRIP steels, the following types of experiments were conducted : 1). mechanical tests to measure the temperature dependence of properties; 2). measurements of the transformation rates as a function of temperature, true plastic strain, and stress-state; and 3). characterization of the microstructure and fracture modes associated with the mechanical tests. To correlate the interrelationships among the results of these experiments becomes one of the main purposes of this work. The details of all experiments will be described in the following sections.

4-1. Mechanical Testing

A. Uniaxial Tensile Tests

Uniaxial tensile tests were conducted in an Instron machine at an initial strain rate of 0.02 min^{-1} in the temperature range of -196°C to 250°C. A lower strain rate of 0.0002 min^{-1} at -196, -110, and -73°C was also used to study the strain rate sensitivity of flow stress in the stress-assisted transformation regime.

Fig.4-1 shows a schematic diagram of the apparatus for controlling the test temperatures. The specimen was heated or cooled in a liquid bath which was contained in a stainless steel beaker welded to the lower specimem grip in the test machine. The selection of the liquid bath depends on the test temperature : silicone oil (from room temperature to 200°C), a low melting-point neutral salt (for above 200°C), methanol or n-pentane (from room temperature to -110°C), or liquid nitrogen (at -196°C). The bath was heated by electric heating tapes wrapped around the beaker, or it was cooled by pouring in liquid nitrogen. The temperature of the bath was kept uniform by a motor-driven stirrer. The test temperature, which was directly measured with a thermocouple mounted on the specimen, was controlled within 1°C for the testing duration. The insulating layer surrounding the beaker also provided good protection against environmental disturbance, especially at very low test temperatures.

Type TR-6 round specimens according to ASTM specification E8-82 were machined after the thermomechanical treatment; dimensions are shown in Fig.4-2. The loading axis was aligned with the rolling direction of the bars. Yield stress and true-stress vs. true-plastic-strain curve were calculated from the load-displacement curve, while uniform and fracture plastic strains were determined by measuring the change of cross-sectional area after the test.

4-1-2. Fracture Toughness Tests

Because of limitations in the material dimensions, the J-integral method with three-point bend loading was used to determine the fracture toughness corresponding to the initiation of crack growth (J_{IC}) at various temperatures ranging from -80 to 300°C. The test temperatures were controlled in the same way as in the tensile tests.

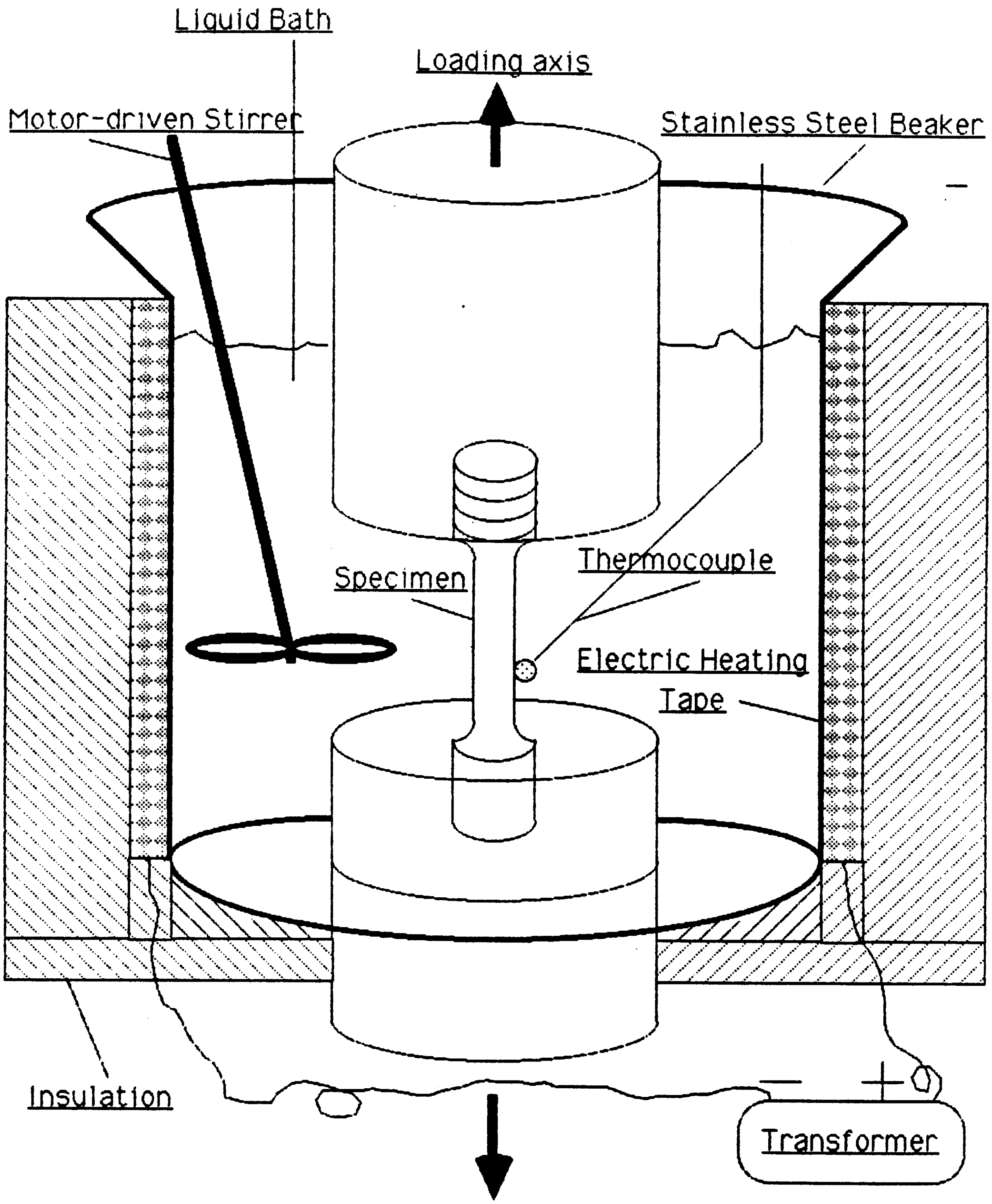

Figure 4-1. Schematic diagram of temperature control setup in tensile test.

A	B	C	D	E
60.0	25.4	4.06	8.13	3.18 R

UNIT : mm

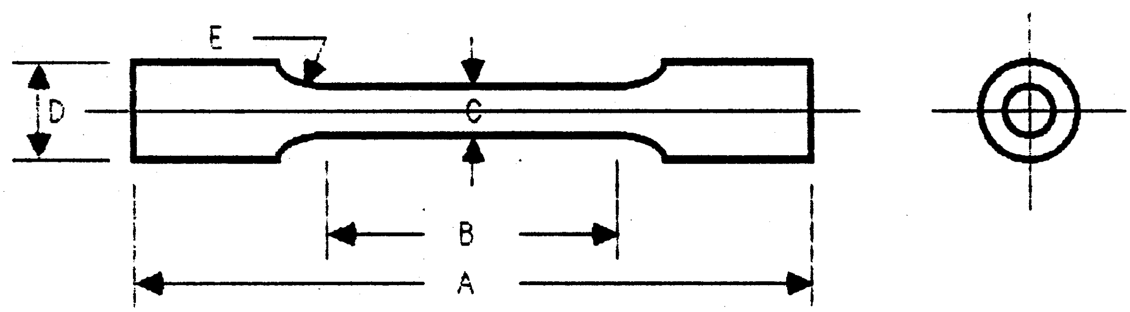

Figure 4-2 Dimensions and shape of tensile specimen

The V-notched specimens were cut with their length parallel to the rolling direction, and then fatigue precracked in stroke control on a servohydraulic Instron machine according to the specification in ASTM E813-81. In order to prevent the formation of mechanically-induced martensite, the precracking was performed at about 280°C by winding a flexible electric heating cord around the specimen as shown in Fig.4-3. No martensite phase was found in the subsequent metallographic examination. The specimen dimensions are shown in Fig.4-4 and the ratio of initial crack length a_0 to specimen width W was about 0.6 which lies within the recomended range.

The single-specimen technique [62,63,64] with the partial unloading compliance method was applied for determining the J-values. Before the test, MoS_2 paste was used to lubricate the contacts between the specimen and the rollers. The load P was recorded as a function of the load-line displacement Δ on a X-Y recorder at a constant crosshead speed of $2.12 \cdot 10^{-3}$ mm/second. Unloading-loading sequences were conducted on every specimen for 9 to 14 times. In the linear range of the P-Δ curve, the specimens were unloaded three times to obtain the compliance corresponding to the initial crack length. Before reaching the maximum load, at least one unloading sequence was performed; after attaining the maximum load, 5 to 10 unloading-loading cycles were performed, with the last unloading done at a load no less than 70% of P_{max}. Before each unloading, the crosshead was stopped for about 1 minute for stress relaxation, and then the load was dropped by no more than 10%. The zero suppression module and chart-speed controller of the test machine allowed the load and the displacement signals to be amplified by 10 times during the unloadings in order to

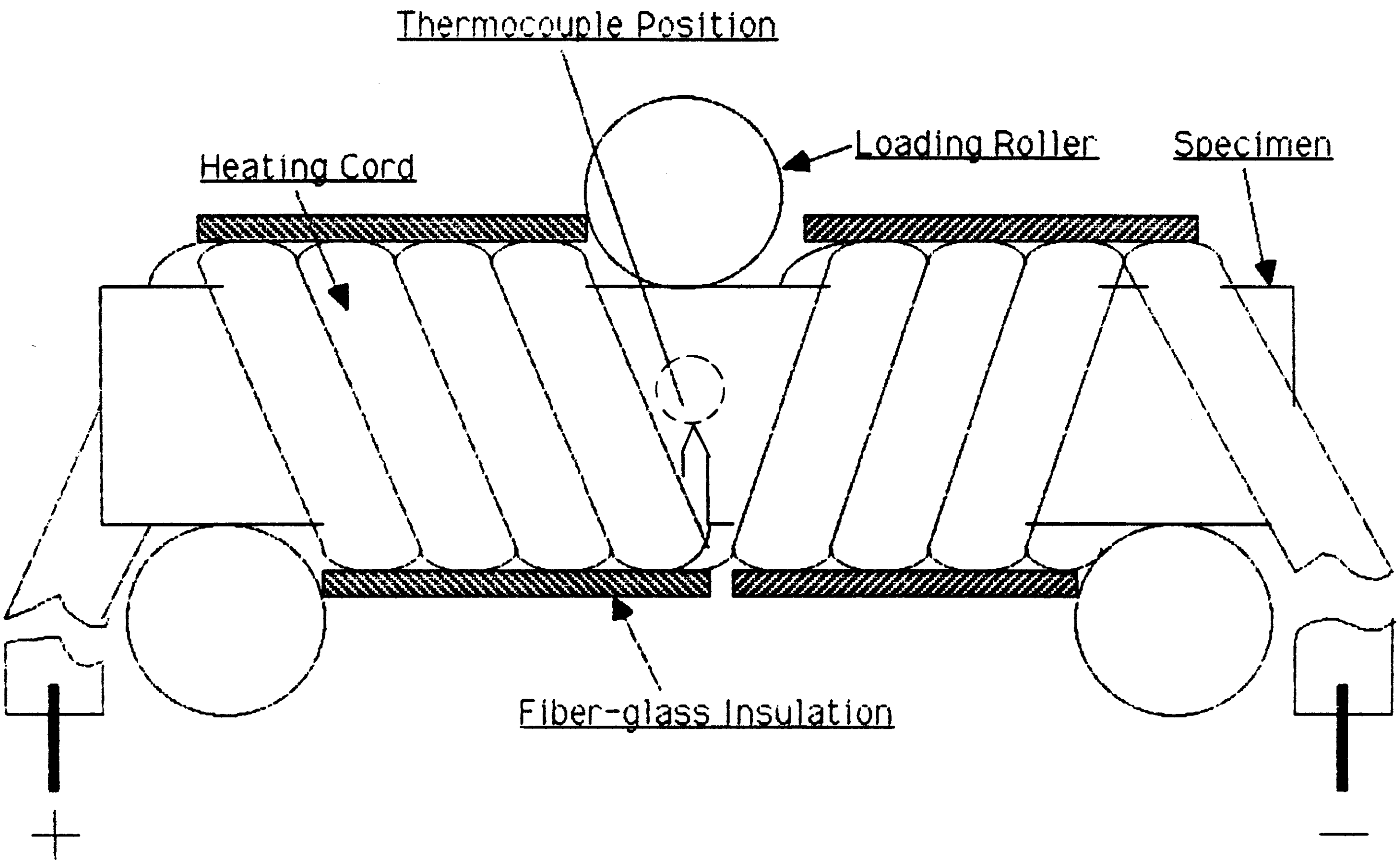

Figure 4-3. Arrangement of electric heating cords used to heat the specimen during fatigue precracking.

A	B	C	D	E	F	G
60.0	12.0	6.0	1.60	2.35	7.20	30 Deg.

UNIT : mm

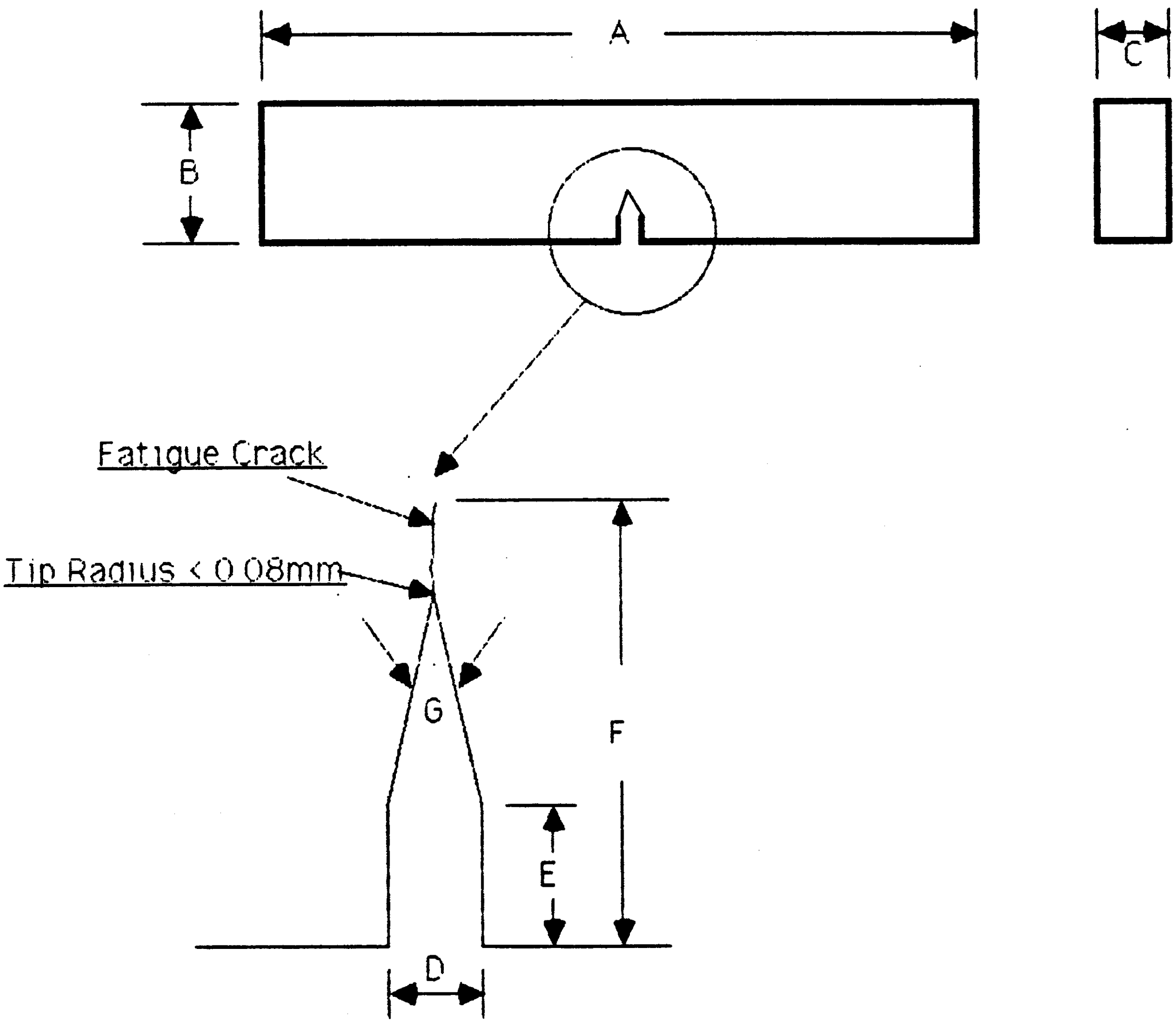

Figure 4-4. Dimensions and shape of three-point bending specimen.

facilitate slope measurements from the linear plots of the load vs. load-line displacement.

The crack advance in three-point bend specimens can be derived from the equation :

$$da = (b/2)(dC/C) \qquad (4-1)$$

where a is the crack length, C is the elastic compliance, and b is the remaining ligament (= W-a). Integrating Eq.4-1, the compliance can be expressed as [65,66] :

$$C = A/[1-(a/W)]^2 \qquad (4-2)$$

where A is a constant and equals 13.13 and 12.36 within the range of a/W from 0.45 to 0.75 according to Bucci and Tada's relations [67,68], respectively. Eq.4-2 is an accurate enough relationship and an easy one to handle for most purposes in the crack size range from 0.45 to 0.75 W. Taking the ratio of compliances to eliminate the constant A of Eq.4-2, we can obtain :

$$C_i/C_0 = [1-(a_i/W)]^2 / [1-(a_0/W)]^2 \qquad (4-3)$$

where a_0 = the initial crack length

a_i = the crack length at the load from which the ith unloading started

C_0, C_i = the compliances corresponding to $a = a_0$ and $a = a_i$, respectively.

Since the inverse of the compliance is linearly proportional to the slope of the unloading line, the crack advance Δa_i can be calculated as:

$$\Delta a_i = a_0 - a_i = (W-a_0)[1-(S_i/S_0)]^{1/2} \qquad (4\text{-}4)$$

where slopes S_i, S_0 are measured from the P-Δ curve, and the initial (and final) crack lengths are determined from metallographic observation or from the fracture surface broken at the liquid nitrogen temperature after the test. The accuracy was checked by comparing the final crack length evaluated by the unloading technique with that determined from direct measurement, demonstrations agreements within 10%.

The value of J_I corresponding to each crack advance Δa_i was calculated by the simple formula [69] :

$$J_I = 2A/B(W-a_0) \qquad (4\text{-}5)$$

where A is the area under the P-Δ curve before the ith unloading sequence, and B is the specimen thickness. A line of J versus Δa was plotted and the J_{Ic} value was defined as the intersection of this line and the blunting line $\Delta a = J/2\sigma_y$. The temperature dependendce of fracture toughness was found by plotting the J_{Ic} values versus the test temperatures.

4-1-3. Uniaxial Compressive Tests

The compression of a cylinder between anvils is an appropriate test for studying the kinetics of strain-induced martensitic transformations. There is no problem with necking and the test can be carried out to strains in excess of 2.0 if the material is ductile. The tests were run in the temperature range from -196 to 160^{o}C at the same strain rates as in tensile tests and stopped at various plastic strains before the failure of specimens.

Buckling and barreling are two common difficulties unless the tests are conducted with caution. Buckling can be eliminated by reducing the aspect ratio L_0/D_0, where L_0, D_0 are the initial height and diameter of the cylindrical specimen, respectively. However, a friction force will exist at the specimen-anvil interfaces. It can lead to a barreled specimen profile and create a cone-shaped region of undeformed material near the anvil surfaces. For a given diameter, a too short cylinder could have an overlap of the undeformed regions after large deformation and is undesirable for the kinetics studies. The overlap of undeformed zones also increases the required axial force for further deformation and the load-displacement curve bends upward [70].

A cylindrical specimen with aspect ratio 1.64 (6.35mm in length and 4.06mm in diameter) was selected according to the results of a series of preliminary tests in which specimens with different values of L_0/D_0 were used and their shapes and microstructures after testing were checked. The friction at the specimen-anvil interface was minimized by applying MoS_2 lubricant on the smooth, hardened surfaces of the anvils. Specimens were uniformly deformed using a self-aligning fixture in which the semispherical top anvil could freely rotate on loading to match the specimen surface. Neither buckling nor barreling occurred in the ranges of applied plastic strain up to 0.45 at the various test temperatures. The values of yield stress and the true stress-true plastic strain curves were calculated from the load-displacement curves.

4-1-4. Microhardness Measurements

Microhardness measurements were made to determine the hardness difference between the martensitic and the austenitic phases of both 0.5Mn and 3.5Mn steels subjected to the aging treatment described in section 3-3. This hardness difference was also determined for the γ'-strengthened 31Ni(L) steel [1]. Before the measurement, the martensitic phase was produced at $-196^{o}C$ either assisted by tensile stress for the two phosphorus-containing alloys or just immersing in liquid nitrogen for the 31Ni(L) steel. Then the samples were polished and lightly etched. The measurements were done using an Akashi microhardness tester with an applied load of 100 g. At least 10 measurements were taken for each sample and their average was used.

4-2 Transformation Kinetics Measurements

In order to quantify the influence of triaxiality on the stability of the austenitic phase, the transformation kinetics with respect to the plastic strain in tension and in compression were measured at temperatures from -196 to $150^{o}C$. The study was only done on the 0.5 Mn-0 alloy, which is the least stable material. For each temperature, specimens were loaded to various plastic strain levels, and then sliced normal to the loading axis to form thin discs with about 15 milligram in weight. For compression specimens, discs were only cut from the middle because of the possible existence of the undeformed zones at the ends of the cylinder. The surfaces of the thin samples were ground using 600 grit SiC paper and well-cleaned in acetone in an ultrasonic cleaner to avoid any contamination of the ferromagnetic material.

The amount of the martensitic phase was determined from the measurement of the saturation magnetization moment. A standard sample with 100% martensite, ascertained from X-ray diffraction and metallography, was prepared by imposing a large tensile plastic strain on a severely overaged 0.5 Mn-alloy (aged at 630^{o}C for 30 hours) at -90^{o}C. Magnetization measurements were performed in a vibrating sample magnetometer (VSM) at room temperature under a magnetic field of 15 kilogauss which was high enough to saturate the magnetization of the thin samples. The martensite volume fraction, $f_{\alpha'}$, is linearly proportional to the magnetic moment of saturation per unit mass, B_s (emu/g), and was calculated as :

$$f_{\alpha'}(\%) = (B_s/B_{s,std.}) \times 100\% \qquad (4\text{-}6)$$

where $B_{s,std.}$ represents the B_s of a standard sample and equals 152.2 emu/g, comparable to the reported value of 304 stainless steel [72,73].

4-3. Microscopy

Optical microscopy was intensively used to examine the general austenitic microstructure, including grain size, cleanliness, and voids; the martensitic morphology after mechanical tests at different temperatures; the fracture profiles in tensile and three-point bending specimens; and the transformation-zone size around cracks at mid-thickness of the three-point bending specimens. Etching for grain size measurements was done by swabbing a reagent of 1 part nitric acid and 2 parts hydrochloric acid for a few seconds. The martensitic phase was revealed by a solution of 0.5 g sodium metabisulfite in 33 ml hydrochloric acid and 167 ml water.

Transmission electron microscopy was conducted on specimens for the observation and identification of second-phase particles, grain boundaries, and other defects. The substructure of specimens subjected to tensile plastic strain was also examined to explore the role played by the second-phase particles on transformation. Preparation of thin foils followed a general procedure : samples 0.25 mm thick were cut from a target material using a water-cooled, low speed SiC cutter and ground by hand to 0.10 mm thick with good surface finishing; 3 mm diameter discs were punched out and then thinned to obtain an electron-transparent condition by double-jet electropolishing in an electrolytic solution consisting of 10% perchloric acid in methanol at a temperature below -35^{o}C. A d.c. power supply was operated at 65 volts and 0.12 amperes. The thin foils were observed in either a JEOL-100C or a JEOL-200CX microscope operated at 120 kV or 200 kV accelerating voltage, respectively. Selected-area diffraction patterns were taken for identification of crystallographic features including precipitates, inclusions, and martensite. Dark-field images utilizing specific diffraction spots were recorded to reveal the distribution and morphology of the subject phases.

An AMR 1000 scanning elctron microscope was employed to study the fracture characteristics of the tensile and the three-point bending specimens. TEM foils were also observed for measuring the volume fraction and X-ray fluorescence spectrum of coarser dispersed particles.

Chapter 5 Results and Discussion

5-1 Microstructure Characterization

Even without the work-hardening effect due to 40% warm rolling, both alloys exhibit remarkable precipitation-hardening behavior. The hardness of both alloys can readily reach R_c45 (Hv 452) from the R_c5 (Hv 190) of the solution treated condition simply by aging at 680°C. In this section, the microstructure of these high-phosphorus steels characterized by TEM, SEM, and X-ray diffraction are discussed and will be used to explain the fracture behavior and mechanical properties. Fig.5-1 illustrates and identifies the general matrix precipitation in the 0.5Mn alloy after the 1150°C/2Hr solution treatment and a 680°C/14Hr aging treatment. The high-magnification bright-field image, Fig. 5-1(a), shows a large number of small spherical particles with diameter ≅ 80Å finely dispersed in the austenitic matrix along with a few individual dislocations. The electron diffraction pattern of the central area in Fig.5-1(a) clearly consists of two superimposed sections of an fcc reciprocal lattice in Fig.5-1(c) and can be indexed as zone [001] of austenite and zone [001] of the complex carbide $M_{23}C_6$, respectively. The dark-field image, Fig.5-1(b), due to the diffraction spot (020) of $M_{23}C_6$, further confirms that the dispersed particles are complex carbides. The crystal structure of carbide $M_{23}C_6$ is identical to that of the austenite and the orientation relationship between two phases can be represented as

$$(001)_\gamma//(001)_{M_{23}C_6},\ [100]_\gamma//[100]_{M_{23}C_6},\ [010]_\gamma//[010]_{M_{23}C_6}$$

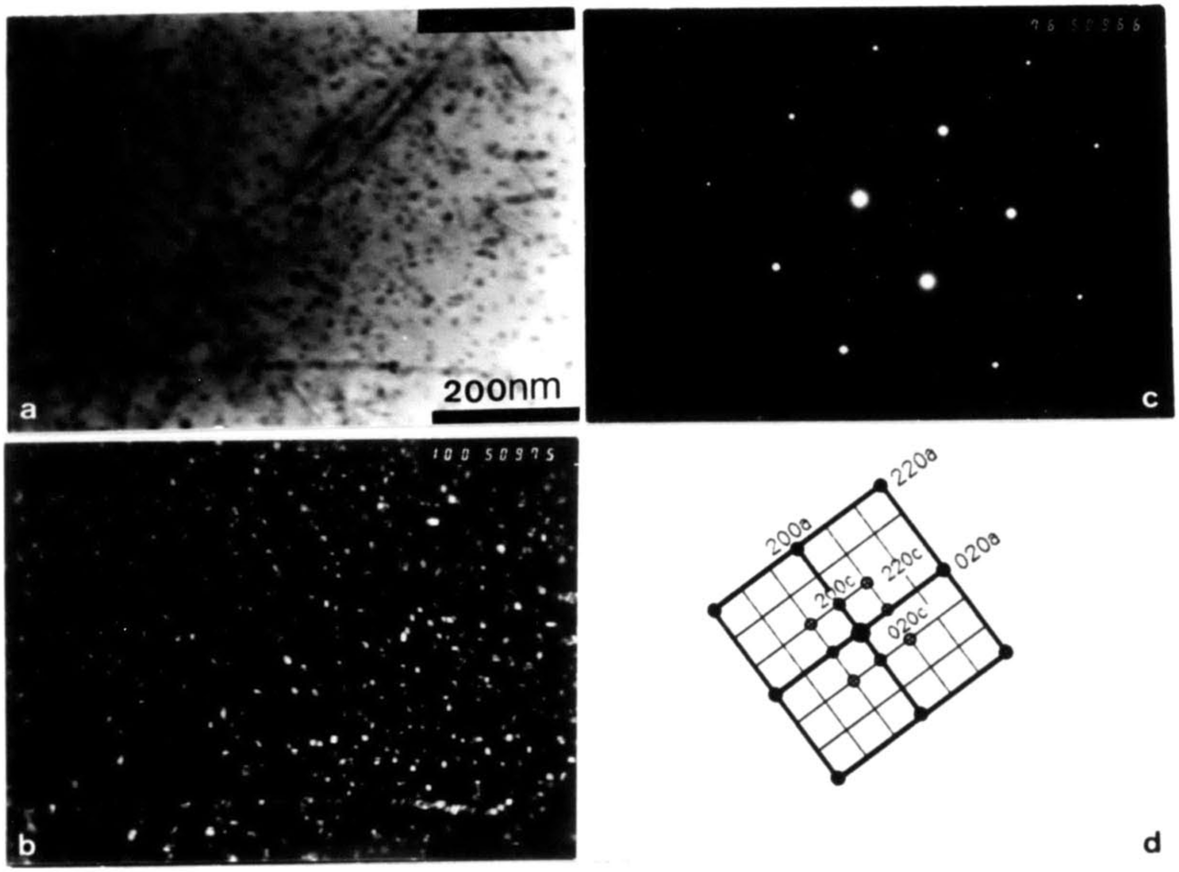

Fig. 5-1 TEM micrographs illustrating the general matrix precipitation in the 0.5Mn alloy, solution treated at 1150°C for 2 hours and aged at 680°C for 14 hours. a). Bright-field image, showing finely dispersed equiaxed particles with diameter ≅ 80A and few dislocations. b). Dark-field image from diffraction spot (020) of $M_{23}C_6$ carbide. Contrast reversion confirms the particles are $M_{23}C_6$ carbides. c). and d). are an electron diffraction pattern from the central area of a). and its indexing, showing $[001]_{\gamma}//[001]_{carbide}$.

according to the diffraction patterns. A few lath-like $M_{23}C_6$ precipitates on {111} matrix planes were also found in some areas as shown in Fig.5-2. The lattice parameter of $M_{23}C_6$ is very close to three times of that of the matrix shown in the diffraction pattern, and so it is likely that a high degree of coherency can be maintained with respect to a high coincidence between two lattices. Using the measured lattice parameters (a_γ and $a_{M_{23}C_6}$) of austenite and carbides in Table 3-3 and 5-1, the misfit which is defined as $[(3a_\gamma - a_{M_{23}C_6})/3a_\gamma]$ are between $2 \cdot 10^{-4}$ and 10^{-2}. Because of this small isotropic misfit, coherent carbides can easily precipitate out of the matrix with an equiaxed shape rather than in grain boundaries. Apparently, those finely dispersed carbide precipitates are able to effectively impede dislocation motion, which accounts for the observed age hardening behavior.

Next, we discuss the effect of warm rolling on the substructure. Fig.5-3 shows that the typical microstructure of the as-rolled 0.5Mn alloy contained a high density of dislocations as well as shear bands, similar to the microstructure of a deformed 304 stainless steel [71]. However, most of the shear bands disappeared during the subsequent aging treatment because the aging temperatures, 600-630^oC, were sufficiently high to activate recovery in the highly deformed local regions, viz. part of the work hardening effect was eliminated. This observation can explain the fact that the hardening contributions from warm rolling ($\Delta R_C \cong 25$) and from aging ($\Delta R_C \cong 40$) on the final hardness ($R_{C\ max.} = 50$) of the warm rolled and aged alloys are not additive.

The microstructure around grain boundaries was carefully examined in the rolled and aged condition. There was no strong evidence supporting the

Fig. 5-2 Some plate-like $M_{23}C_6$ precipitates on {111} matrix planes were found in the 0.5Mn alloy, solution treated at 1150^{0}C for 2 hours and aged at 680^{0}C for 14 hours.

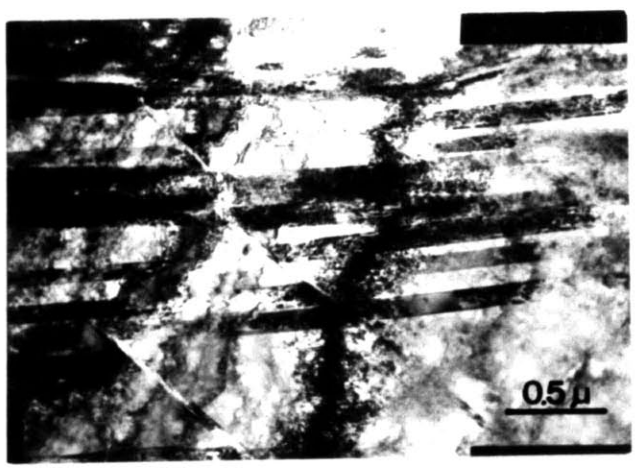

Fig. 5-3 Microstructure of the solution treated and warm rolled 0.5Mn alloy showing the present of shear bands and high-density dislocations.

existence of a grain boundary precipitate-free zone (PFZ), as shown in Fig.5-4. PFZs can reduce the bonding strength between grains and the corrosion resistance around grain boundaries. There are two causes to promote the formation of PFZs [73]. The nucleation and growth of grain boundary precipitates during cooling from the solution treatment temperature may cause solute to be drained from the surrounding matrix and a PFZ results. Another cause of PFZ can be due to vacancy diffusion to grain boundaries during quenching so that the vacancy concentration is drastically lowered in the vicinity of grain boundaries. This will reduce the diffusion rate of solute in the vicinity of grain boundaries at the aging temperature and then no precipitate can nucleate even though the concentration of solute is largely unchanged. In the present work, a high cooling rate after the solution treatment was obtained by hanging the alloy bars with small cross section in a vertical furnace and directly dropping them into a cold water bath. This fast quenching is capable of avoiding preferential formation of precipitates on grain boundaries as well as losing vacancies around grain boundaries, thus suppressing the formation of PFZs.

The precipitate morphology in the warm-rolled and underaged 3.5Mn-U and 0.5Mn-U alloys is shown in Fig. 5-5 and 5-6, respectively. Diffraction patterns again indicated no other precipitate formed except $M_{23}C_6$ carbides. Only dark-field images (Figs.5-5(c), 5-6(b)) taken from the diffraction spot of carbide particles can clearly show the precipitate morphology; there is contrast interference from entangled dislocations in bright-field images (Figs.5-5(a),5-6(a)). High dislocation density in the preaged microstructure brings two benefits. One is a lowering of the energy barrier for precipitate nucleation and hence the required aging temperature; the other is to further

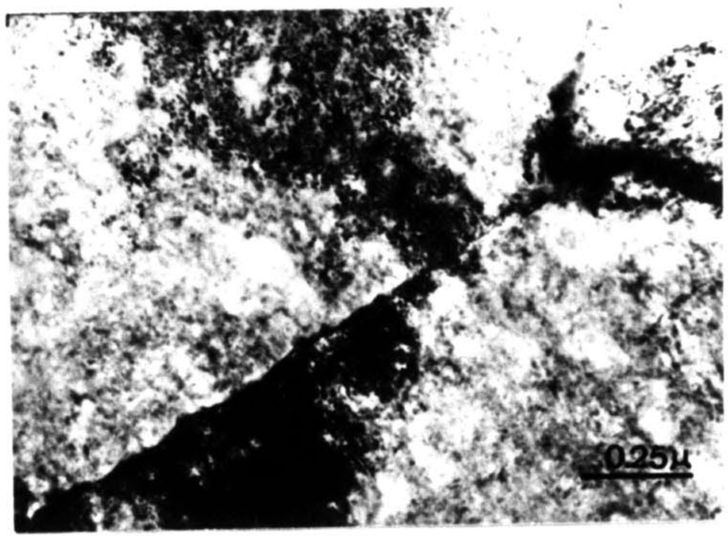

Fig. 5-4 No precipitate-free zones were found in the vicinity of grain boundaries in the overaged 0.5Mn alloy.

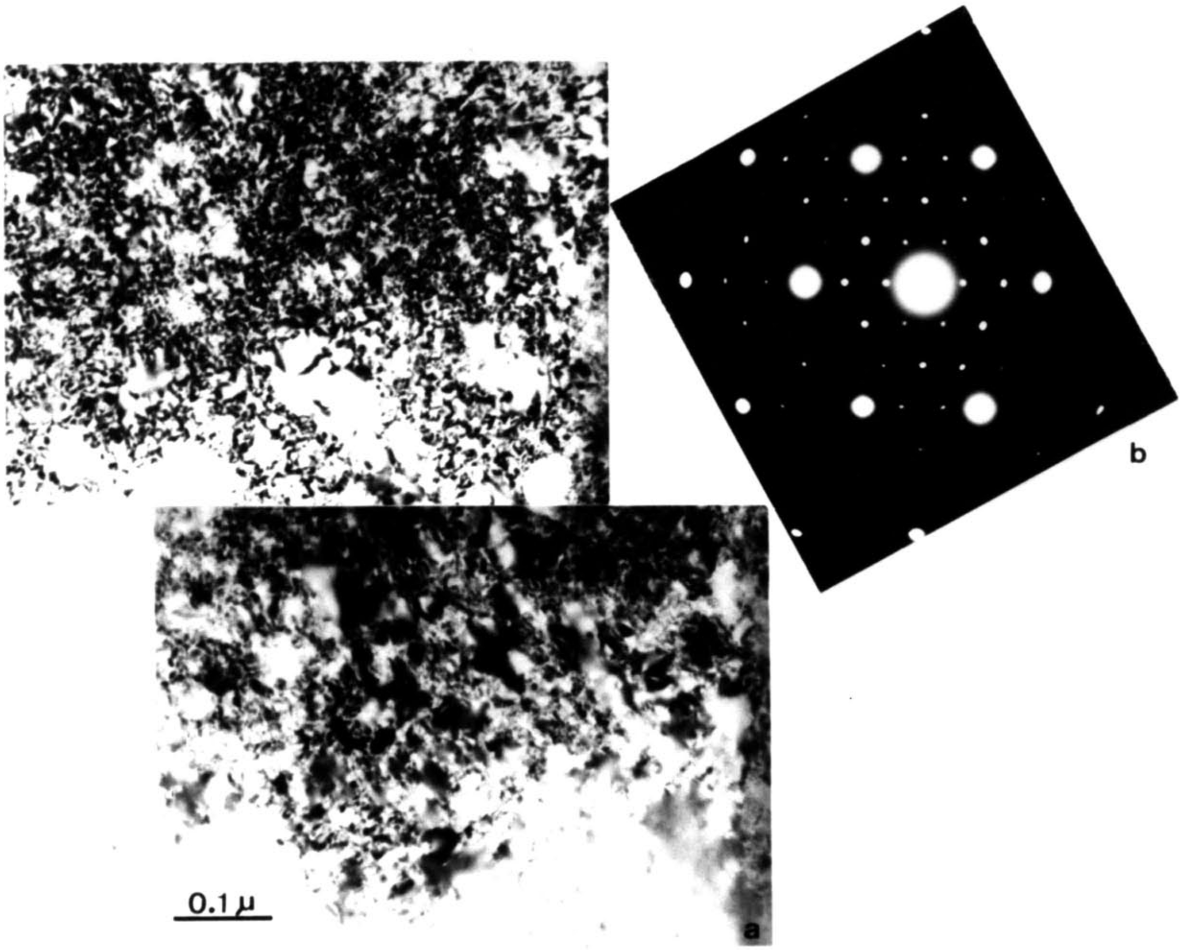

Fig.5-5 TEM micrographs showing the morphology and distribution of carbide precipitates in underaged 3.5Mn alloy. a). Bright-field image. It does not clearly reveal the morphology of precipitates because of contrast interference from dislocations. b). Electron diffraction pattern, indexed as $[114]_{\gamma}//[114]$ of $M_{23}C_6$.

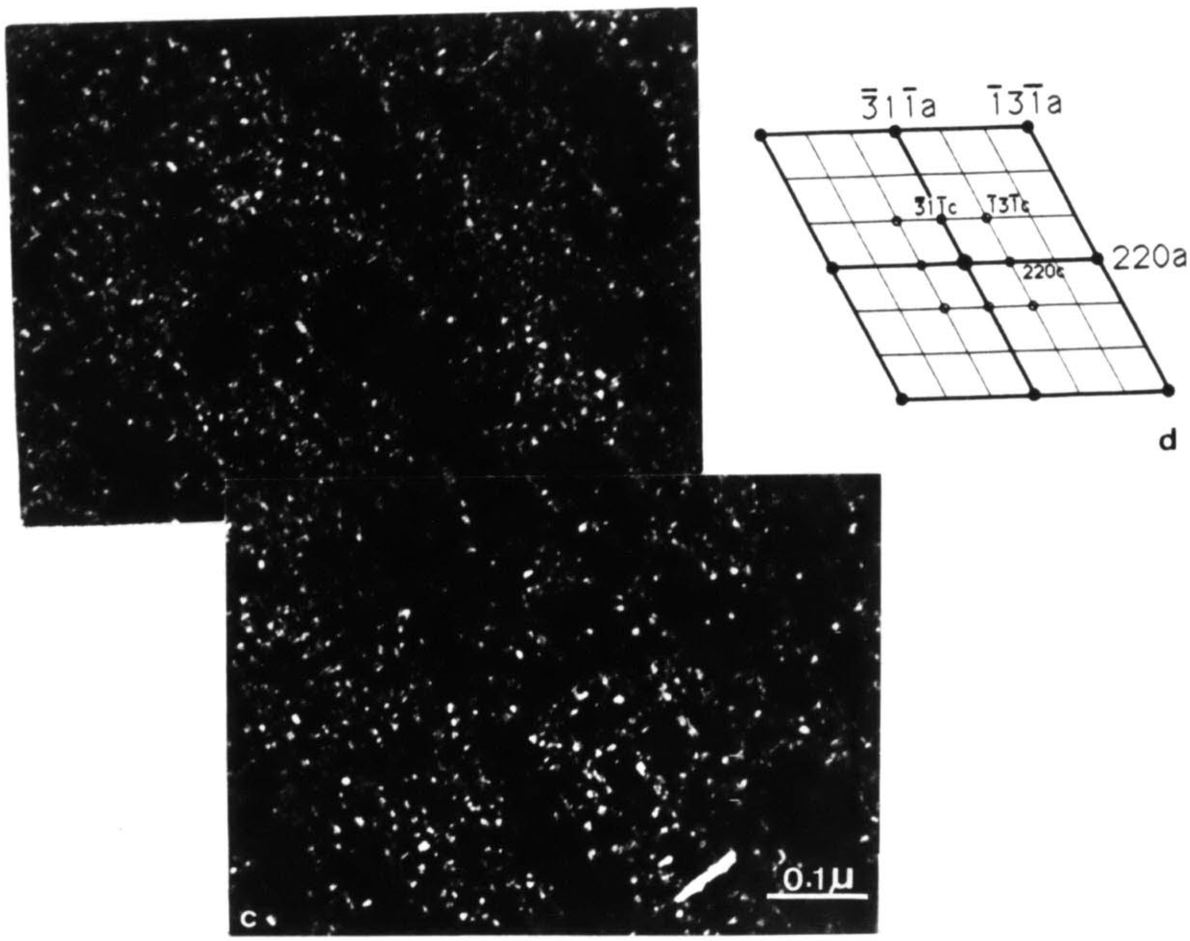

Fig.5-5 c). Dark-field image from diffraction spot (220) of $M_{23}C_6$.

d). Indexing of diffraction pattern.

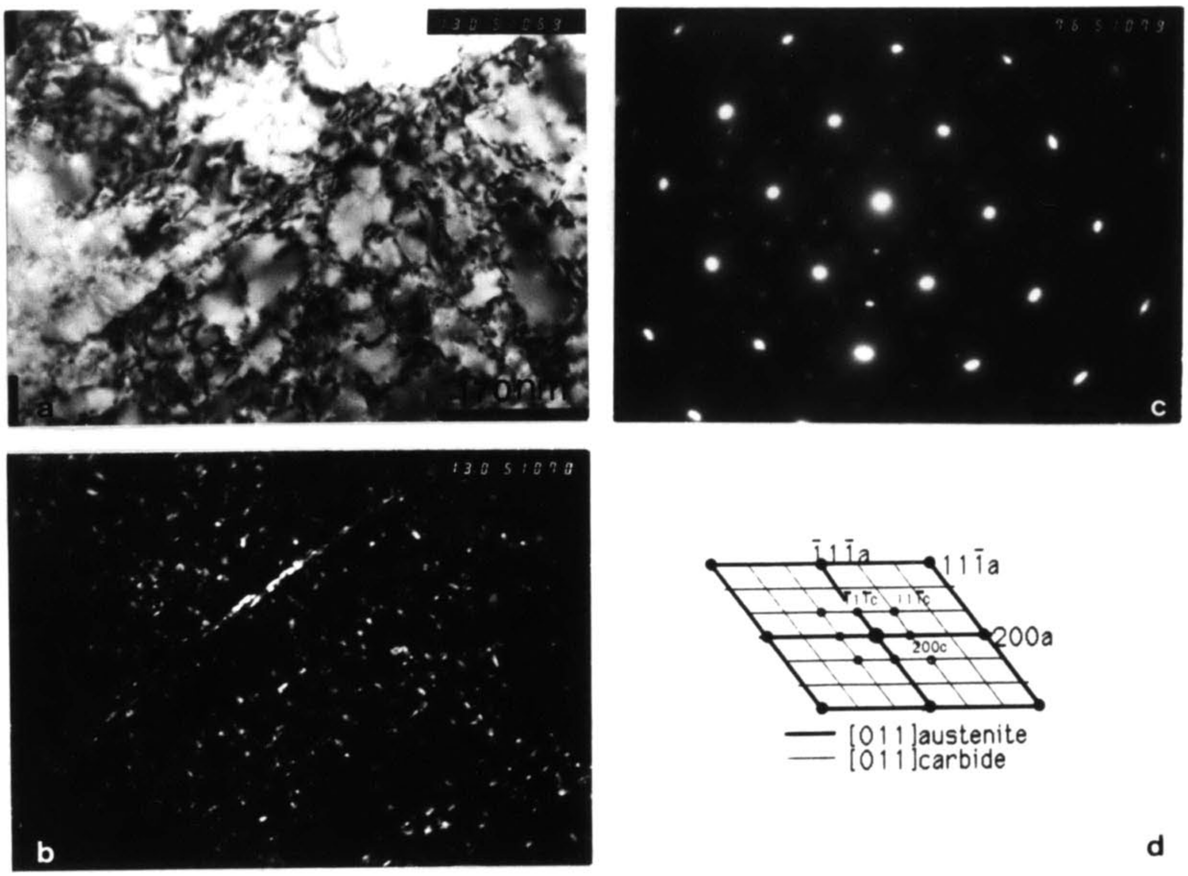

Fig.5-6 TEM micrographs showing the morphology and distribution of carbide precipitates in underaged 0.5Mn alloy. a). Bright-field image. b). Dark-field image from diffraction spot (020) of $M_{23}C_6$. Carbide precipitates tend to sit on dislocations or array themselves along a "diffuse" shear band boundary. c). and d). are electron diffraction pattern and its indexing, indicating $[011]_{\gamma}//[011]$ of of $M_{23}C_6$.

reduce the possibility of forming grain boundary PFZs because dislocations are also fast diffusion paths for solutes. Comparing the dark-field and the bright-field images, carbide particles are found to sit on dislocations or array themselves along "diffuse" shear band boundaries (Fig.5-6(b)) that means the defects introduced by warm rolling became the preferential nucleation sites for the precipitates. In Fig.5-5(c) and 5-6(b), finer precipitates (average diameter ~65Å) with denser dispersion are found in the warm-rolled alloy as a result of lower aging temperature, and can provide better strengthening effect.

Banerjee et al. [2] studied the effect of phosphorus on the composition of carbide precipitates in three heats of 18Cr-10Ni-4Mn stainless steel with 0.3% carbon at 70 ppm, 0.28% and 0.38% phosphorus levels. They found that phosphorus in the precipitated $M_{23}C_6$ carbides increases with more advanced aging, and with increased phosphorus content of the steel, while the lattice parameter decreases. Thus, based on the relative atomic sizes of Cr, Fe, P and C, they suggested substitutional rather than interstitial positioning of the phosphorus atoms in the $M_{23}C_6$ structure, indicating that the carbides should be labeled $(Cr,Fe,P)_{23}C_6$ instead of $(Cr,Fe)_{23}(C,P)_6$.

X-ray diffraction using Cr K_α radiation was performed to determine the lattice parameters of α', γ, and $M_{23}C_6$, thereby permitting calculation of the atomic volume change due to the deformation-induced martensitic transformation after various aging treatments. The lattice parameter values of $M_{23}C_6$ are listed in Table 5-1 along with Banerjee's X-ray microanalysis data. The aging-treatment dependence of the $M_{23}C_6$ lattice parameter in the 0.5Mn alloy followed the same trend as Banerjee's results.

Table 5-1. Composition and Lattice Parameter of Carbide

Alloy	Heat Treatment, °C/Hr	Composition	Lattice Parameter, Å
A*	704/16 (aged)	$(Cr_{.64}Fe_{.36})_{23}C_6$	-------
	760/16 (aged)	$(Cr_{.782}Fe_{.208}P_{.01})_{23}C_6$	-------
	1150/.5 (annealed)	$(CrFe)_{23}C_6$	-------
B*	704/16 (peak hardness)	$(Cr_{.770}Fe_{.196}P_{.034})_{23}C_6$	-------
	760/16 (overaged)	$(Cr_{.751}Fe_{.183}P_{.066})_{23}C_6$	-------
	1150/.5 (annealed)	$(Cr_{.50}Fe_{.217}P_{.283})_{23}C_6$	-------
C*	704/16 (peak hardness)	$(Cr_{.730}Fe_{.213}P_{.057})_{23}C_6$	-------
	760/16 (overaged)	$(Cr_{.652}Fe_{.196}P_{.152})_{23}C_6$	10.610
	1150/.5 (annealed)	$(Cr_{.50}Fe_{.217}P_{.283})_{23}C_6$	10.597
0.5Mn	530/3+600/12 (underaged)	-------	10.750
	630/19 (overaged)	-------	10.696
	630/30 (overaged)	-------	10.614
3.5Mn	530/3+630/12 (underaged)	-------	10.726

*--- Steels used in Banerjee's work [2], their chemical compositions (wt.%) are :

A--- 18.2Cr-9.6Ni-3.65Mn-0.31C-0.007P

B--- 18.0Cr-9.5Ni-3.59Mn-0.32C-0.28P

C--- 17.7Cr-9.5Ni-3.59Mn-0.33C-0.38P

It implies that the overaging treatment should deplete phosphorus from the austenitic matrix because of forming higher phosphorus-containing carbides. This could reduce the potentiality of intergranular fracture since phosphorus is a well-known element causing grain boundary embrittlement in high-strength steels.

Argon et al. [35] pointed out that void nucleation due to external stress tends to occur for particles larger than 100Å in diameter when a critical interfacial stress condition is reached. Therefore, the extremely fine carbide precipitates (< 80Å) in diameter should not be responsible for void nucleation as the initial stage of the ductile fracture process. Work by Hsu [74] indicated that simple sulfide, oxysulfide, and oxide particles with diameter 0.1 to 0.7 µm provide grain-coarsening resistance for RSP M-2 matrix steel at austenitizating temperatures up to 1220°C. At 1260°C, simple sulfides and oxysulfides were dissolved in the matrix and oxides became the dominant stable particles, while the grain growth rate markedly increased. In the present work, SEM was used to search for second-phase particles other than carbide precipitates by observing electropolished thin foils .

Two types of particles were found and defined according to the size and distribution, as follows : Particles of the first type with average diameter 0.15 µm (ranging from 0.1 to 0.5 µm) and volume fraction about 0.12% are well dispersed in the 0.5Mn-0 alloy as shown in Fig.5-7(a), where we can see many of them located at the grain boundaries. The estimated volume fraction, size, and distribution are consistent to those of grain refining particles found in some RSP steels [74,75]. Owing to the poor image contrast presented by the small particles, the size and volume fraction were determined by outlining all the particles in 20 fields on tracing paper, and then measuring the maximun chord length and the area fraction in an image analyzer. The X-ray spectrum (Fig.5-7(b)) of a particle indicated by an arrow in Fig.5-7(a) shows a high Al-peak. The other peaks are believed to come from the matrix and the Au surface coating layer as a result of a much larger X-ray activated volume than the particle. The crystallographic structure of the grain-refining particles was identified by electron diffraction as hcp α-Al_2O_3 with lattice parameters a_0=4.76 A and c_0=12.99 A (c_0/a_0=2.73), as shown in Fig.5-8.

Particles of the second type have larger diameters from 0.5 to 3 μm with directional alignment along the extrusion axis, as revealed in Fig.5-9. They presented the same X-ray spectrum as in Fig.5-7(b). In general, these particles appear in groups and concentrate in small regions, similar to the morphology of Type IV oxide inclusions in steels. According to the microanalysis results and the morphology, they are aluminum oxide, too. The overall volume fraction was in the order of 0.1% but difficult to quantify due to the very inhomogeneous distribution. This second type of particle would be the primary void former because both larger particle size and localized distribution, compared to the grain-refining particles, favor void nucleation [76]. Thus, the formation of alumina particles like inclusion colonies is undesirable in view of their known deleterious effect on the fracture toughness.

Some significant conclusions may be drawn from the above experimental results : l). The outstanding age-hardening behavor originates from the

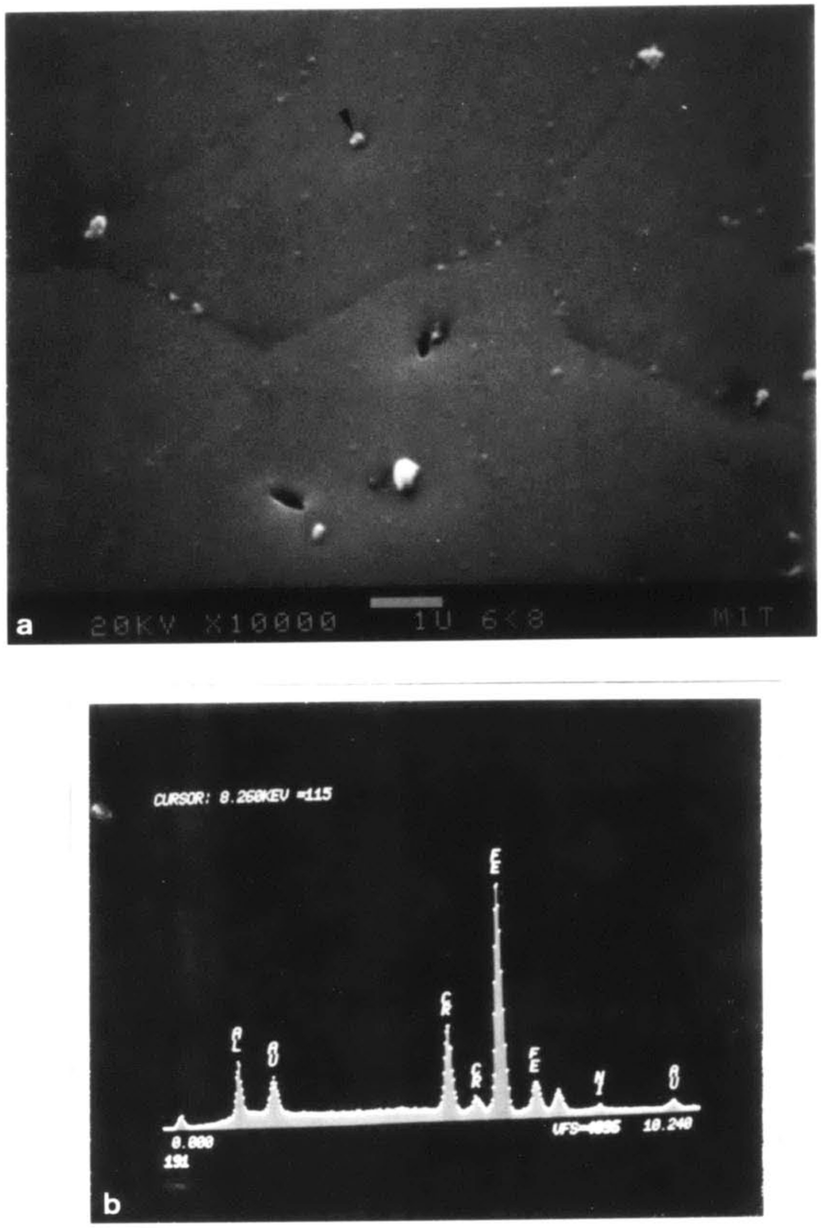

Fig.5-7 a). SEM secondary electron image recorded from an electropolished surface of the overaged 0.5Mn alloy, showing the distribution of the grain refining particles with diameter 0.1 to 0.5 µm. Two particles fell out during electropolish and formed pores. b). X-ray spectrum from the arrow-designated particle indicates the presence of Al-peak. Other peaks are from the matrix and surface coating layer.

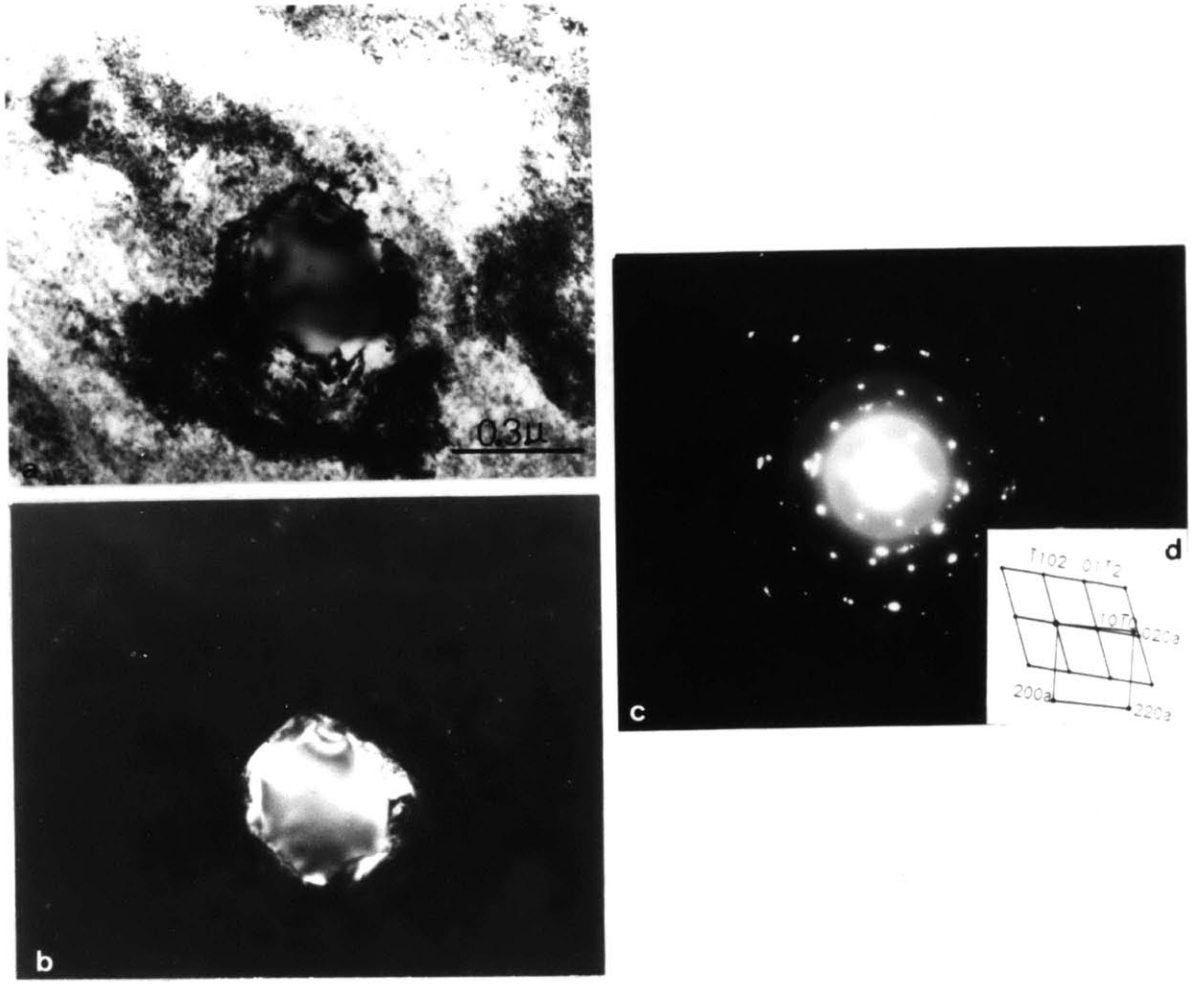

Fig.5-8 TEM micrographs identify the structure of grain refining particles as α-Al_2O_3. a). Bright-field image. b). Dark-field image from diffraction spot (0112) of α-Al_2O_3. c). and d). are the electron pattern and its indexing, including zone [2423] of α-Al_2O_3 and zone [001] of austenite.

Fig.5-9 SEM secondary electron image showing alumina colony in 0.5Mn-0 alloy.

finely dispersed coherent phosphocarbide precipitates with diameter $< 80\text{Å}$. 2). No grain-boundary precipitate or PFZ was found. 3). Lower phosphorus content in the matrix is expected for longer aging times because more phosphorus is gettered in the precipitated carbides. 4). Two types of alumina particles exist in the RSP alloys and are expected to control grain refining and void nucleation.

5-2 Transformation Stability

5-2-1 Temperature Dependence of Yield Stress and Transformation Temperature

The M_s^σ temperature of a metastable austenite is defined as the maximum temperature at which transformation is induced by a stress below the yield stress of the parent phase [3,4]. It can be recognized as an invariant property at a given stress-state and strain rate. As demonstrated by Patel and Cohen [25], the thermodynamic assist of an externally applied stress, $\partial \Delta G/\partial \sigma$, and hence the M_s^σ temperature is a function of stress-state due to the contribution of the transformation volume change. It implies that the change of austenite stability under the different loading conditions of commonly used mechanical testing methods can be reflected by the shift of M_s^σ temperature. Experimental work done by Leal [1] showed that the M_s^σ temperature of γ'-strengthened TRIP steels increased with the stress-states corresponding to uniaxial tension, tensile necking (formed in the later stage of uniaxial tensile test), and a crack-tip. The determination of the M_s^σ temperature is affected by the nature of mechanical testing method and is not always straightforward. In the cases of uniaxial tension and uniaxial compression, the M_s^σ temperatures are well-defined values because the material within the gage length is under a constant stress-state and can be directly measured from the temperature dependence of yield stress according to its definition. On the other hand, an "effective" M_s^σ temperature can only be roughly determined for a tensile neck or a crack-tip from the martensitic morphology due to the gradient of stress-state.

Another characteristic temperature related to the stability is called M_d, defined as the highest temperature at which transformation can be induced by deformation. Comparing with M_s^σ temperature, M_d is not an univariant property for a metastable austenite at a fixed stress-state because it also depends on the extent of plastic deformation imposed on the material.

In order to distinguish the transformation temperatures M_s^σ and M_d under different stress-states, we have added the abbreviations UC, UT, N, and CT to represent uniaxial compression, uniaxial tension, tensile neck, and crack-tip, respectively. For example, the M_s^σ temperature in uniaxial tension is designated as M_s^σ(UT).

Fig.5-10 shows the tensile yield stress vs. test temperature curves of the 0.5Mn-O, 0.5Mn-U, and 3.5Mn-U alloys measured by using multiple specimens. Within the range of test temperatures, all three cases exhibited a significant drop of yield stress when the deformation was dominated by transformation. Such curves allow interpolation to accurately determine M_s^σ(UT) at the peak stress under uniaxial tension as 53°C, -24°C, and -105°C for the 0.5Mn-O, 0.5Mn-U, and 3.5Mn-U alloys, respectively, and indicated by arrows in Fig.5-10. The measured M_s^σ(UT) temperatures suggested that the austenite stability of this carbon-containing alloy system not only can be controlled by the minor composition modifications but also by changing the aging condition. The latter is an important benefit for the practical application of TRIP steels because the optimum toughness enhancement due to transformation can be controlled to occur in the service temperature range simply by changing the aging process without significantly losing strength. In preliminary experiments, a more convenient

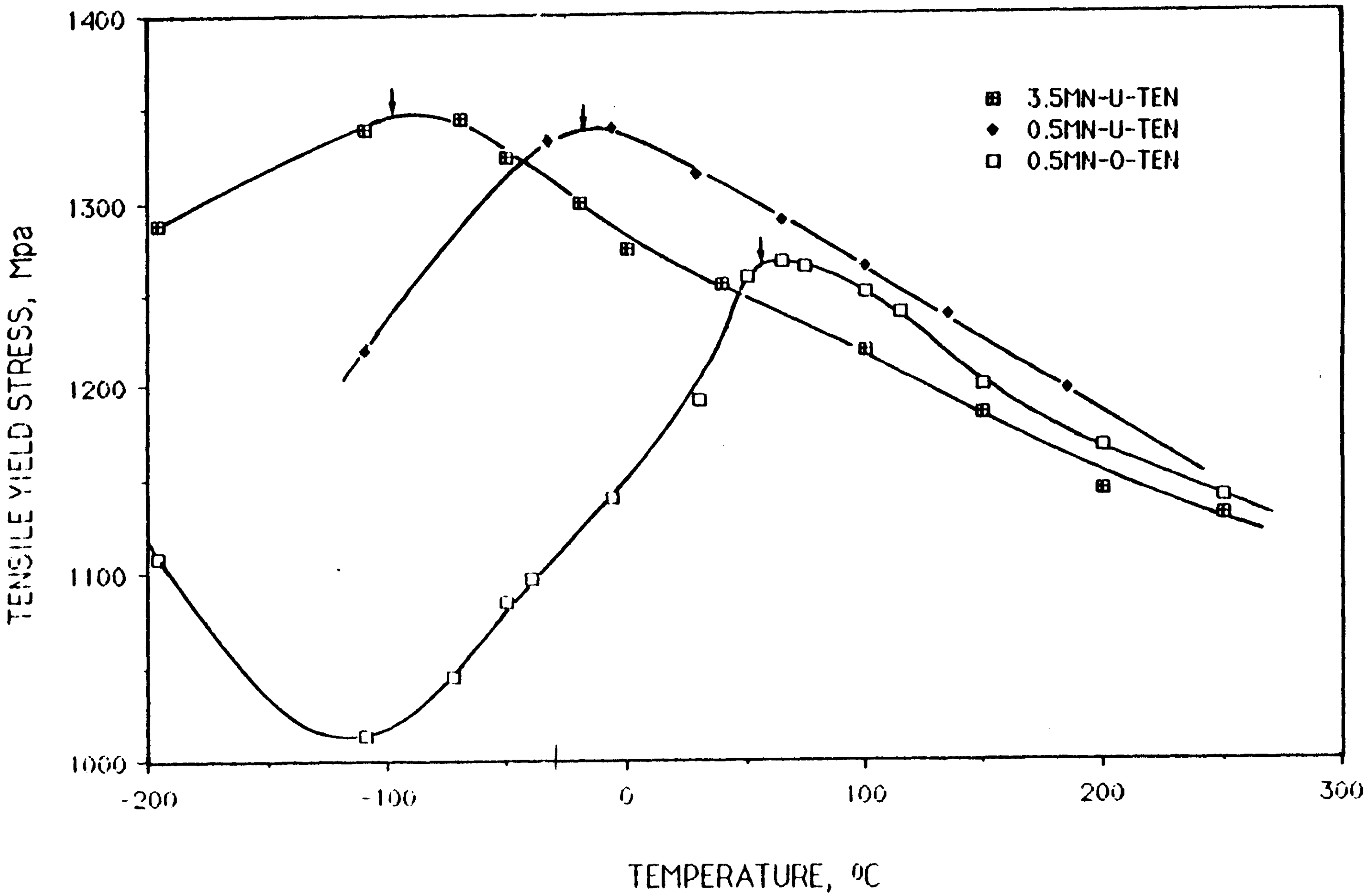

Fig. 5-10 Temperature dependence of 0.2% tensile yield stress of 3.5Mn-U, 0.5Mn-U, 0.5Mn-O alloys M_s^{σ} temperatures in uniaxial tension are indicated by arrows. $\dot{\varepsilon}$ = 0.02 min^{-1}.

single-specimen technique developed by Richman and Bolling [4] (where loading-unloading cycles were performed at sequentially decreasing temperatures until a load drop was found) was applied to determine the M_s^{σ} temperature of the 0.5Mn-0 alloy in tension. The results were about 20^{0}C lower than the value determined for the multiple specimen tests.

Examining the values of yield stress at 250^{0}C (to avoid the effect of transformation), the austenitic phases in all three cases posses a similar strength level and meet one of the objectives of the aging treatment. At temperatures below the M_s^{σ}(UT) temperature, the observed yield stress for the 0.5Mn-0 alloy first decreases linearly, passes through a minimum point, and then increases with decreasing temperature. The curvature arises from nonlinearity of the transformation chemical free-energy change vs. temperature at low temperatures and will be discussed later. It is believed that the yield stress values of the other two alloys will present the same type of temperature dependence but the minima occur at temperatures below -196^{0}C.

Following a similar procedure, the M_s^{σ} temperature of the 0.5Mn-0 alloy under uniaxial compression was measured as 2^{0}C using the same strain rate as in the tensile tests. Assuming that the difference between M_s^{σ}(UC) and M_s^{σ}(UT) is a constant, the M_s^{σ} temperatures in compression for 0.5Mn-U and 3.5Mn-0 are estimated as -75 and -156^{0}C.

Fig.5-11 shows the temperature dependence of yield stress in compression and in tension at two strain rates differing by 10^2, where the lower strain rate was only applied in the stress-assisted regime. Some

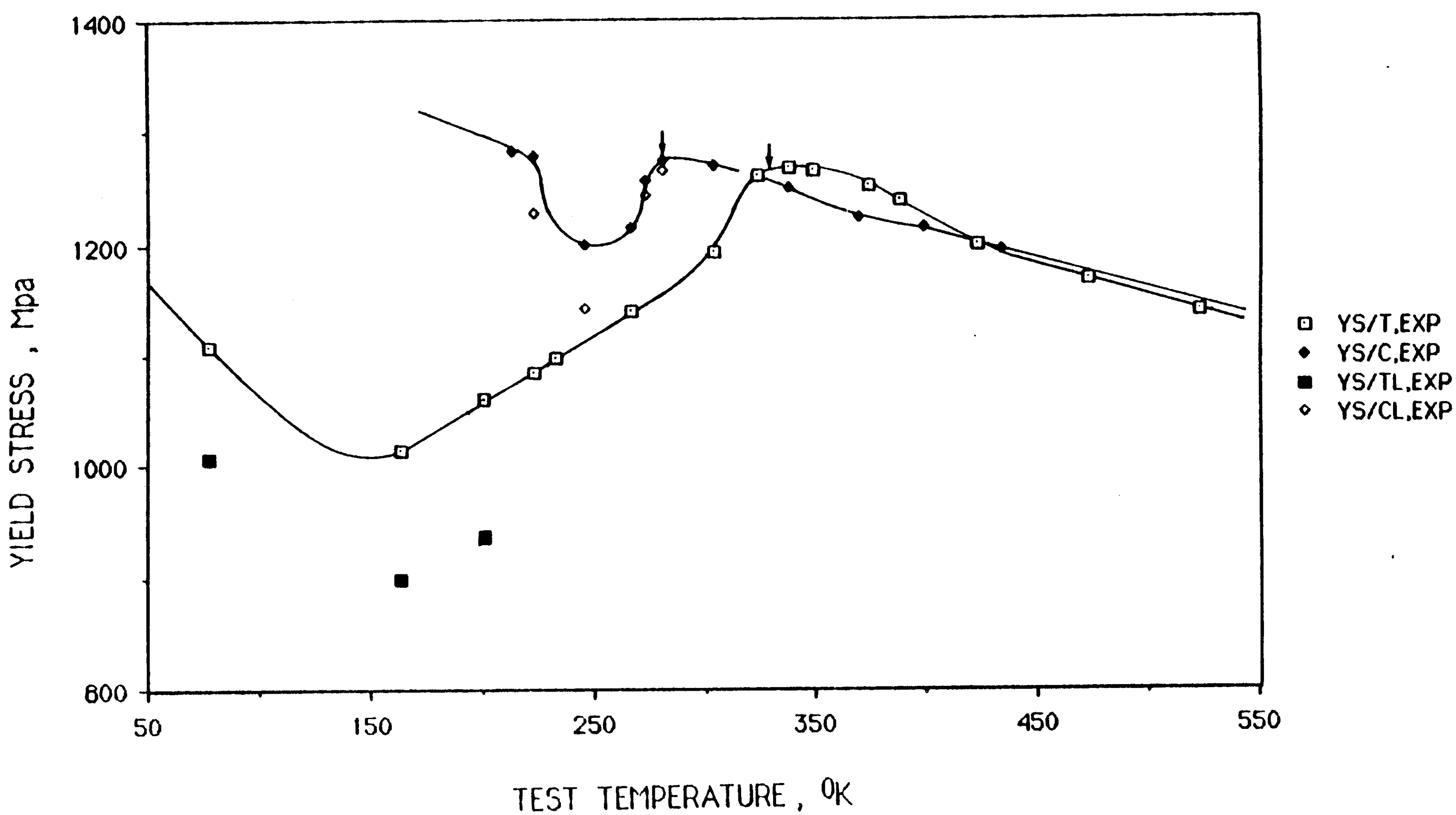

Fig.5-11. Comparison of temperature dependence of yield stress in tension and compression for 0.5Mn-0 alloy tested at same strain rate 0.02 min^{-1} (shown by solid curves). Yield stresses below M_s^{σ} at lower strain rate 0.0002min^{-1} are also presented.

parameters related to isothermal martensitic nucleation will be calculated using yield stresses at both strain rates. Comparing the flow stress in tension and in compression, the compressive yield stress drop due to the transformation is much less pronounced and covers a much narrower temperature range. Below -50°C (223°K) a large strength-differential (S-D) effect is found. Metallographic observation of the specimens subjected to a small plastic strain below -50°C revealed mixed martensite morphologies (plate and lath) in compression, but only plate martensite in tension. It suggests that flow is entirely controlled by transformation in tension, but partially by slip in compression. Above 150°C (423°K) where slip controls flow in both tension and compression, a normal S-D effect is found. However, in the temperature range betwen 50°C (323°K) and 150°C, the tensile flow stress is higher than the compressive value although slip controls the flow in both tension and compression. This anomalous (negative) S-D effect has been attributed to pre-transformation strengthening due to the influence of lattice metastability on dislocation mobility [26].

The M_s^{σ} temperature at a crack-tip was estimated on the basis of martensitic morphology. The strain-induced lath martensite prevails above the M_s^{σ} temperature, while the stress-assisted plate martensite is predominant below the M_s^{σ}(CT) temperature. As mentioned before, the triaxiality around a crack-tip is not a constant but varies with position, and corresponding the M_s^{σ}(CT) temperature. Thus, the observed value is considered to be an "effective" temperature and is bracketed by the two most adjacent test temperatures at which the transition of martensitic morphology can be seen.

In the case of the tensile neck, it is difficult to determine the M_s^σ temperature by metallography due to the following factors : 1). the existence of a stress-state gradient; 2). the influence of fracture strain on the geometry of the necked region and hence the stress-state; since the ratio between the diameter of the minimum cross-section and the curvature of radius in the neck is a function of the fracture strain and this is sensitive to test temperature for a given metastable austenite, the measurements were forced to be conducted at different stress-states. 3). the very high martensite volume fraction existing near the fracture surface interferes with the determination of the martensitic morphology. Fortunately, the measured or estimated M_s^σ(UT) and M_s^σ(CT) offer a chance to predict the M_s^σ temperatures in the tensile neck for all three alloys. The procedures are demonstrated in Fig.5-12 for the 0.5Mn-0 alloy. The stress-state at the minimum cross-section of the neck was first calculated from the axial plastic strain using the Bridgman correction [72], and then the line connecting M_s^σ(UT) and M_s^σ(CT) was extended to higher stress-states corresponding to the fracture strains in the range of 0.56 to 0.85 for the 0.5Mn-0 alloy. The predicted M_s^σ(N) for 0.5Mn-0 is expressed by a temperature interval of 70-76^{0}C which represents the possible lowest and highest M_s^σ(N), respectively, accounting for the fracture strain variation. The triaxiality increment due to necking is small (from 0.333 to 0.637) as can be seen in Fig.5-12 so that using a linear extrapolation to estimate M_s^σ(N) would be reasonable. Here, we should mention that the effect of transformation on the geometry of tensile neck [78] was neglected.

The M_d temperatures for each stress-state have been also determined from metallographic observation and expressed by a temperature interval.

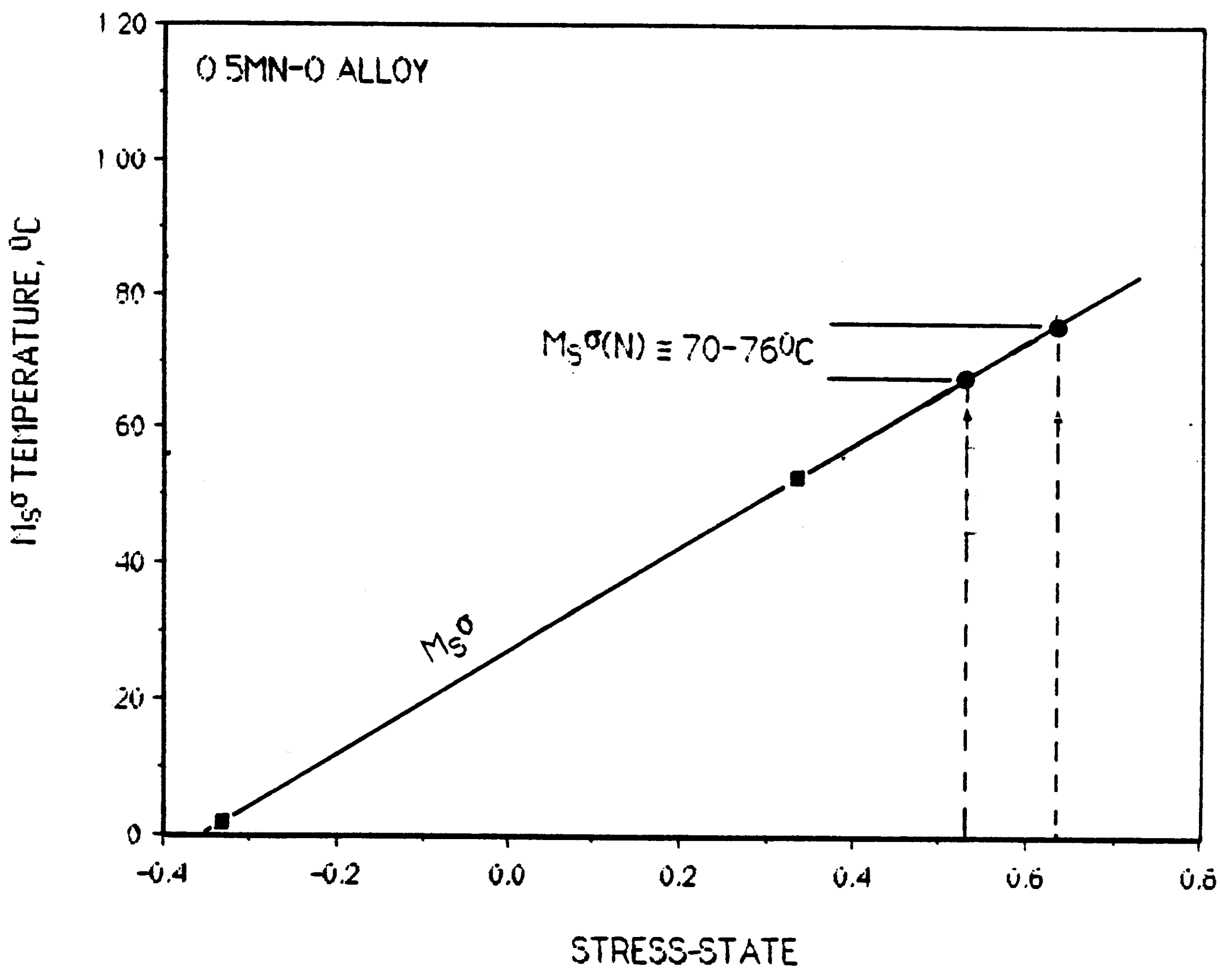

Fig.5-12. M_S^{σ} temperature in a tensile neck ($M_S^{\sigma}(N)$) is determined from the extrapolation of $M_S^{\sigma}(UT)$ and $M_S^{\sigma}(UC)$ by calculating the stress-state corresponding to the fracture strain.

All measured or estimated transformation temperatures are summarized in Table 5-2.

The observed tensile yield stress vs. temperature curve below $M_s^{\sigma}(UT)$ for the 0.5Mn-0 alloy passes through a minimum at about $-120^{\circ}C$ and exhibits a smooth "U" shape. The minimum is consistent with the isothermal transformation behavior of some austenitic steels which present suppressible C-curve kinetics [23]. We have applied the kinetics of isothermal martensitic nucleation and the thermodynamic contribution of applied stress to calculate the temperature dependence of transformation stress under various stress- states and then $M_s^{\sigma}(UC)$, $M_s^{\sigma}(UT)$, and $M_s^{\sigma}(CT)$ were estimated on this basis.

The chemical free-energy change, ΔG_{ch}, for the 0.5Mn-0 alloy was calculated from available thermodynamic data [79] and is plotted vs. temperature in Fig.5-13. The additional thermodynamic assist of the applied tensile stress was calculated as $\Delta G_{mech} = \sigma_y \times (\partial \Delta G / \partial \sigma)$, where the tensile yield stresses σ_y for 0.5Mn-0 were measured at two strain rates in Fig.5-11, and $\partial \Delta G / \partial \sigma$ equals -0.86 J/mole-Mpa in uniaxial tension for the most favorably oriented nuclei according to the Patel and Cohen estimate [25]. The summation of ΔG_{ch} and ΔG_{mech} represents the critical transformation free-energy change ΔG_{crit} required to obtain a fixed rate of transformation f. As will be shown in the next section, f is linearly related to strain rate $\dot{\varepsilon}$ with proportionality being 0.08 for the 0.5Mn-0 alloy. The ΔG_{crit} vs. temperature curves corresponding to strain rates of 0.02 and 0.0002 min^{-1} are indicated by two straight lines with different slopes emanating from a common point at $0^{\circ}K$, as shown in Fig.5-13. A linear relation of ΔG_{crit}

Table. 5-2. Transformation Temperatures

	0.5Mn-O	0.5Mn-U	3.5Mn-U
M_s^σ(UC)	2°C	-75°C	-156°C
M_d(UC)	> 126°C	---	---
M_s^σ(UT)	53°C	-24°C	-105°C
M_d(UT)	175 ± 25°C	117 ± 17°C	-10 ± 10°C
M_s^σ(N)	73 ± 3°C	-5 ± 3°C	-82 ± 3°C
M_d(N)	225 ± 25°C	160 ± 15°C	70 ± 30°C
M_s^σ(CT)	113 ± 12°C	75 ± 25°C	-13 ± 12°C
M_d(CT)	225 ± 25 °C	175 ± 25°C	~ 85°C
M_s^σ(UC)calc.	~ -115°C	---	---
M_s^σ(UT)calc.	~ 35°C	---	---
M_s^σ(CT)calc.	~ 200°C	---	---

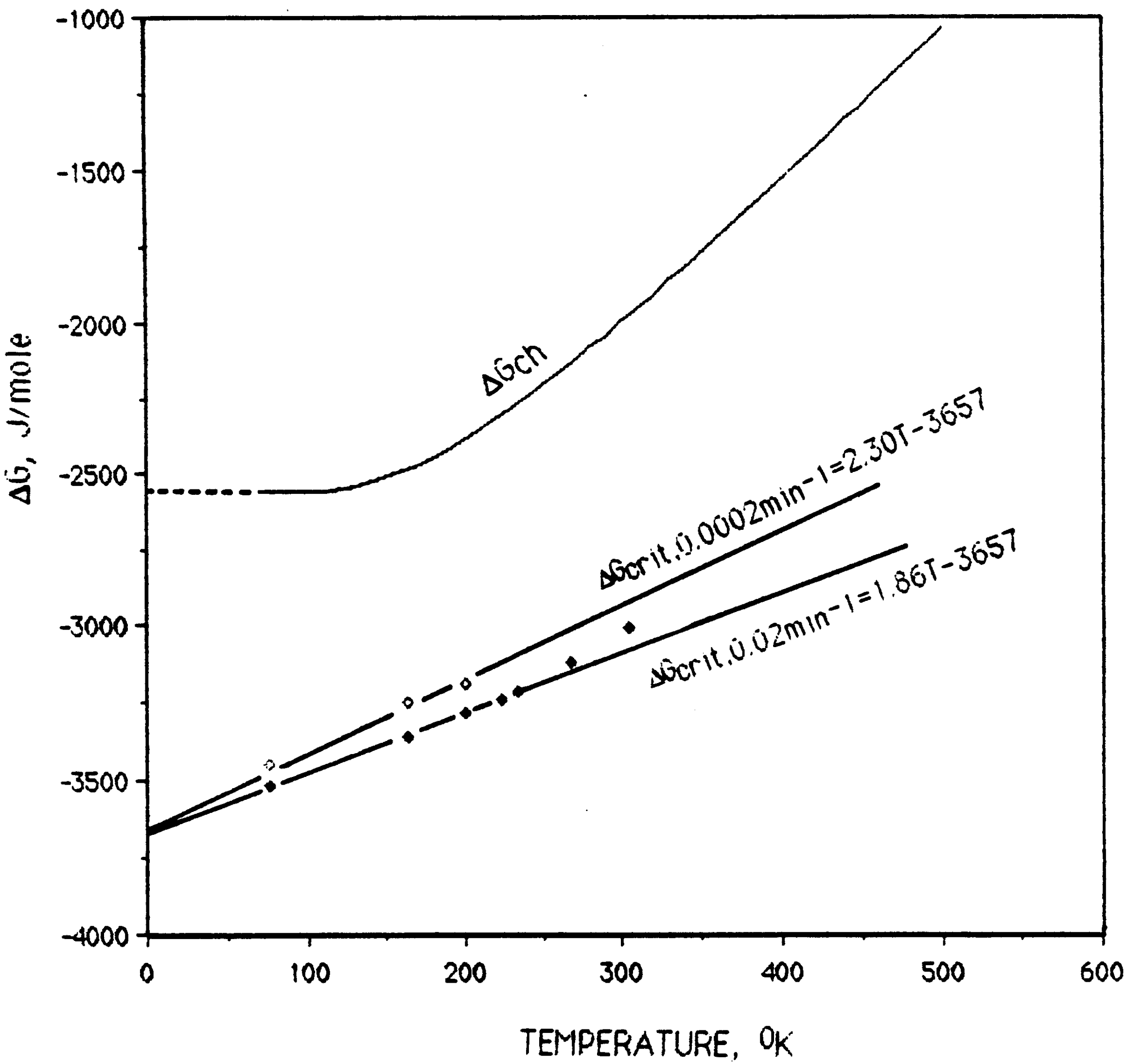

Fig.5-13. Temperature dependence of chemical free-energy change (ΔG_{ch}) and critical free-energy change (ΔG_{crit}) at strain rates of 0.02 and 0.0002 min^{-1} for the 0.5Mn-0 alloy.

with similar slope has also been observed for a warm-rolled high strength TRIP steel Fe9Cr8Ni4Mo2Si0.8Mn0.27C below $M_s^{\sigma}(UT)$ [26]. As described in Section 2-1-2, the fixed rate of transformation can be expressed as an exponential function of the total driving force, $A+B\,\Delta G_{crit}$, as :

$$\dot{f}_{\alpha'} = n_s V \nu \cdot \exp(-(A+B\Delta G_{crit})/RT) \qquad (5\text{-}1)$$

where n_s is the density of nucleation sites, V is the instantaneous mean martensitic plate volume, ν is the nucleation-attempt frequency, A and B are constants. The constant B corresponds to the "activation volume" for thermally activated motion of the nucleus interface. Rearranging Eq.5-1, the relation between ΔG_{crit} and temperature T is given by :

$$\Delta G_{crit} = -1/B \cdot (A+RT \cdot \ln(\dot{f}_{\alpha'}/n_s V \nu)) \qquad (5\text{-}2)$$

which does indicate a linear temperature dependence of the ΔG_{crit}. Using the two slopes of the ΔG_{crit} lines in Fig.5-13 and the ratio of strain rates, coefficient B is found to be 88 Ω, with Ω being the atomic volume, in good agreement with the value (90 Ω) obtained from isothermal nucleation experiments on Fe-Ni-Mn alloy [80]. From the ΔG_{crit} value at 0^0K and B, the coefficient A is calculated to be 3.22×10^5 J/mole, which is about 50 % greater than the A value from the nucleation experiments on annealed Fe-Ni-Mn alloy [80]. This is attributed to an increased friction stress inhibiting interfacial dislocation motion in the warm-rolled and aged substructure of high-strength 0.5Mn-0 alloy. Substituting the A and B parameters, typical values of $n_s = 10^6$ cm^{-3} and $V = 1.5 \times 10^{-9}$ cm^3, and other numerical data into Eq.5-1, the nucleation-attempt frequency ν is found to be 2.1×10^7 sec^{-1}.

This is the same order as an experimental ν measured by applying high magnetic fields to vary the driving force [81]. Comparing the atomic vibration frequency $10^{13}sec^{-1}$ used in early analysis of experimental operational nucleation kinetics, the observed very low nucleation-attempt frequency can be rationalized by the large size difference (few microns) between the pre-existing embryo and the operational nucleus in ferrous alloys [80].

Using the ΔG_{mech} ($=\Delta G_{crit}-\Delta G_{ch}$) in Fig.5-13 and the $\partial\Delta G/\partial\sigma$ values (-0.56 J/mole-Mpa for uniaxial compression, -0.86 J/mole-Mpa for uniaxial tension, and -1.42 J/mole-Mpa for the crack tip) derived by Olson and Cohen [26], the temperature dependence of stress for the stress-assisted transformation under various stress-states can be calculated for the 0.5Mn-0 alloy. Fig. 5-14 shows the measured yield stress and the calculated transformation stress in uniaxial tension at strain rates of 0.02 and 0.0002 min^{-1}. The theoretical stress curve passes through a minimum point and presents a smooth "U" shape as expected due to the nonlinearity of the ΔG_{ch} vs. temperature curve. The M_s^σ(UT), which can be estimated from the intersection of the theoretical stress and the yield stress of parent phase, increases with the strain rate decreasing and qualitatively agrees with some experimental observations [91]. The calculated transformation equivalent stresses in compression, tension, and crack tip are plotted vs. temperature in Fig.5-15 along with the measured yield stresses to predict M_s^σ corresponding to each stress-state. There is considerable discrepancy between the predicted and the measured M_s^σ, particularly in the cases of compression and crack tip, as also listed in Table 5-2. This might arise from using a constant mechanical driving force $\partial\Delta G/\partial\sigma$ for each loading condition or by considering all nucleation sites being of the optimum orientation. Using a recent statistical analysis [82] in which the influence of stress on the effective potency distribution was calculated on the assumption of a random distribution of pre-existing nucleation-site orientation may possibly reduce the above discrepancy, though that model was developed for low strength annealed austenite.

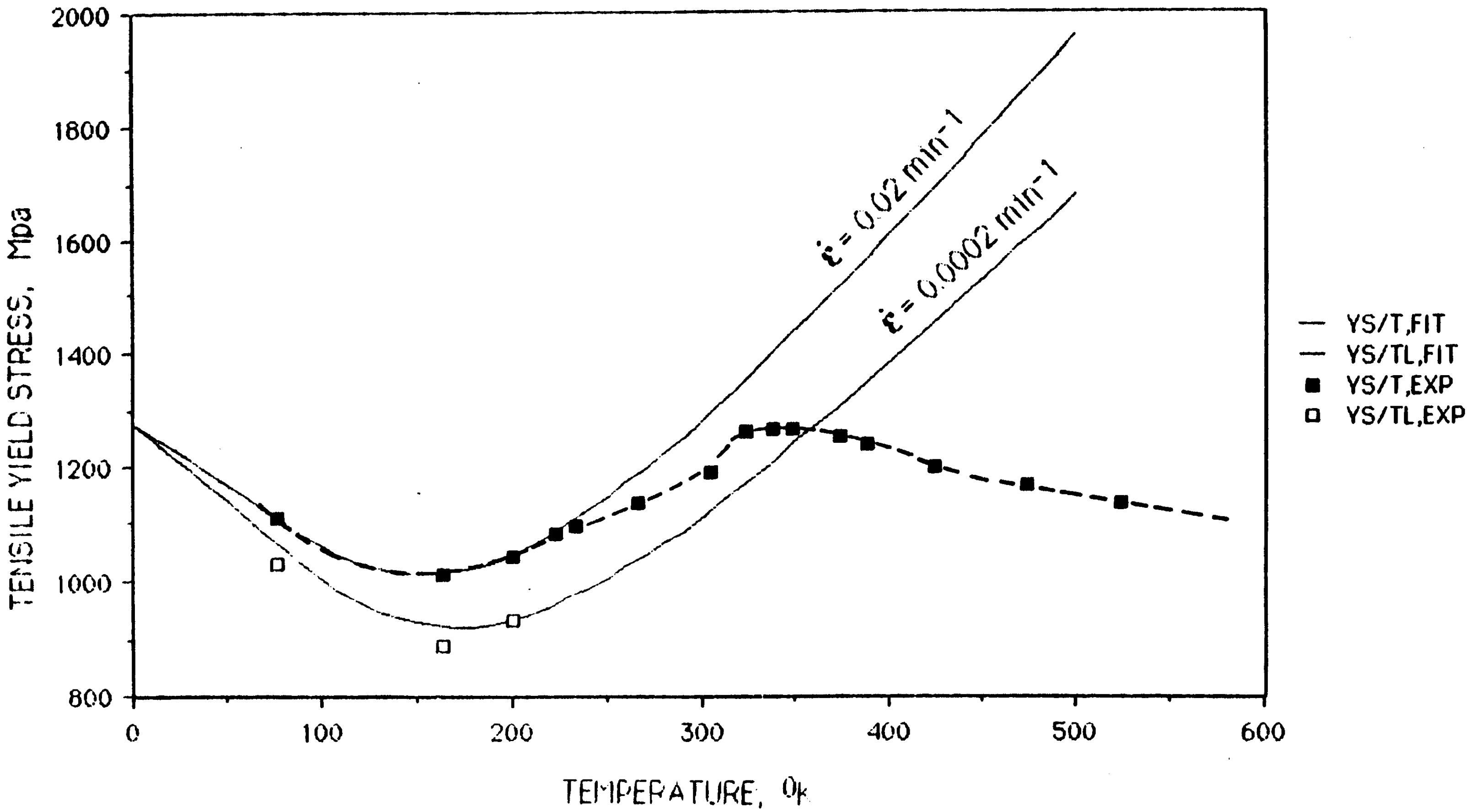

Fig.5-14. Observed temperature dependence of tensile yield stress and calculated stress for stress-assisted transformation for 0.5Mn-0 alloy at two strain rates.

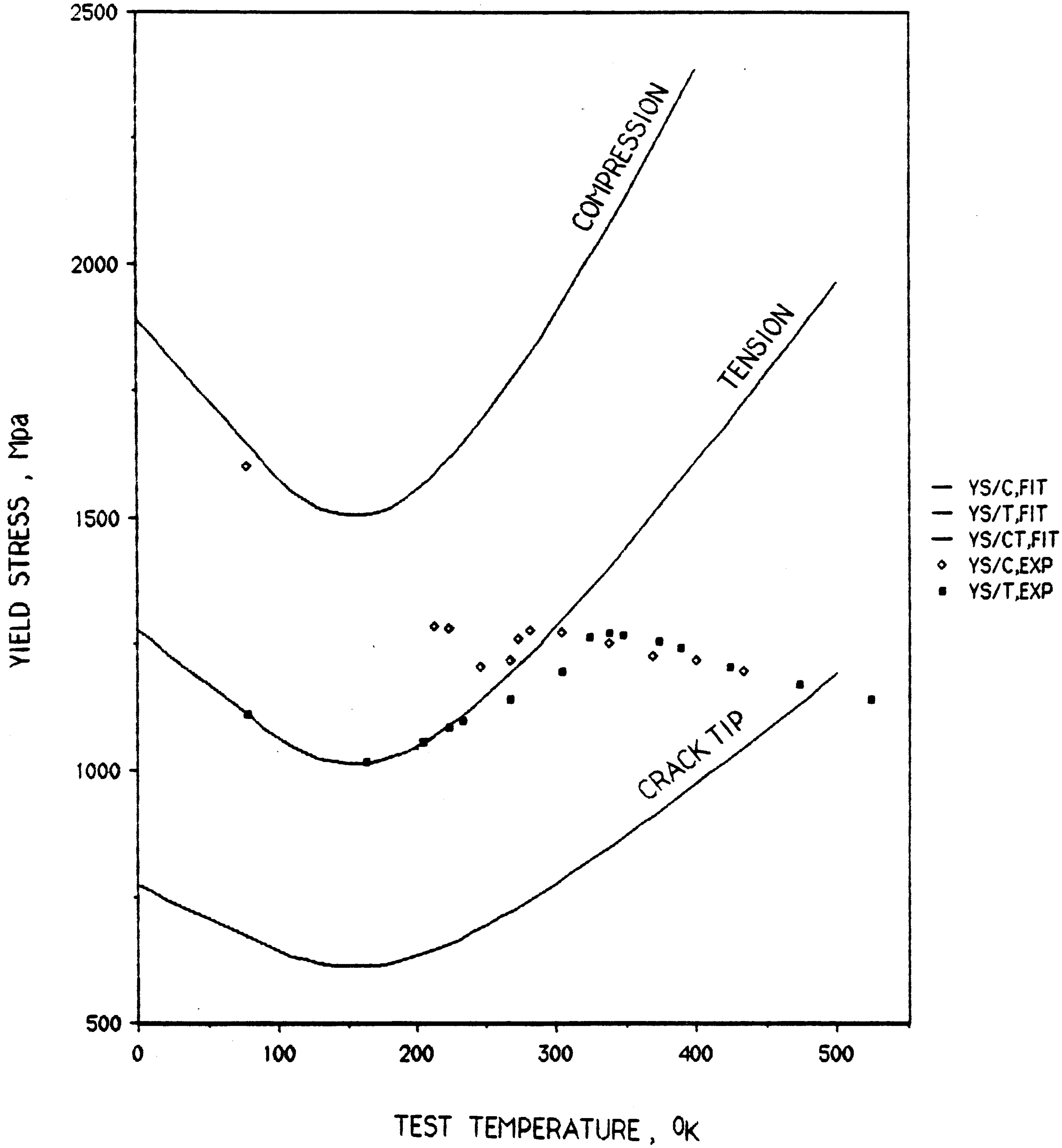

Fig. 5-15 Calculated transformation stress and measured yield stress for 0.5Mn-0 alloy under different stress-states.

5-2-2 Transformation Kinetics

In the last section, we estimated the transformation temperature M_s^{σ} and found that it is a function of chemical composition, aging treatment, strain rate, and stress-state. However, the M_s^{σ} temperature only reflects the austenite stability in a qualitative sense and can not be used to evaluate the stress-strain relationships governing the macroscopic mechanical properties, when the martensitic transformation is involved during the deformation process. In order to explore the effect of transformation on properties, the transformation rate with respect to plastic strain, stress-state, and temperature must be known. In this section, the transformation kinetics of the least stable alloy 0.5Mn-0 was measured in both uniaxial tension and compression at temperatures ranging from -196 to 126°C. Though the results are relatively limited in quantity, they do show how stress-state, temperature, plastic strain, and transformation mode influence the kinetics.

Table 5-3 summarizes the results of kinetics measurements as well as the values of parameters used to fit the strain-induced transformation curves. At temperatures above 65°C, it was not possible to measure the transformation curves in uniaxial tension beyond a true plastic strain of 0.1 because of the onset of necking. The martensite volume fraction is plotted versus the true plastic strain in compression and in tension as shown in Figs.5-16 and 5-17, respectively. In both figures, the data are depicted in two groups according to the transformation modes. The dash-lines represent the kinetics when the stress-assisted mode is predominant, while the solid-lines correspond to the strain-induced transformation kinetics. The

Table 5-3. Transformation Kinetics Data and Fitting Parameters

Compression		Tension	
ε_p	$f_{\alpha'}$	ε_p	$f_{\alpha'}$
-50°C		-196°C	
0.026	0.091	0.057	0.625
0.105	0.514	-110°C	
0.216	0.819	0.051	0.625
-50°C,S		-6°C	
0.056	0.370	0.049	0.620
-27°C		0.082	0.890
0.067	0.333	0.190	0.975
-27°C,S		31°C	
0.018	0.127	0.074	0.485
0.066	0.368	0.130	0.770
-6°C		0.250	0.958
0.074	0.323	65°C, α=10.1, β=2.36	
0.175	0.652	0.064	0.143
0.276	0.800	0.155	0.628
31°C, α=11.3, β=1.54		0.270	0.826
0.086	0.205	0.360	0.890
0.185	0.590	100°C, α=8.20, β=1.01	
0.234	0.667	0.089	0.072
0.331	0.761	115°C, α=6.90, β=0.65	
0.402	0.772	0.090	0.029
65°C, α=10.3, β=0.66		------	
0.085	0.075	------	
0.181	0.280	------	
0.332	0.425	------	
0.404	0.464	------	
96°C, α=8.50, β=0.23		------	
0.143	0.055	------	
0.207	0.092	------	
0.339	0.178	------	
126°C, α=5.70, β=0.14		------	
0.214	0.037	------	
0.360	0.079	------	

S---represents slower strain rate

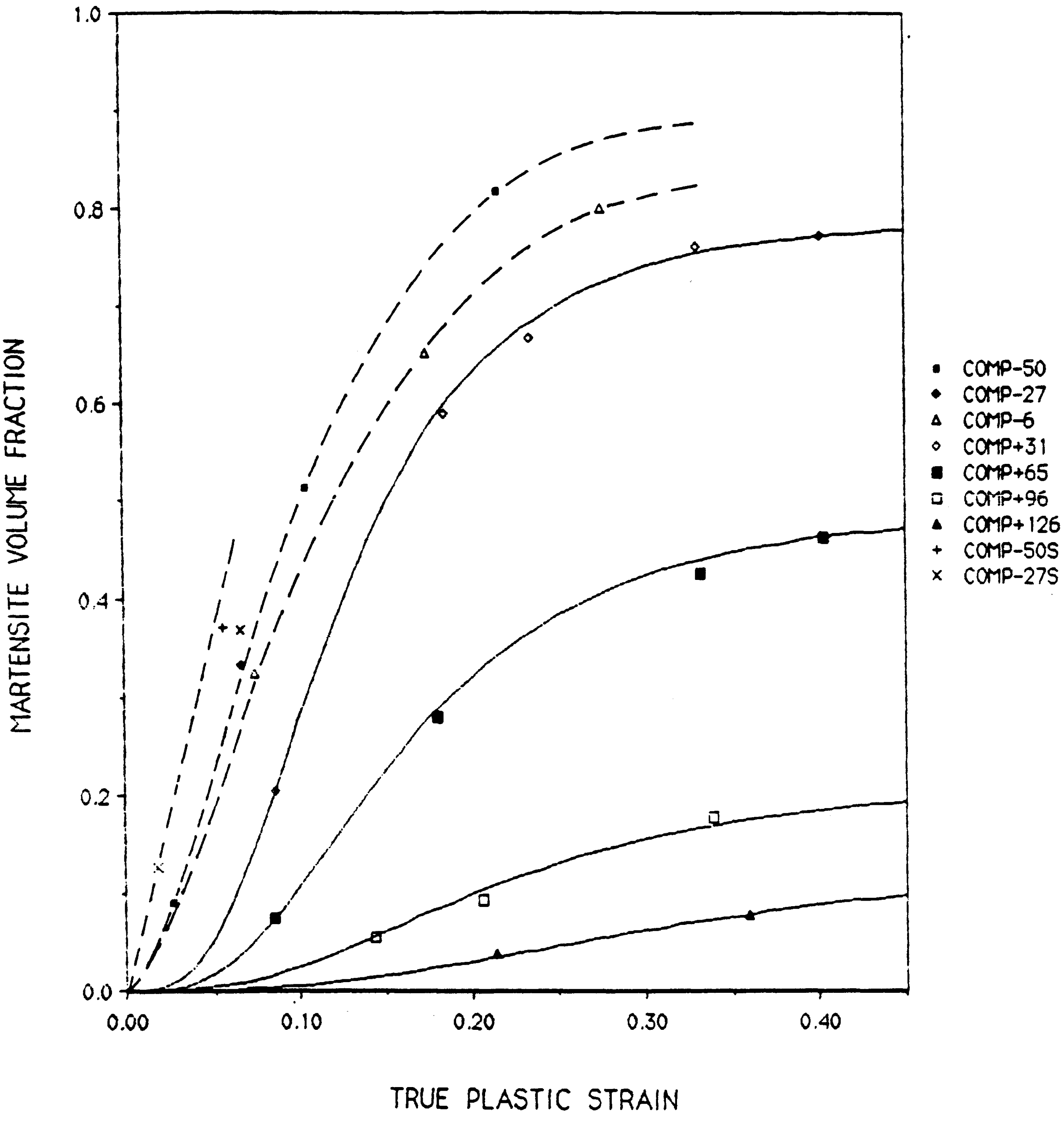

Fig.5-16 Transformation curves for the overaged 0.5Mn alloy in uniaxial compression. The dash-lines correspond to the kinetics in stress-assisted mode, while the solid-lines represent the strain-induced transformation kinetics fitted to the Olson-Cohen model [22].

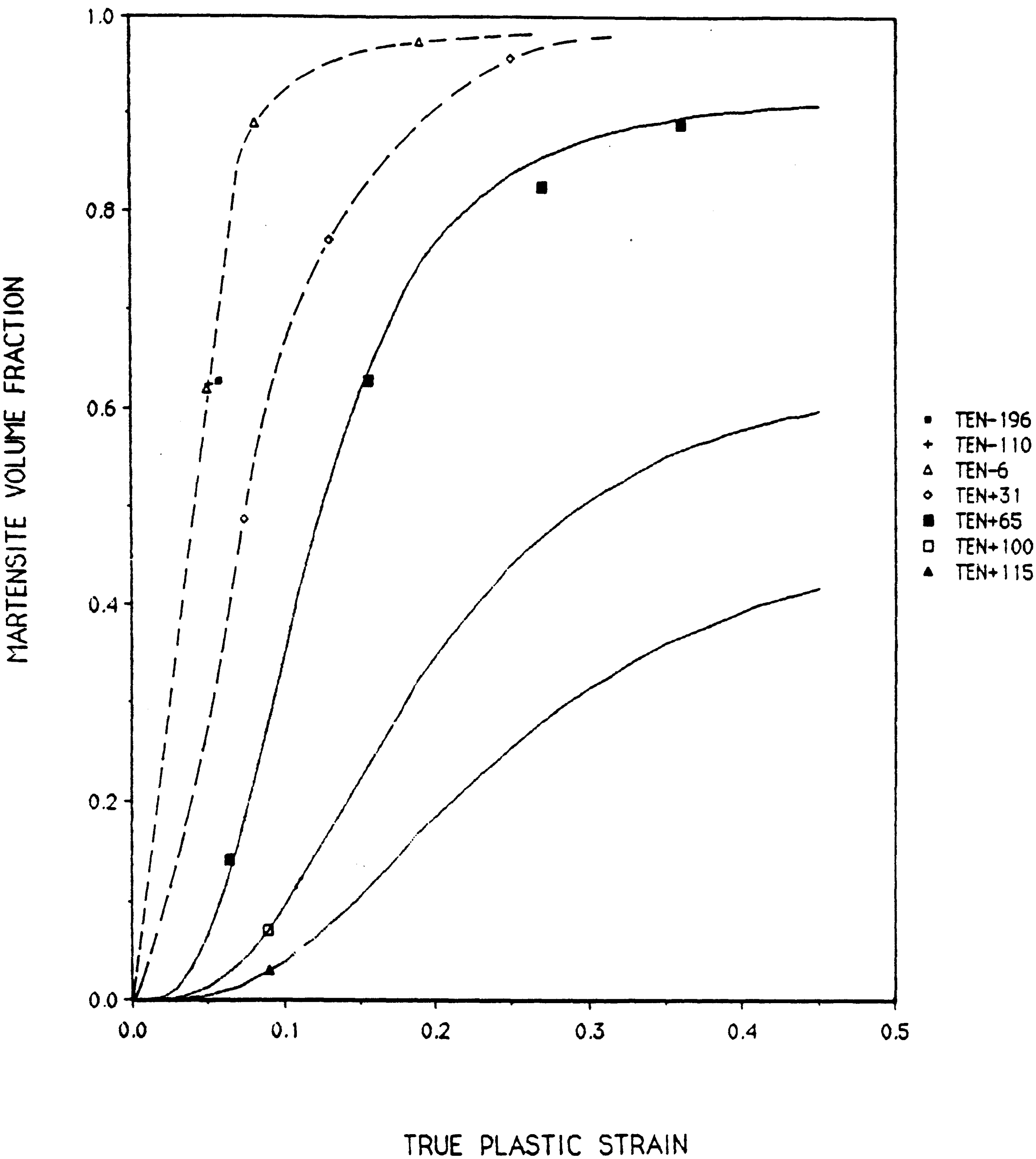

Fig.5-17 Transformation curves for the overaged 0.5Mn alloy in uniaxial tension. The dash-lines correspond to the kinetics in stress-assisted regime, while the solid-lines represent the strain-induced transformation kinetics fitted to the Olson-Cohen model [22].

test type, temperature, and strain rate are designated in the legend. For example, COMP-27S means the compression test was run at -27°C in a slower strain rate 0.0002min^{-1} rather than 0.02min^{-1} used for most cases.

Stress-assisted transformation In uniaxial tension, the transformation curves in Fig.5-17 exhibit an initially linear behavior at temperatures far below M_s^σ(UT) (53°C) and the slope is independent of the test temperature comparing the data obtained at -196,-110, and -6°C. Such linear $f_{\alpha'}$-ε_p curves are expected when deformation is entirely controlled by the transformation. At those temperatures, the transformation kinetics can be expressed as $f_{\alpha'} = k\varepsilon_p$, where the constant k equals 12.5 (or 1/k = 0.08) for the 0.5Mn-0 alloy. 1/k can be interpretated as the plastic strain caused by 100 pct martensitic transformation. However, the $f_{\alpha'}$-ε_p curves in compression are no longer linear at temperatures below M_s^σ(UT) even at a plastic strain as low as 0.02. Examining the metallography shown in Fig. 5-18, the nonlinear behavior was found to arise from the earlier perturbation of strain-induced martensite, but not from the stress biasing of the martensitic plate variants [5]. This is consistent with the much smaller yield stress drop under compression than that under tension in Fig.5-11 at temperatures below the corresponding M_s^σ.

Strain-induced transformation At temperatures above M_s^σ, all transformation curves in both tension and compression for 0.5Mn-0 have a sigmoidal shape. The typical microstructure subjected to tensile plastic strain at 65°C in Fig.5-19 shows that fine lath martensite formed predominantly at the intersection of shear bands in the austenite. It seems reasonable to fit the experimental results using the Olson-Cohen model for

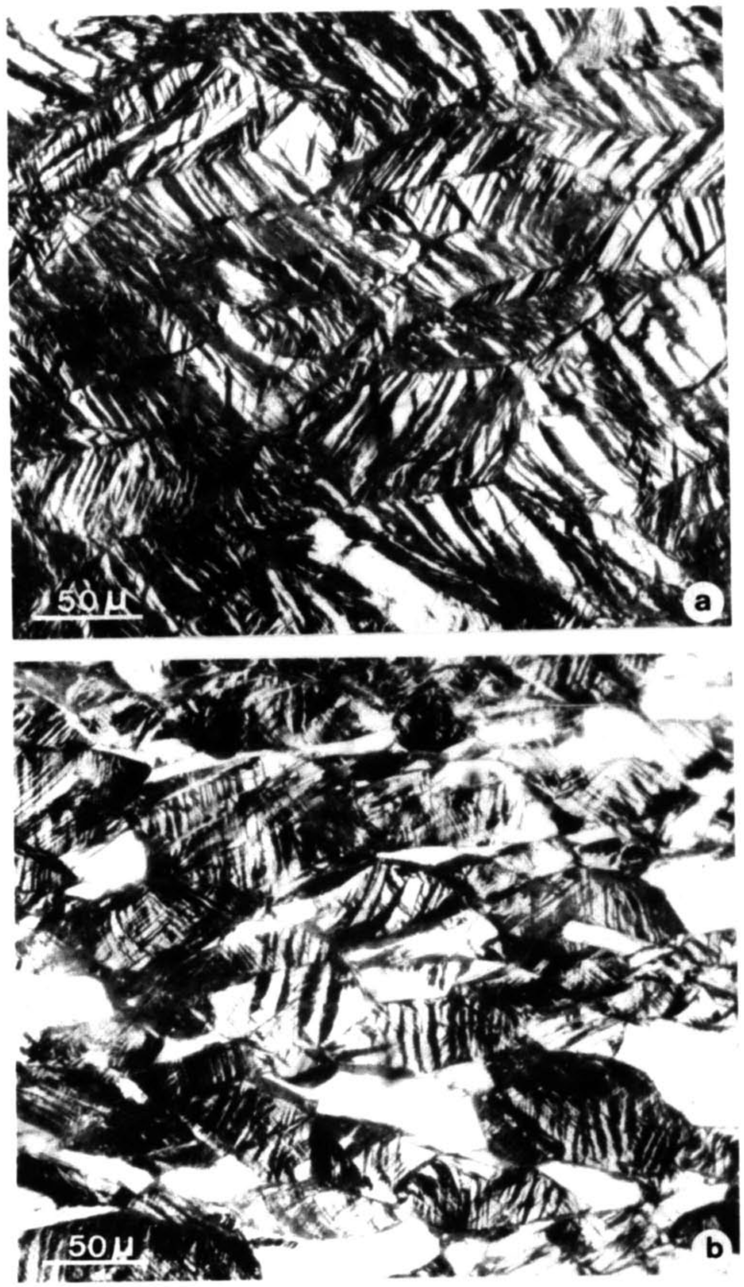

Fig 5-18 Morphology of martensite transformed below M_s^{σ} temperature, (a). uniaxial tension with $\varepsilon_p=0.051$ at -110ºC. Only plate martensite is found. (b) uniaxial compression with $\varepsilon_p=0.067$ at -27ºC. It shows a mixed microstructure of plate and lath martensite.

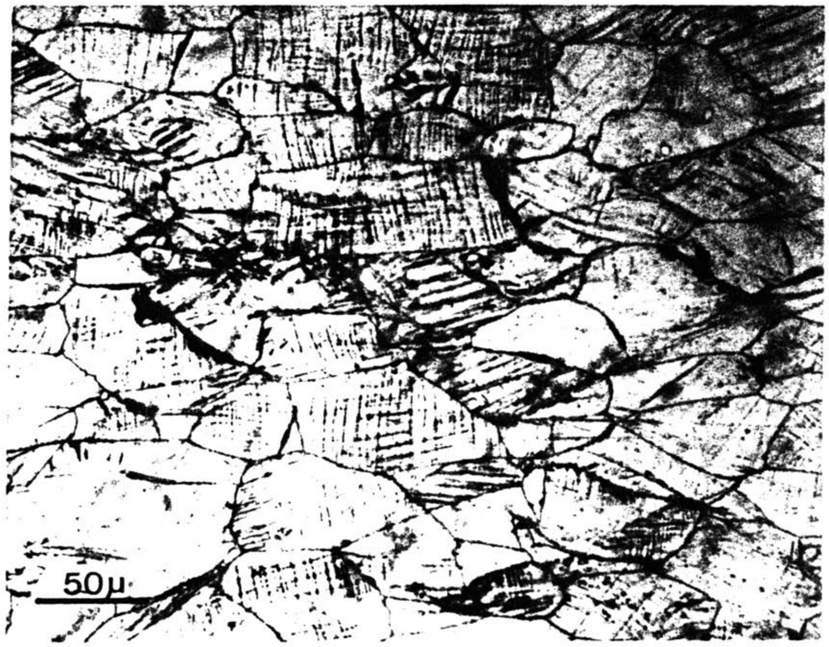

Fig.5-19 Typical morphology of the strain-induced martensite produced at 65ºC in tension. Fine martensitic laths are formed at shear-band intersections.

the strain-induced transformation kinetics [29], which assumes microscopic shear band intersections to be the dominant nuceation sites. The total volume fraction of martensite is related to the true plastic strain by rewriting Eq.2-7 :

$$f_{\alpha'} = 1 - \exp\{-\beta\,[1-\exp(-\alpha\varepsilon_p)\,]^n\} \qquad (5\text{-}3)$$

where n is a fixed exponent larger than 2, the α parameter is temperature dependent through the temperature dependence of stacking fault energy, the β parameter is temperature and stress-state dependent. Eq.5-3 gives sigmoidal transformation curves with the saturation level being determined by the parameter β, and the rate of approach to saturation being controlled by both parameters α and β. Eq.5-3 is first fitted to the measured kinetics data in compression and those at 65ºC in tension. An exponent of n=4.0 is found to give the best overall agreement between the experimental data and Eq.5-3, as shown by the solid lines in Fig.5-16 and 5-17. The fitted α parameters are plotted vs. temperatures in Fig.5-20 which verifies that the α parameter is sensitive to temperature but independent of stress-state from a comparison of α parameters at 65ºC in tension and in compression. Therefore, Fig.5-20 allows an interpolation to estimate the α parameters for the kinetics curves in tension at 100 and 115ºC in order to calculate the corresponding β parameters fitted to n=4.0 and the single measured martensite volume fraction. The β parameter in tension is much larger than that in compression at any given temperature, as shown in Fig.5-21, to account for the different thermodynamic assist of applied stress between the two stress-states. However, both curves in Fig.5-21 have a similar temperature dependence. Considering that the change of austenite stability in tension and in compression can be reflected by the shift of transformation temperature M_S^{σ}, the β parameters are replotted vs. a temperature interval ($T-M_S^{\sigma}$) in Fig.5-22. It is found that all fitted β values comprise a single curve in the shape of an exponential function, which is consistent with the gaussian distribution of shear-band intersection potencies with respect to temperature as proposed in Olson-Cohen's work [29]. An empirical equation was derived to express the β parameter of 0.5Mn-0 alloy in terms of the temperature interval (°C) as :

$$\beta = 3.18 \cdot \exp\left[-(T-M_S^{\sigma}(\sigma_h/\sigma))/40.3\right] \qquad (5\text{-}4)$$

where the transformation temperature $M_S^{\sigma}(\sigma_h/\sigma)$ is a function of stress-state, σ_h/σ. Assuming that a linear relation between $M_S^{\sigma}(\sigma_h/\sigma)$ and σ_h/σ is valid within the stress-state range from uniaxial compression to tensile neck as shown in Fig.5-12, $M_S^{\sigma}(\sigma_h/\sigma)$ equals $76.5 \cdot \sigma_h/\sigma + 27.5$ in units of centigrade degrees and Eq.5-4 can be written as :

$$\beta = 3.18 \cdot \exp\{-[T-(76.5 \cdot \sigma_h/\sigma + 27.5)]/40.3\} \qquad (5\text{-}5)$$

Eq.5-5 will be used to estimate the effect of stress-state change on the transformation kinetics in the tensile neck and consequently on the strain-hardening rate which is related to the observed fracture strain when fracture is controlled by shear-instability [83].

The above analysis of kinetic data is empirical. The transformation curves in tension and compression were fitted well by carefully adjusting n, α, and β parameters. Within a limited range of stress-states, a simple

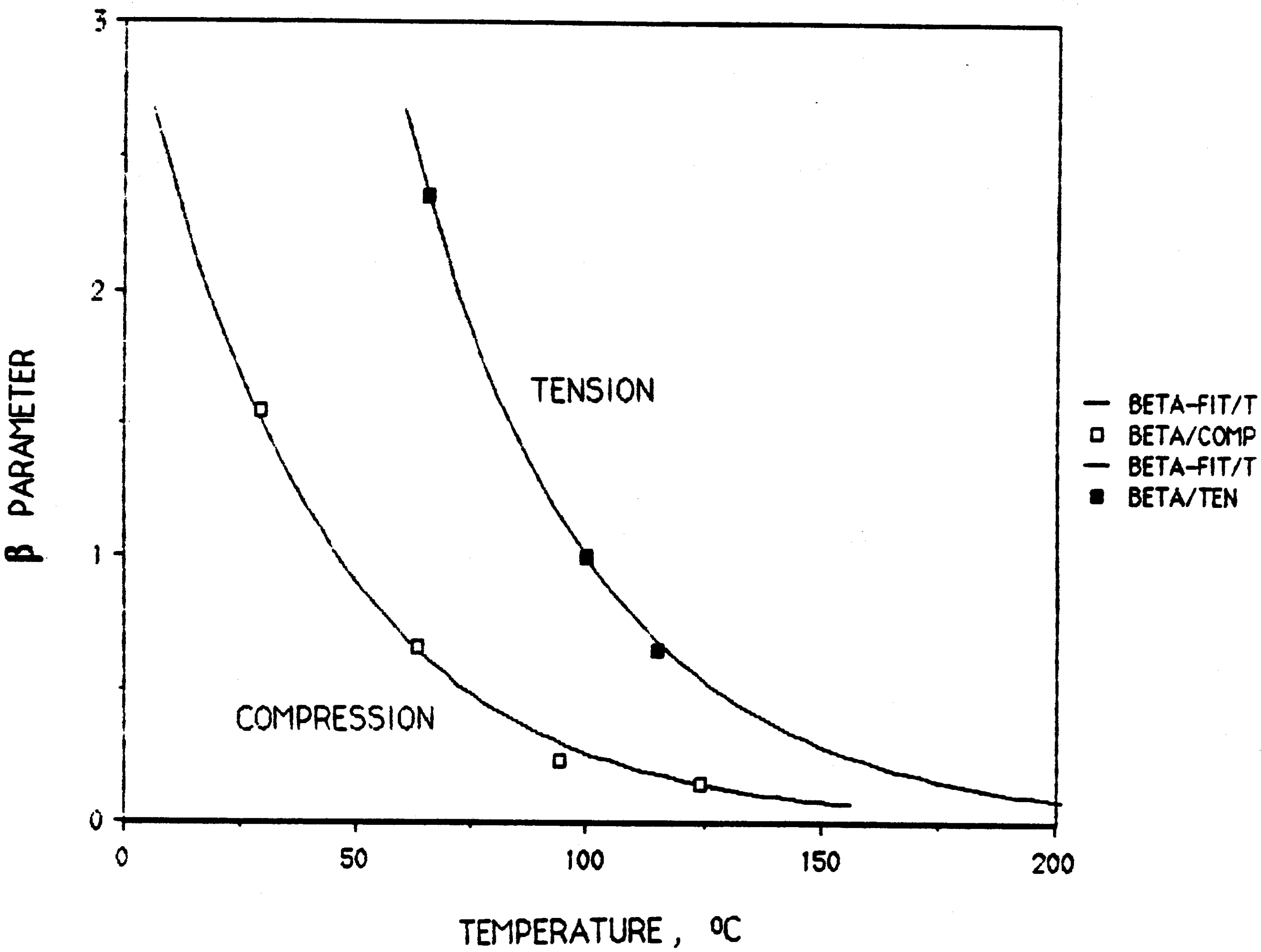

Fig.5-21 Temperature dependence of β parameter from Eq.5-3 in tension and compression.

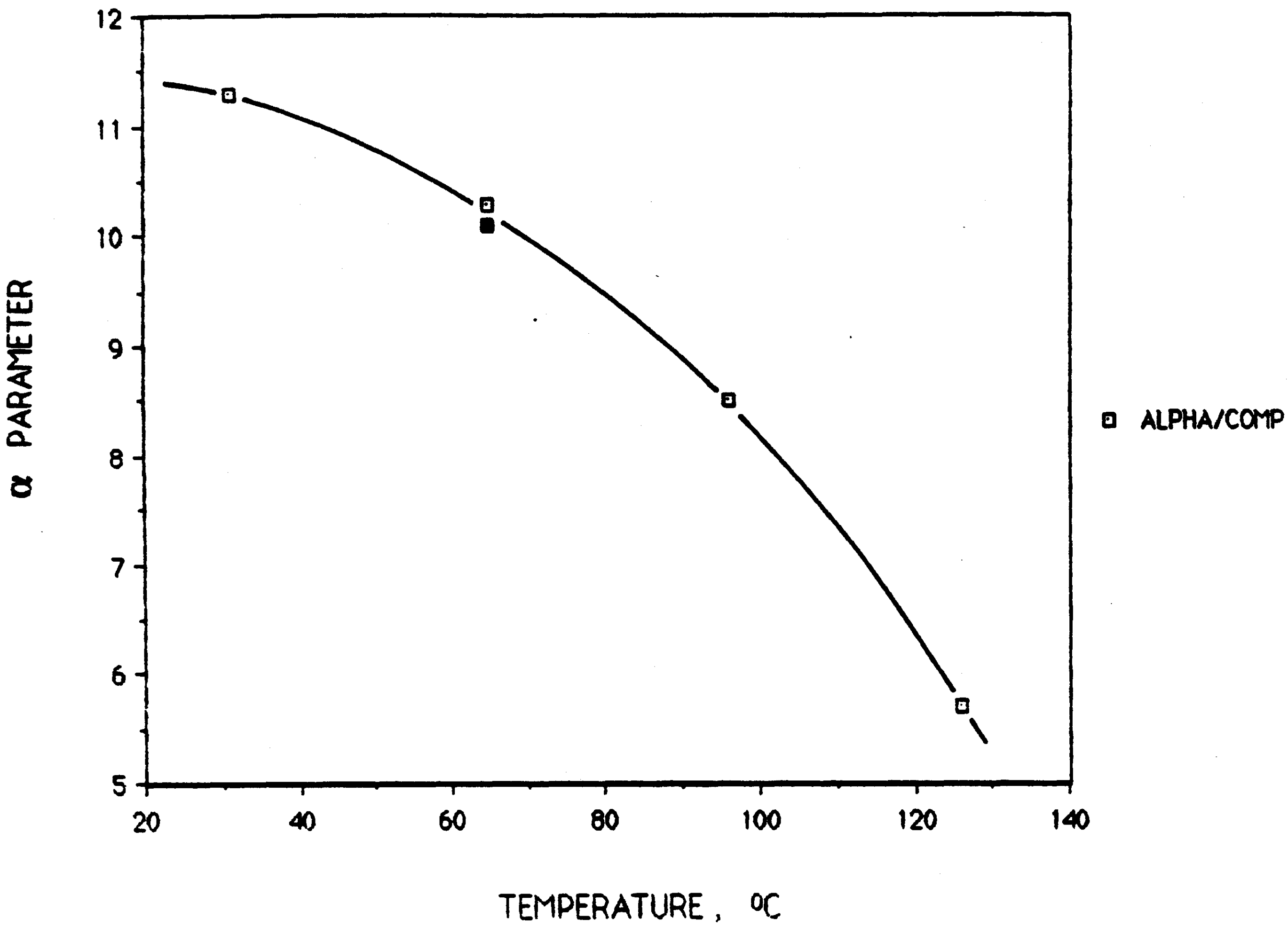

Fig.5-20 Temperature dependence of the α parameter from Eq.5-3. Open squares represent analysis for the compressive data. Solid square indicates analysis for the tensile data.

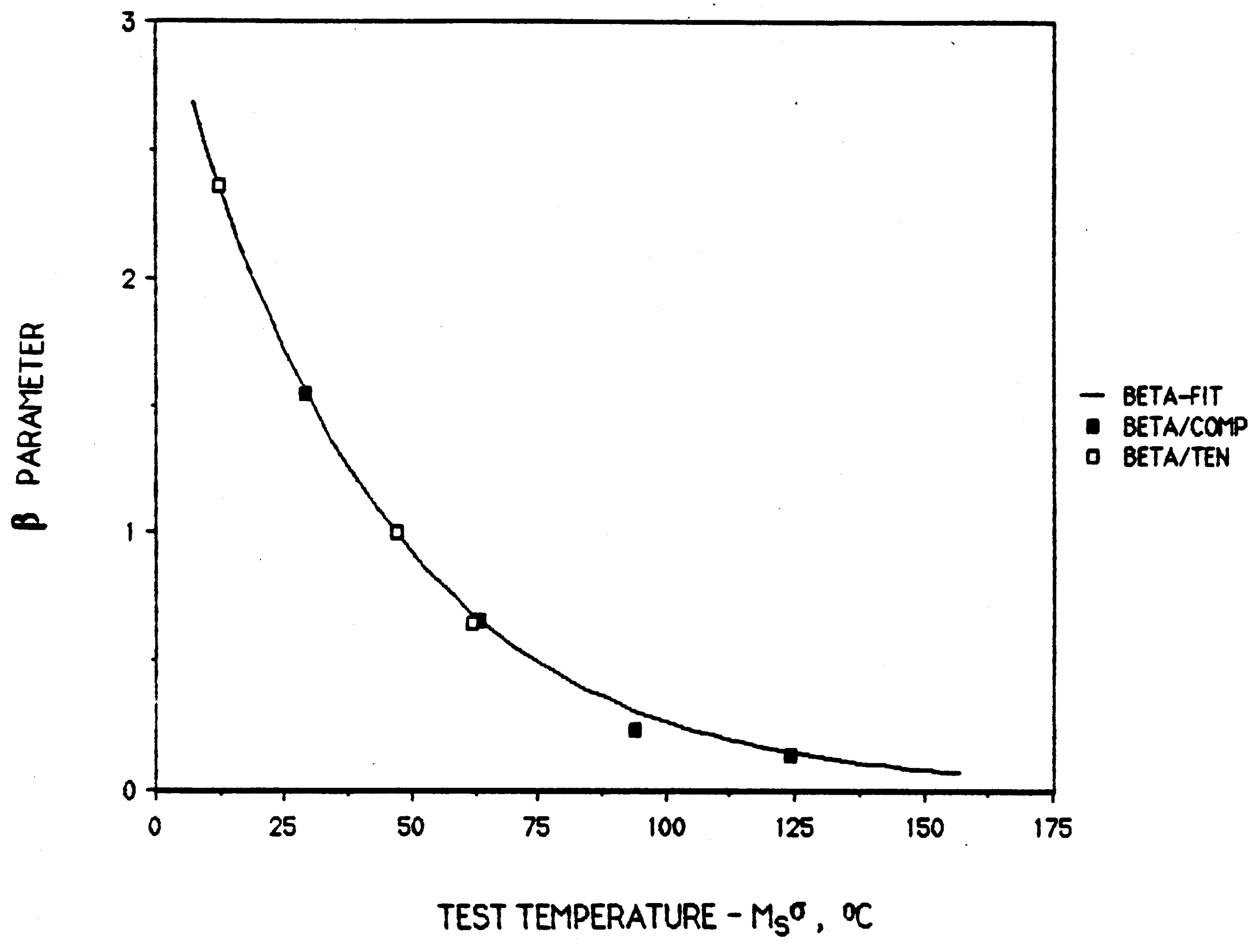

Fig.5-22 All values of β parameter are plotted vs. temperature interval, T-M_S^σ, and form a single exponential curve. Open and solid squares correspond to tension and compression data, respectively.

exponential equation correlates the β parameter to the M_s^{σ} taking care of the effect of triaxiality on kinetics. However, the presently used kinetic equation is not a convenient form to be applied in the finite element calculation of the martensite volume fraction around a crack-tip where both triaxiality and strain are functions of position. Efforts to develop a general kinetic model for the strain-induced transformation expressed in incremental form is underway [84]. In the new model, the martensite embryo is assumed to exist at all kinds of crystal defects and then the probability (p) of forming a nucleus from an embryo is evaluated, as an appropriate function of the total driving force including both the chemical and mechanical parts. Considering the dilatation and the shear strain associated with transformation, the mechanical driving force is estimated from a statistical model proposed by Tsuzaki et al. [82] and consists of two energy terms involving hydrostatic pressure (σ_h) and deviatoric stress ($\bar{\sigma}$), respectively. The final relationship between the martensite volume fraction and the imposed slip plastic strain ($\varepsilon_{sl}{}^p$) can be written in incremental form :

$$-\ln[(1-f_{\alpha'})/1-f_{\alpha',o})] = V_{\alpha'}\cdot\{p(T,\sigma_{h,o},\bar{\sigma}_o)\cdot[N_v{}^D(\varepsilon_{sl}{}^p) - N_v{}^D(\varepsilon_{sl,o}{}^p)] + N_v{}^D(\varepsilon_{sl,o}{}^p)\cdot[p(T,\sigma_h,\bar{\sigma}) - p(T,\sigma_{h,o},\bar{\sigma}_o)]\} \quad 5\text{-}6$$

where $V_{\alpha'}$ = average volume of a martensitic plate

$N_v{}^D(\varepsilon_{sl}{}^p)$ = defect density during deformation-induced transformation

$= K\cdot[1-\exp(-\alpha\varepsilon_{sl}{}^p)]^n$; K, n, and α are parameters fitted to the experimental results of kinetics.

$p(T,\sigma_h,\bar{\sigma})$ = probability of forming a nucleus from a crystal defect at σ_h

and $\bar{\sigma}$.

The subsript o indicates the previous values of related terms. This model is being refined and fitted to the experimental data. As the ultimate goal of transformation plasticity research, the new kinetic model along with the stress-strain relations of parent and product phases will be employed to quantify the transformation toughening effect around a crack-tip through a continuum mechanics approach [78].

5-3. Mechanical Behavior and Deformation-Induced Martensitic Transformation

5-3-1. Tensile Properties

For a given metastable austenitic steel, the stability of the parent phase as well as the flow behavior of both austenite and martensite are influenced by the temperature of testing, and so are the resultant tensile properties. Table 5-4 lists the values of 0.2% yield stress (σ_y), fracture stress (σ_f), true plastic uniform strain (ε_{pu}), and true plastic fracture strain (ε_{pf}) obtained for the three alloys studied. The variations of the 0.2% yield stress with test temperature for the three steels has been elucidated in Section 5-2-1. The temperature dependence of ε_{pu} and ε_{pf} for the overaged and the underaged alloys along with the relevant transformation temperatures M_s^σ and M_d are shown in Fig.5-23 and Fig.5-24, respectively, and will be discussed separately. For the sake of clarity, the indicated transformation temperatures represent the mean values listed in Table 5-2.

a. Overaged Alloy

With decreasing test temperature from 200°C, the uniform plastic strain ε_{pu} initially maintains at a nearly constant value, followed by a sharp, significant increase at 65°C, and then progressively drops, as shown in Fig.5-23. The uniform ductility reaches a maximum at 65°C slightly above M_s^σ(UT) (= 53°C), reflecting an optimum transformation rate to resist the onset of necking. Above 65°C, the work-hardening associated with the sluggish transformation is insufficient to supress the onset of necking and the enhancement of uniform ductility is almost negligible. On the other hand, the early completion of transformation at temperatures below 65°C

Table 5-4. Tensile Properties

0.5Mn-0 Alloy				
T(ºC)	σ_y(Mpa)	ε_{pu}	ε_{pf}	σ_f(Mpa)
-50	1085	0.170	0.22	2032
-40	1097	0.184	0.34	2153
-6	1140	0.190	0.36	2192
31	1193	0.250	0.42	2072
65	1268	0.360	0.53	2025
75	1265	0.075	0.56	2044
100	1252	0.090	0.67	2056
115	1240	0.089	0.85	2030
150	1200	0.080	0.77	2013
200	1168	0.060	0.60	1761
250	1140	0.060	0.57	1627
0.5Mn-U Alloy				
T(ºC)	σ_y(Mpa)	ε_{pu}	ε_{pf}	σ_f(Mpa)
-6	1340	.092	0.092	1700
31	1290	0.100	0.24	1721
65	1255	0.090	0.26	1712
100	1223	0.063	0.55	1871
135	1239	0.059	0.63	1980
185	1197	0.063	0.58	1775
3.5Mn-U Alloy				
T(ºC)	σ_y(Mpa)	ε_{pu}	ε_{pf}	σ_f(Mpa)
-80	1345	0.38	0.38	1893
-50	1326	0.085	0.25	2062
-20	1302	0.070	0.56	2080
0	1275	0.073	0.85	2235
40	1255	0.10	0.82	19955
100	1224	0.092	0.74	1936
150	1185	0.070	0.78	1869
200	1145	0.070	0.70	1751
250	1130	0.070	0.66	1750

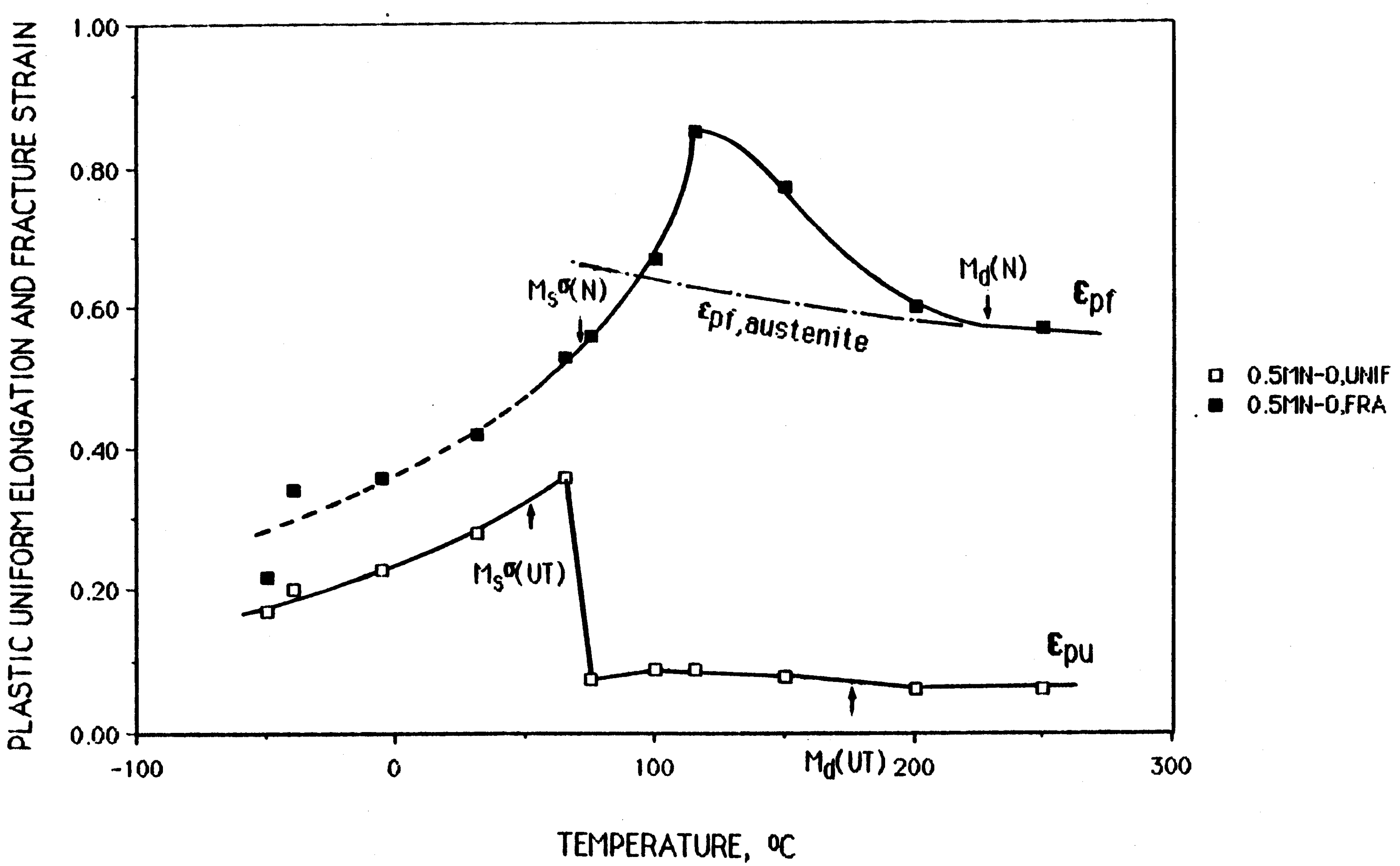

Fig. 5-23 Temperature dependence of fracture plastic strain (ε_{pf}) and uniform plastic strain (ε_{pu}) for the overaged 0.5Mn-0 alloy. Arrows indicate the mean values of the relevant transformation temperatures. The estimated fracture strain of austenite is also shown.

according to the kinetics measurements in Table 5-3 leads to lower necking strains.

With decrease of test temperature from 250°C, the fracture strain of the 0.5Mn-O alloy first increases to reach a maximum value, and then rapidly decreases, as shown in Fig.5-23. Similarly, the variation of ε_{pf} with temperature is related to the strain-hardening rate and dilatation provided by the deformation-induced martensitic transformation to retard the fracture process. There is also an optimum transformation rate in the range of high strain corresponding to the maximum ε_{pf} at 115°C, which is about 45°C above the estimated $M_s^{\sigma}(N)$ rather than at $M_s^{\sigma}(N)$ as previously observed in some γ'-strengthened austenitic steels [1]. At temperatures below 31°C, the brittle fracture modes including cleavage, and intergranular fracture control the failure of the 0.5Mn-O alloy where the ε_{pf} vs. temperature curve is represented by a dash line. The fracture strain of the austenitic phase is also plotted vs. temperature in Fig.5-23 as indicated by the fracture-strain values of the most stable 3.5Mn-U alloy at temperatures above M_d. The best enhancement of ε_{pf} for the 0.5Mn-O alloy is not remarkable ($\cong$ 0.25), possibly owing to the small hardness difference between α' and γ phases, listed in Table 3-3. A quantitative analysis of the influence of strain-induced martensitic transformation on the uniform strain and the fracture strain of the 0.5Mn-O alloy will be presented in Section 5-3-3 by combining the transformation kinetics to the flow relations of both the parent and the product phases.

b. Underaged Alloys

The underaged alloys 0.5Mn-U and 3.5Mn-U are expected to exhibit better ductility enhancement than the overaged 0.5Mn-O alloy because the martensitic phase of these two alloys is much stronger and consequently can provide a more significant work-hardening effect. However, the premature intergranular fracture prevented the underaged alloys from taking full advantage of transformation plasticity to enhance the ductility.

Considering that the brittle fracture even occurred above the M_s^σ temperatures of both underaged alloys in Fig.5-24, the transition of fracture mode can not be entirely caused by the formation of plate martensite, which is thought to be more brittle than the fine lath martensite and responsible for the brittleness of TRIP steels below M_s^σ [1]. Fine grain size and consequent fine martensitic plates in the studied RSP alloys should be beneficial in reducing the tendency of brittleness below M_s^σ. In Table 5-5, the temperatures corresponding to the maximum ε_{pu} and ε_{pf} of the 3.5Mn-U and 0.5Mn-U alloys are predicted using both the relevant transformation temperatures and the temperatures at which the maximum values of ε_{pu} and ε_{pf} of the 0.5Mn-O alloy are found. Similar values of (M_d- M_s^σ) for the stress-states of both uniaxial tension and tensile-neck in all three alloys suggest that they have comparable values of stacking-fault energy and entropy change $\Delta S^{\gamma-\alpha}$. It implies that these three austenitic steels possess a similar stability at a given normalized temperature (T- M_s^σ) under the same stress-state. Therefore, the peak values of ε_{pu} and ε_{pf} corresponding to a common optimum transformation rate should occur at about the same (T- M_s^σ). Table 5-5 shows that the predicted values of

Table 5-5. Predicted Temperatures Corresponding to the Peak ε_{pu} and ε_{pf} for the Underaged Alloys.

Alloy	$M_s^{\sigma}(N)$	$M_d(N)$	$M_s^{\sigma}(N)-M_d(N)$	$T_{intergranular}$	Tpeak ε_{pf}
0.5Mn-O	73	225	152	< 31	115
0.5Mn-U	-5	160	165	<135	40
3.5Mn-U	-82	70	152	< 0	-39
Alloy	**$M_s^{\sigma}(UT)$**	**$M_d(UT)$**	**$M_s^{\sigma}(UT)-M_d(UT)$**		**Tpeak ε_{pu}**
0.5Mn-O	53	175	122		65
0.5Mn-U	-24	100	124		-12
3.5Mn-U	-105	10	115		-93

* All temperatures are represented in centigrade scale.

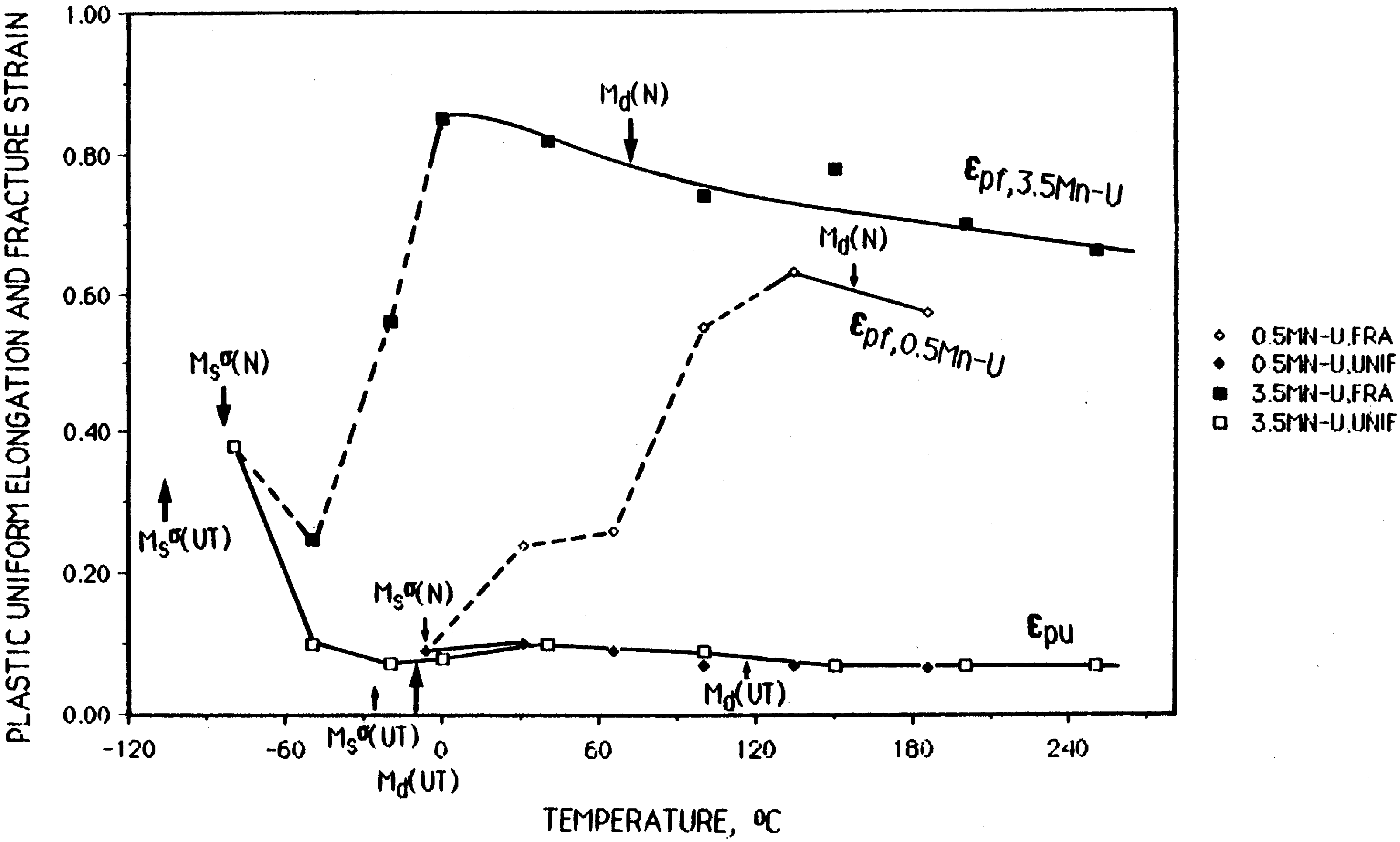

Fig. 5-24 Temperature dependence of fracture plastic strain (ϵ_{pf}) and uniform plastic strain (ϵ_{pu}) for the underaged alloys. Large and small arrows correspond to the mean values of the relevant transformation temperatures for the 3.5Mn-U and 0.5Mn-U alloys, respectively. Dashed lines represent the occurrence of brittle fracture.

$T_{peak,\varepsilon pu}$ and $T_{peak,\varepsilon pf}$ for the underaged alloys are lower than $T_{intergranular}$. This can explain why no appriciable increment of ε_{pu} and ε_{pf} was found in Fig.5-24. Furthermore, the degree of brittleness can be reflected by the temperature difference $\Delta T = T_{intergranular} - T_{peak,\varepsilon pf}$. The magnitudes of ΔT follow the order $\Delta T_{0.5Mn-U} > \Delta T_{3.5Mn-U} > \Delta T_{0.5Mn-O}$ from Table 5-5, which means that 0.5Mn-U is the most brittle material of all the three steels. The lattice parameters of phosphocarbide, listed in Table 5-1, explicitly indicate that the amount of phosphorus remaining in the matrix and hence at the grain boundaries after the aging treatment also follows the same sequence as ΔT for the three alloys. With this coincidence, the embrittlement phenomenon shown by the underaged alloys is believed mainly due to the excess phosphorus segregation at grain boundaries. Analysis of grain-boundary composition using STEM or AES is reqired to further study the role of phosphorus in this embrittling phenomenon.

c. Tensile Fracture

Within the range of testing temperatures studied, the fracture mode of the overaged alloy 0.5Mn-O may be brittle or ductile. When the alloy was tested below 31°C, a mixed mode of dimpled rupture, cleavage, and intergranular fracture is found on the fracture surface in Fig.5-25. Between 65°C and 100°C, the alloy fails by shearing on a plane about 45° to both the direction of loading axis and the normal of the rolling plane, as can be seen from the low-magnification fractograph in Fig.5-25(a). Microscopically, the entire fracture surface displays a pattern of fine dimples in Fig.5-26(b). Between 115°C and 200°C, the delamination phenomenon occurs on planes parallel to the rolling plane in the center of the necked region, as shown in

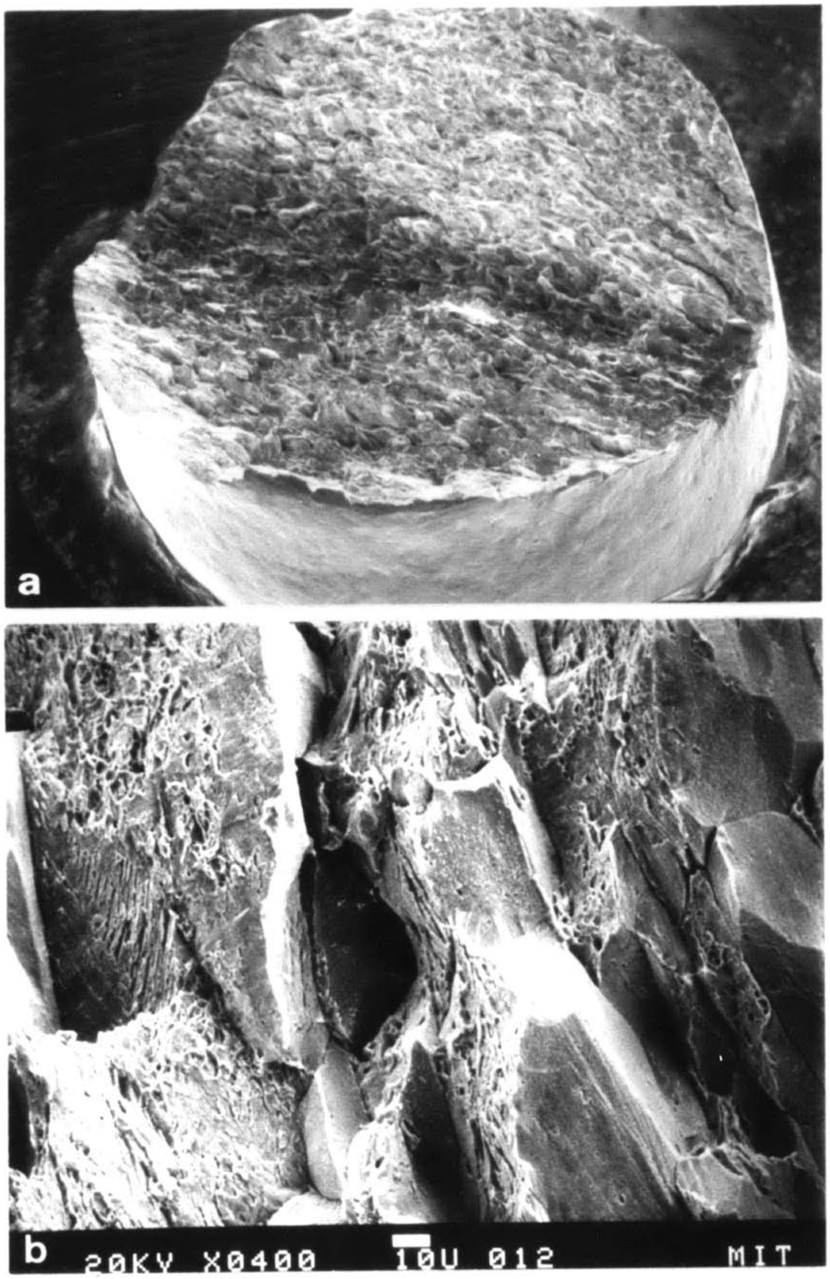

Fig. 5-25 Mixed fracture mode in the 0.5Mn-0 alloy tested at -6ºC.

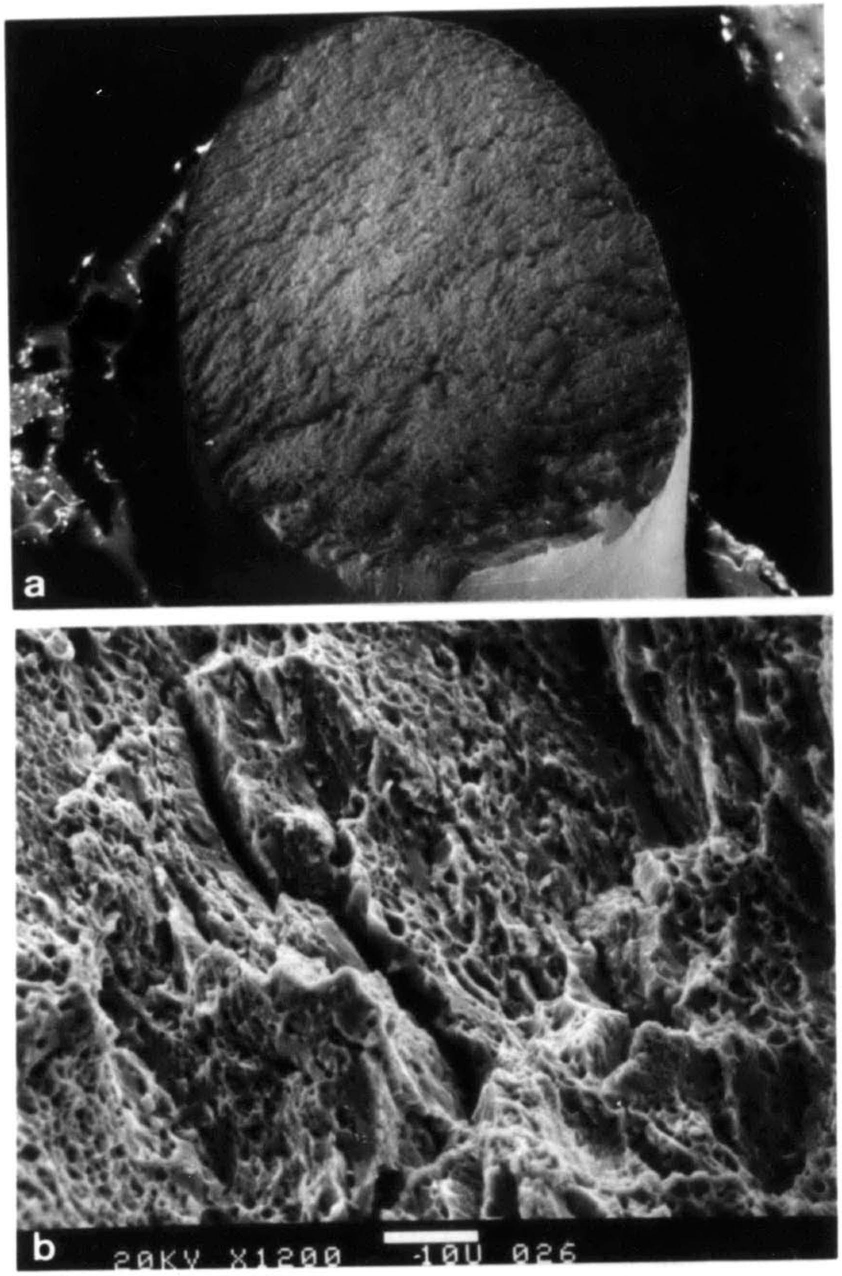

Fig. 5-26 Dimpled rupture in the 0.5Mn-0 alloy tested at 65ºC. The specimen failed by shear on a plane 45º to the loading axis

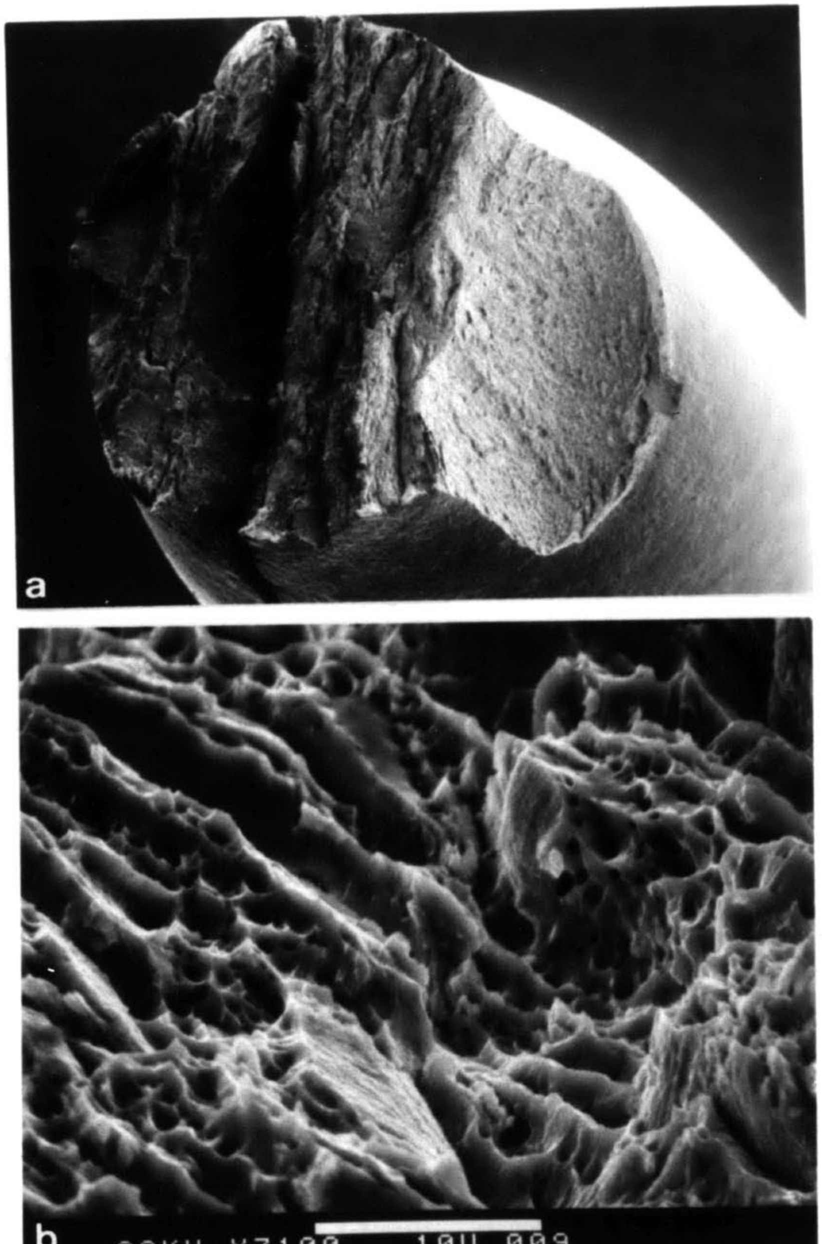

Fig. 5-27 Delamination in the 0.5Mn-0 alloy tested at 115ºC. Elongated dimples are found in the high-magnification micrograph.

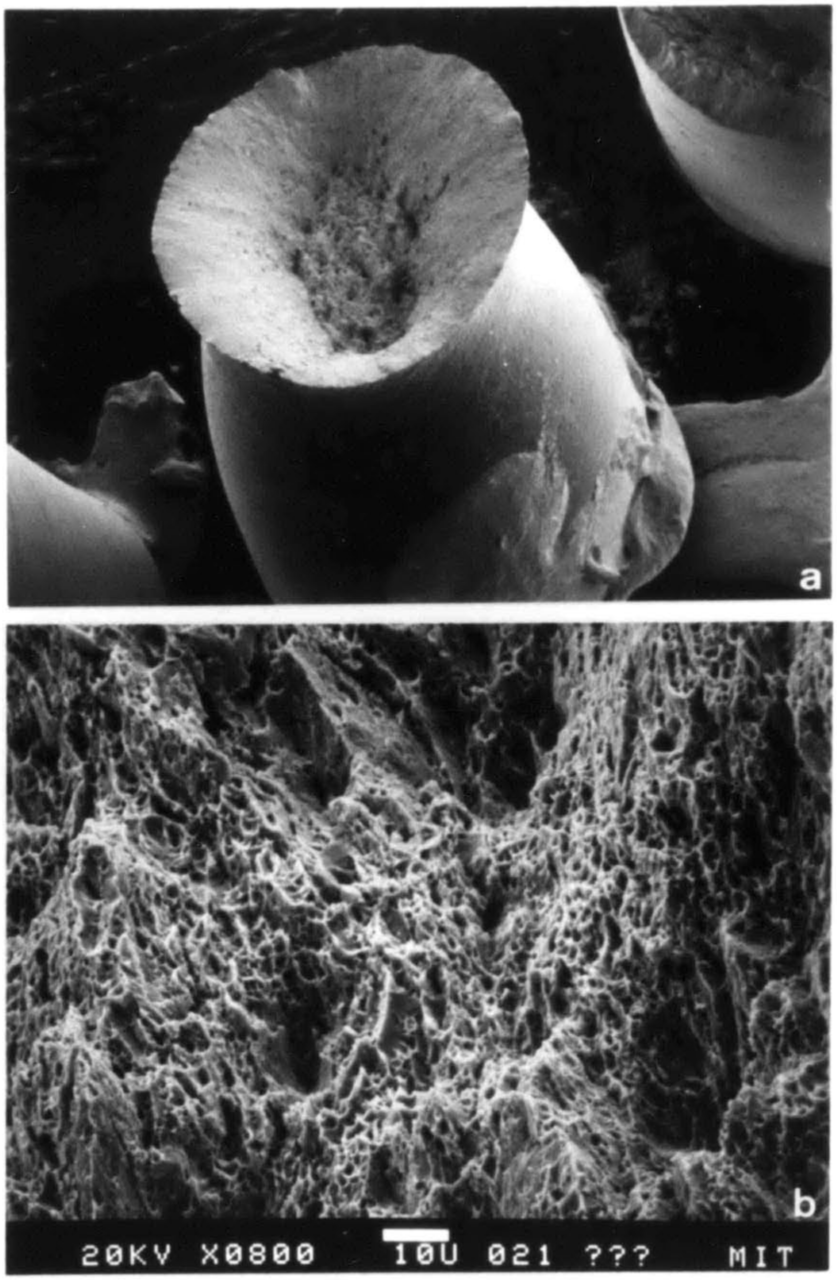

Fig. 5-28 Typical cup-and-cone fracture surface with dimpled topography in the 0.5Mn-0 alloy tested at 250ºC.

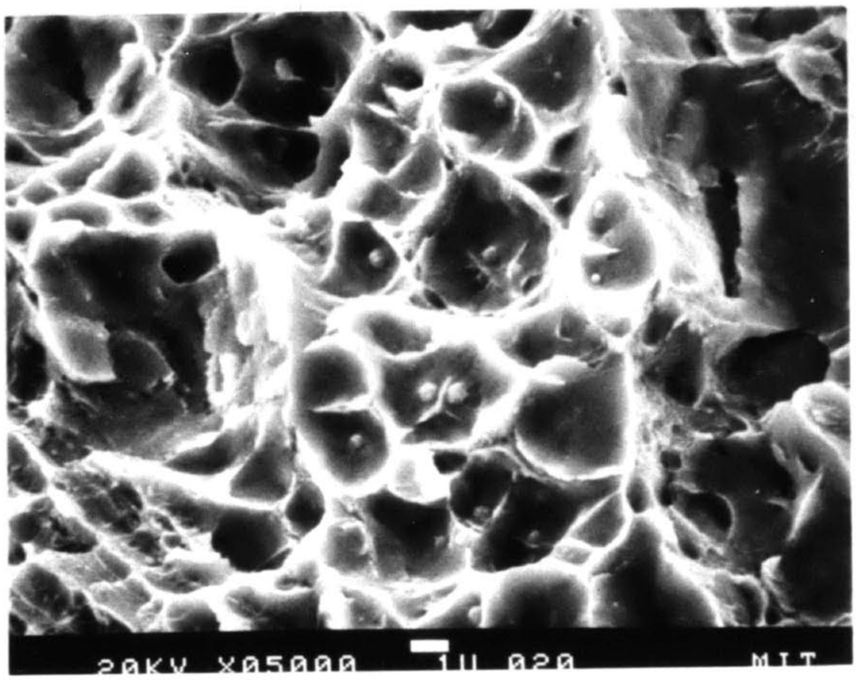

Fig. 5-29 Equiaxed alumina particles are commonly found to sit in the dimples. Micrograph was taken from the tensile fracture surface of the 0.5Mn-0 alloy tested at 200ºC.

Fig. 5-27(a). The observed zig-zag fracture profile in Fig.5-45(a) of Section 5-3-3 and the dimpled rupture surface in Fig.5-27(b) demonstrates that the alloy also failed in shear within this temperature range. At 250°C, a typical cup-and-cone fracture takes place with the dimple morphology shown in Fig.5-28. The high-magnification fractograph in Fig.5-29 reveals that the dimples are evidently formed by the decohesion of interfaces of the equiaxed alumina particles which were identified as the primary void-formers in Section 5-1. Thus far, all of the fractographic analysis has pertained to the overaged alloy. A similar trend of fracture- mode transition is observed in the underaged alloys as well as three-point bend specimens, but with different corresponding temperatures.

5-3-2. Fracture Toughness

a. J_{IC} and Transformation Morphology

Using the methods described in Chapter 4, the J versus Δa curves at various temperatures for all three alloys are plotted in Fig.5-30(a), (b), and (c), respectively. The maximum crack extension for each test is found to be less than 1.6 mm. Within this range of crack advance, the J value is basically linear to the crack advance Δa. The J_{IC} values and the slopes $dJ/d\Delta a$, as determined from the J versus Δa curves, are listed in Table 5-6. For the edge-cracked bend specimens, the initial ligament dimension, b, and thickness dimension, B, should be greater than $25 \cdot J_{IC}/\sigma_0$ for materials with a relatively low strain-hardening exponent, where σ_0 is the flow stress, usually defined as the mean of the yield and ultimate tensile stresses [85]. Using the peak J_{IC} for each alloy and the obtained tensile properties, the

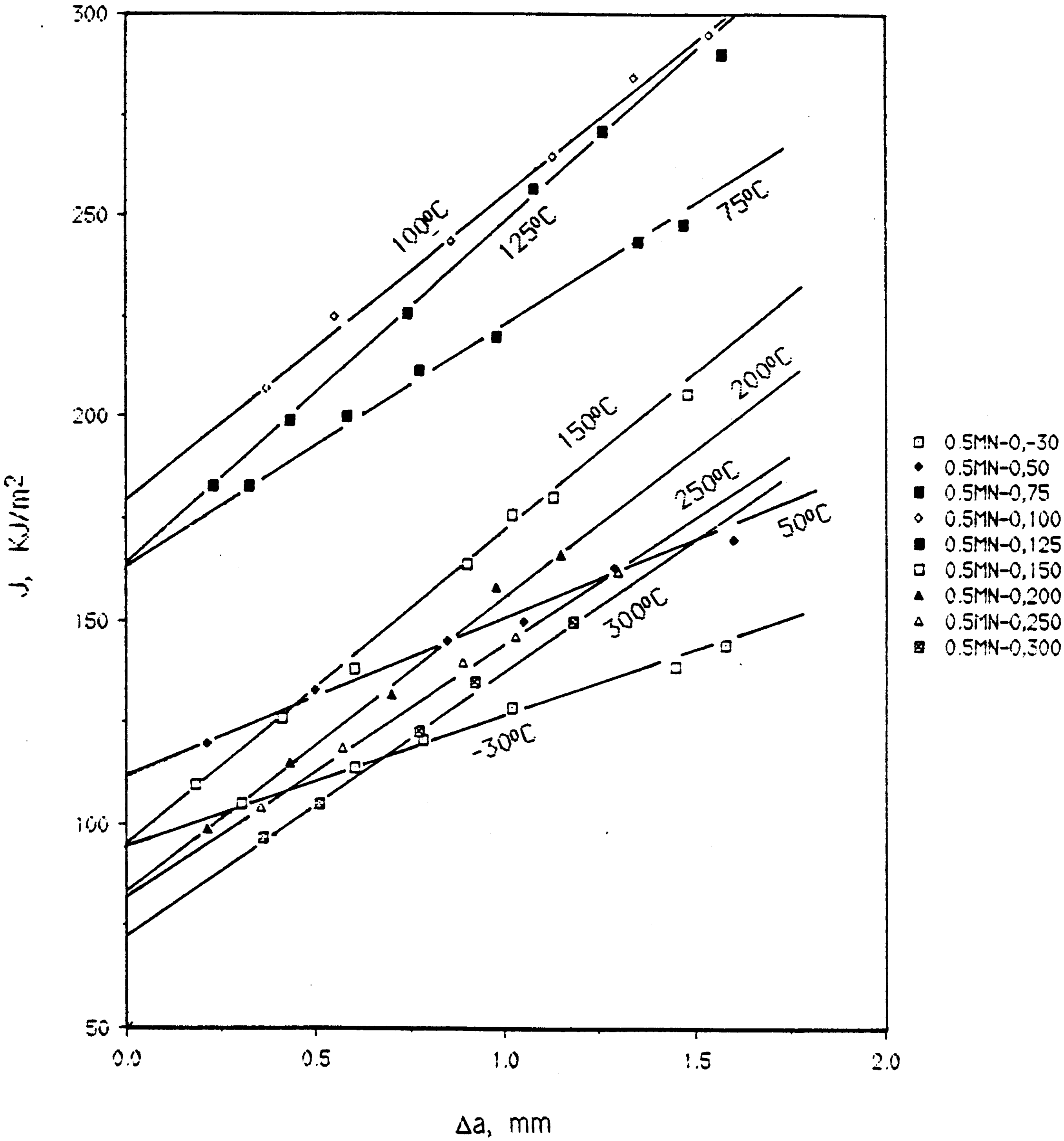

Fig. 5-30(a) J values vs. crack extension at various temperatures for the 0.5Mn-0 alloy. Test temperatures are indicated by the numbers in the legend.

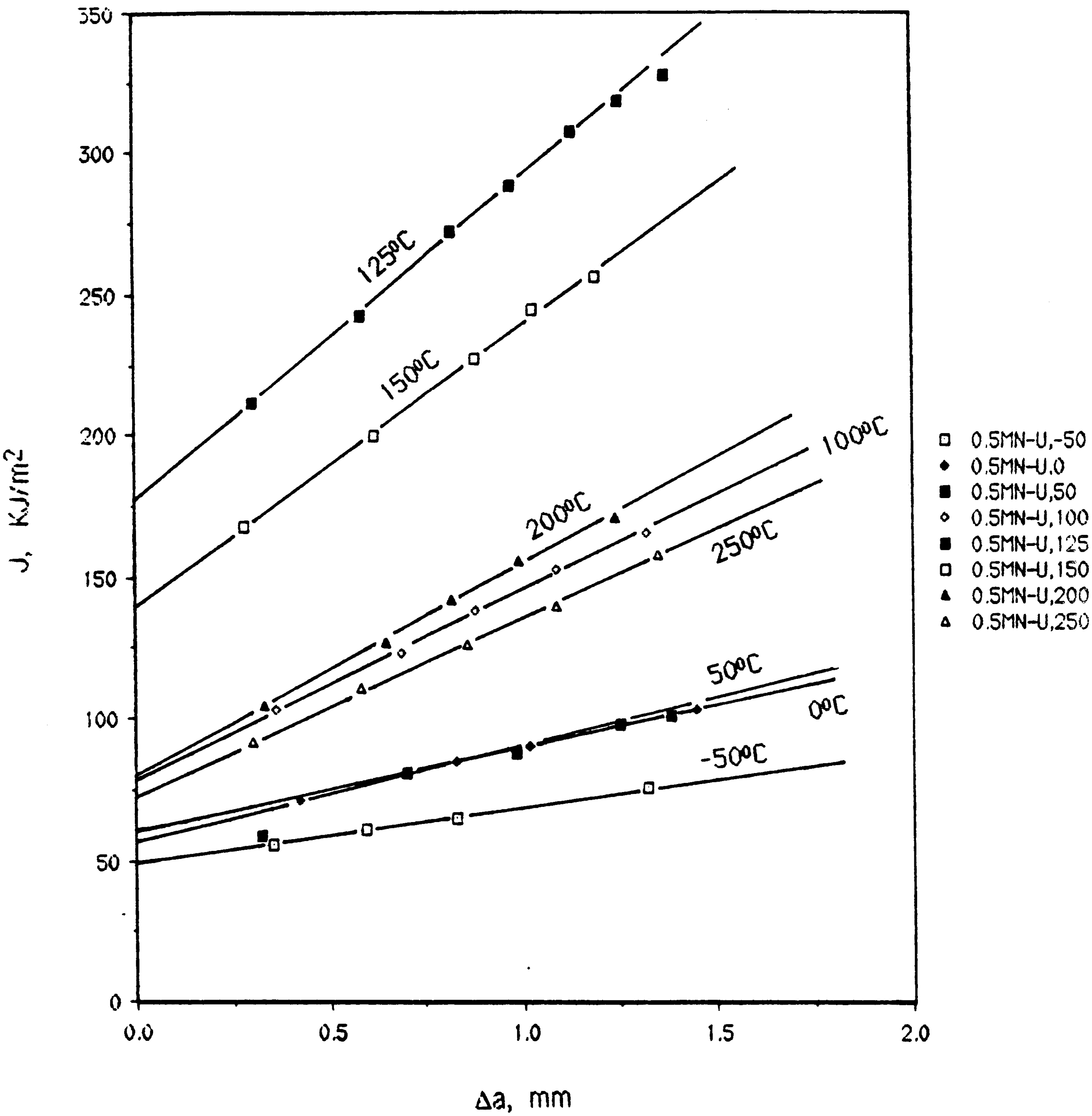

Fig. 5-30(b) J values vs. crack extension at various temperatures for the 0.5Mn-U alloy. Test temperatures are indicated by the numbers in the legend.

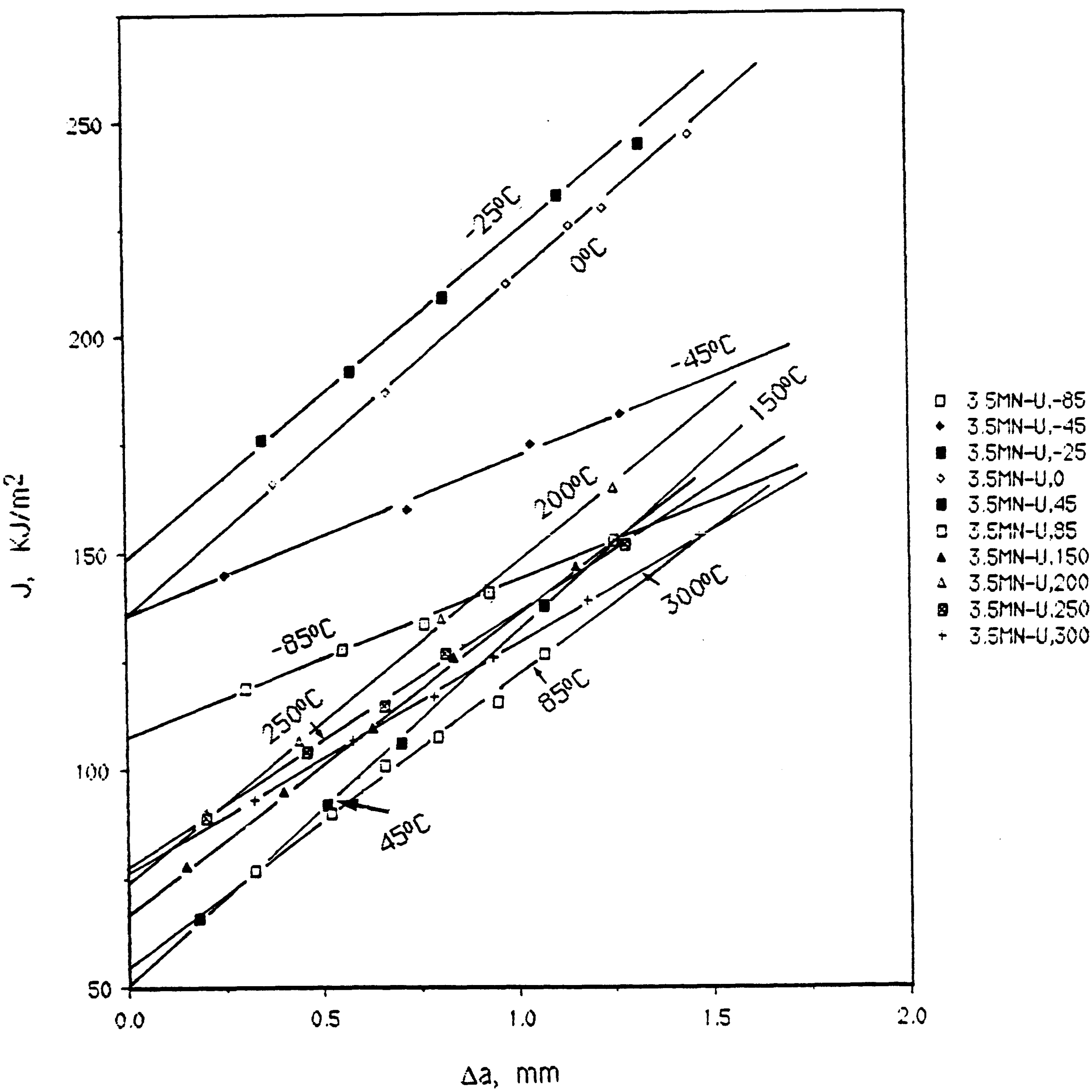

Fig. 5-30(c) J values vs. crack extension at various temperatures for the 3.5Mn-U alloy. Test temperatures are indicated by the numbers in the legend.

Table 5-6. Fracture Properties

0.5Mn-0 Alloy		
T(ºC)	J_{Ic}(kJ/m^2)	dJ/dΔa(Mpa)
-30	95	32
50	115	36
75	167	55
100	179	76
125	162	95
150	93	79
200	85	70
250	83	61
300	74	64
0.5Mn-U Alloy		
T(ºC)	J_{Ic}(kJ/m^2)	dJ/dΔa(Mpa)
-50	49	19
0	58	32
50	61	30
100	80	65
125	179	112
150	140	101
200	80	75
250	73	63
3.5Mn-U Alloy		
T(ºC)	J_{Ic}(kJ/m^2)	dJ/dΔa(Mpa)
-85	112	34
-45	138	38
-25	151	72
0	136	87
45	52	78
85	55	68
150	67	70
200	76	72
250	77	59
300	76	53

maximum value of $25 \cdot J_{Ic}/\sigma_0$ is calculated to equal 2.65 mm and is much less than b and B used in this work, as indicated in Fig.4-4. Thus, the obtained J_{Ic} can be considered a valid measurement of toughness under plane strain.

The temperature dependence of J_{Ic} values for the three alloys is summarized in Fig.5-31, along with their effective transformation temperatures around the crack-tip. Again, intergranular fracture occurred at low temperatures for each alloy, as indicated by dashed lines in Fig.5-31. With decreasing temperature from M_d, the J_{Ic} value of the overaged 0.5Mm-O alloy first increases to a maximum at about 100°C, then decreases at still lower temperatures. For the underaged 3.5Mn-U alloy, no transformation was found at temperatures between 300 and 85°C and these J_{Ic} values represent the fracture toughness of the parent phase. In general, the toughness of austenite decreases with decreasing temperature as replotted in Fig.5-32. From comparisons of the J_{Ic} values at 250 or 300°C, the three alloys possess a comparable toughness when the influence of transformation is absent. There is no significant increase of the J_{Ic} values for the 3.5Mn-U alloy until temperature decreases below 45°C, at which the toughening effect due to the small amount of transformation around the crack-tip may not be sufficient to compensate for the J_{Ic} drop arising from the temperature decrease. Unlike the temperature dependence of the fracture strain in Fig.5-24, the J_{Ic} values of the 3.5Mn-U alloy pass through a peak value at -25°C before the brittle fracture intervenes in the failure of material. Though a remarkable J_{Ic} increment is found for the underaged alloy 0.5Mn-U at temperatures between 200 and 125°C, the optimum J_{Ic}

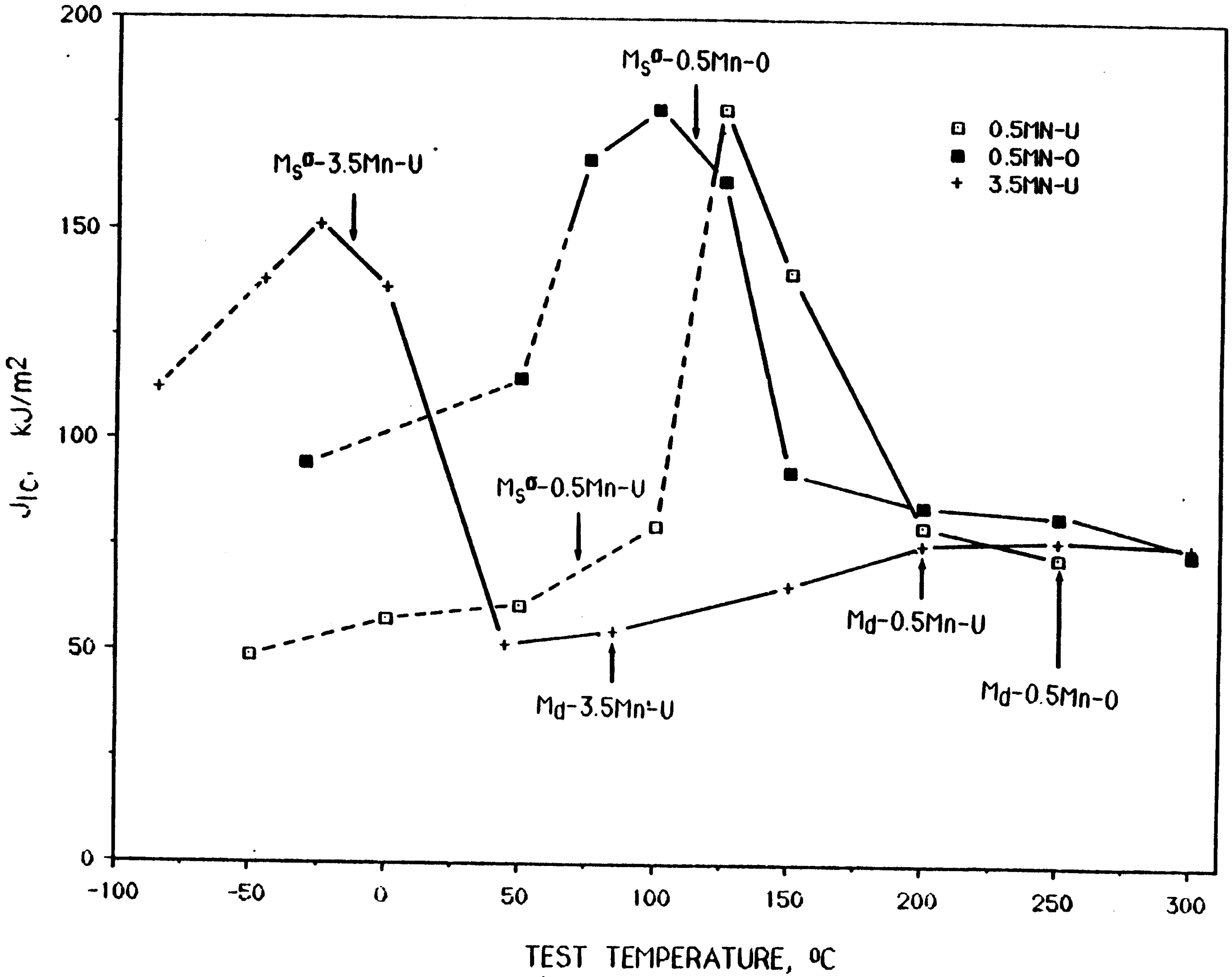

Fig. 5-31 Temperature dependence of fracture toughness for the three alloys. Dashed line in each curve represents the brittle fracture regime.

still can not be obtained due to the ductile-brittle transition of the austenitic phase, as concluded from the observed fracture strain.

The J_{IC} value of the stable austenitic phase in the phosphocarbide-strengthened steels is only half that of the γ'-strengthened austenitic steels [1], apparently resulting from the contamination by aluminum oxide colonies introduced during the rapid solidification process. However, they present a better transformation toughening effect than most of γ'-strengthened austenitic steels. Fig.5-33 illustrates the absolute enhancement of toughness ($\Delta J_{IC} = J_{IC} - J_{IC,aust.}$) versus the temperature interval ($T-M_s^{\sigma}(CT)$). The highest toughness enhancement can be over 100kJ/m^2 or twice of the toughness of the parent phase for all three alloys. The peak ΔJ_{IC} occurred at a temperature sightly below $M_s^{\sigma}(CT)$ for both the 0.5Mn-O and the 3.5Mn-U alloys, but at a temperature much above $M_s^{\sigma}(CT)$ for the 0.5Mn-U alloy because of the interference of the brittle fracture. If the premature brittle fracture could be avoided, the latter was supposed to exhibit the best toughness increment among the three alloys, having the strongest martensite as well as the largest transformation volume change.

Following the above tests, the microstructure in the vicinity of the crack was examined using optical microscopy. At temperatures below $M_s^{\sigma}(CT)$, a large amount of plate martensite is formed, as shown in Fig.5-34 for the 0.5Mn-O alloy tested at -30°C. A nearly complete transformation takes place during the last two-thirds of crack extension. A small crack-tip opening indicates that the crack passed rapidly through that region. This suggests that plate martensite is quite brittle at the test temperature and substantially reduces the resistance to crack initiation and growth. No

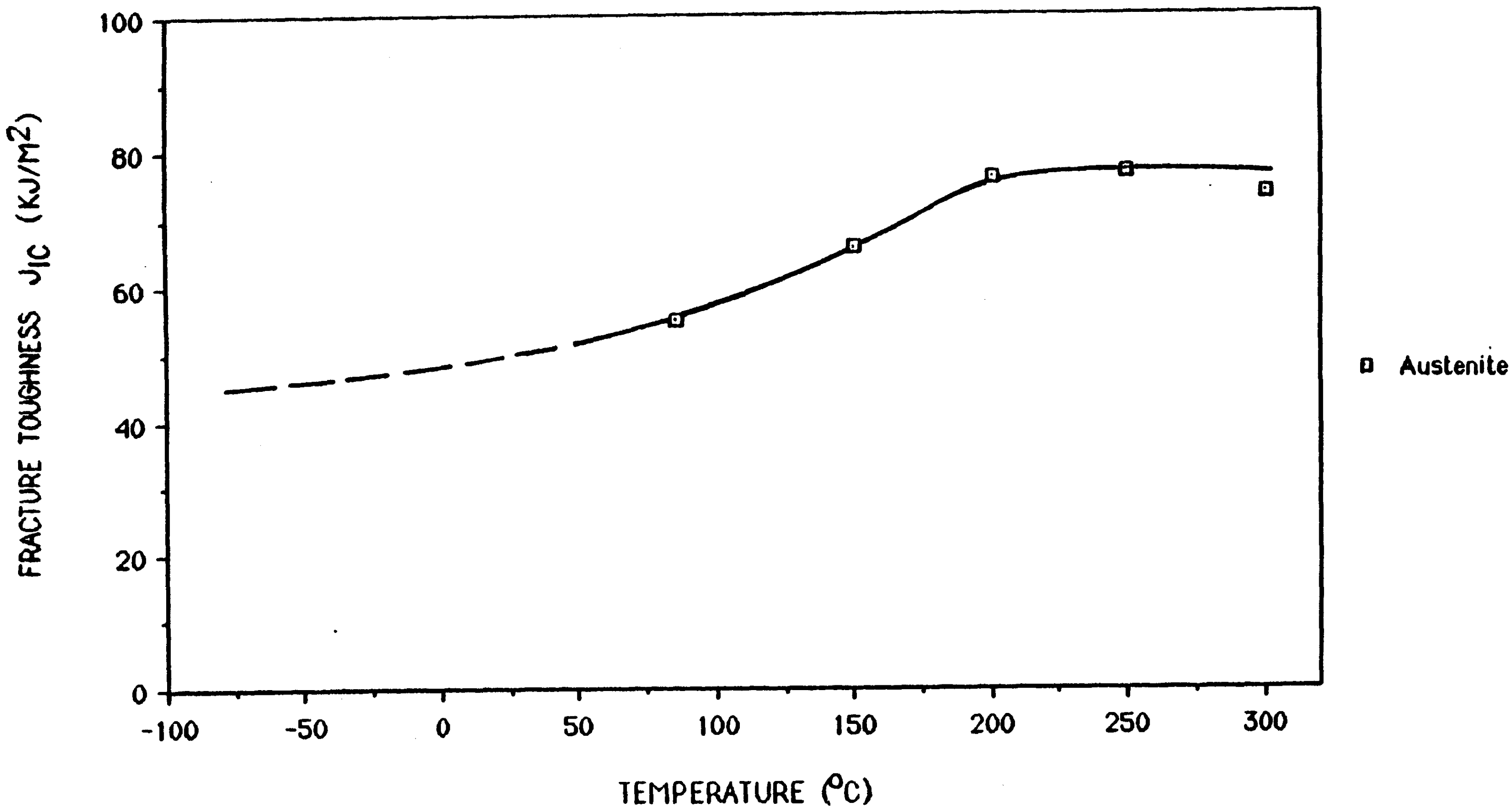

Fig 5-32 Fracture toughness of the austenitic phase estimated from the measured J_{IC} values of the 3.5Mn-U alloy above M_d.

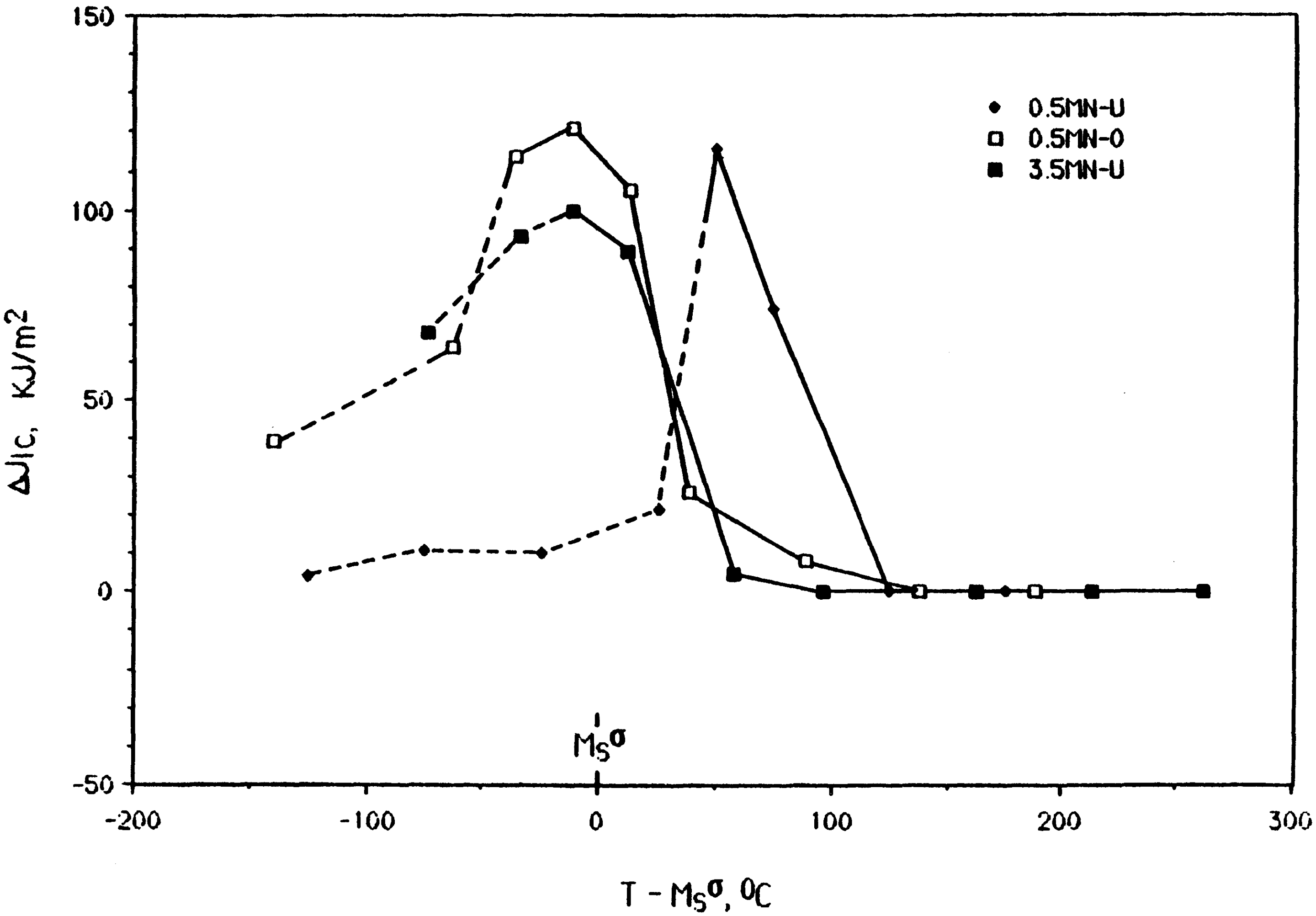

Fig. 5-33 Enhancement of fracture toughness vs. temperature difference ($T-M_s^{\sigma}$)

martensite is found except in the region adjacent to the crack induced by the bending test. This verifies that the fatigue precracking performed at 250°C can avoid martensite formation and hence its effect on the J_{Ic} measurements. At temperatures above M_s^{σ}(CT), fine lath martensite is formed around the crack-tip in Fig.5-35 for the 0.5Mn-0 alloy at 125°C. It also shows that the crack-tip is significantly blunted before further extension and improved crack growth resistance is expected. With further increase of test temperature near M_d(CT), the strain-induced transformation is limited to a narrower zone in Fig.5-36 and corresponds to a smaller toughness enhancement. The other alloys also followed a similar trend. At temperatures above M_s^{σ}(CT), the transformation zone size appears to be a stronger function of test temperature than the amount of visible transformation. The latter is more difficult to quantify because of the fineness of lath-martensite morphology as well as its inhomogeneous distribution. In Section 5-3-4, the relation between the zone size and the toughness will be discussed.

b. Temperature Dependence of $dJ/d\Delta a$

Although the J_{Ic} value is the most widely measured and quoted toughness property for ductile materials, there has been a trend to consider the crack-growth resistance as an additional assessment of toughness. In the J approach, the crack- growth toughness can be evaluated in terms of the non-dimensional tearing modulus ($T_R = E/\sigma_0^2 \cdot dJ/d\Delta a$) [86]. Two requirements have been identified for J-controlled crack growth [87]. First, the region of elastic unloading has to be small compared to the region controlled by the HRR singularity. In addition, J must increase sufficiently rapidly with crack

Fig. 5-34 Optical micrograph showing a large amount of plate martensite in the vicinity of crack extention during bend test for the 0.5Mn-0 alloy at -30ºC. Etchant : 167ml methanal, 33ml water, 0.5g sodium metasulfite.

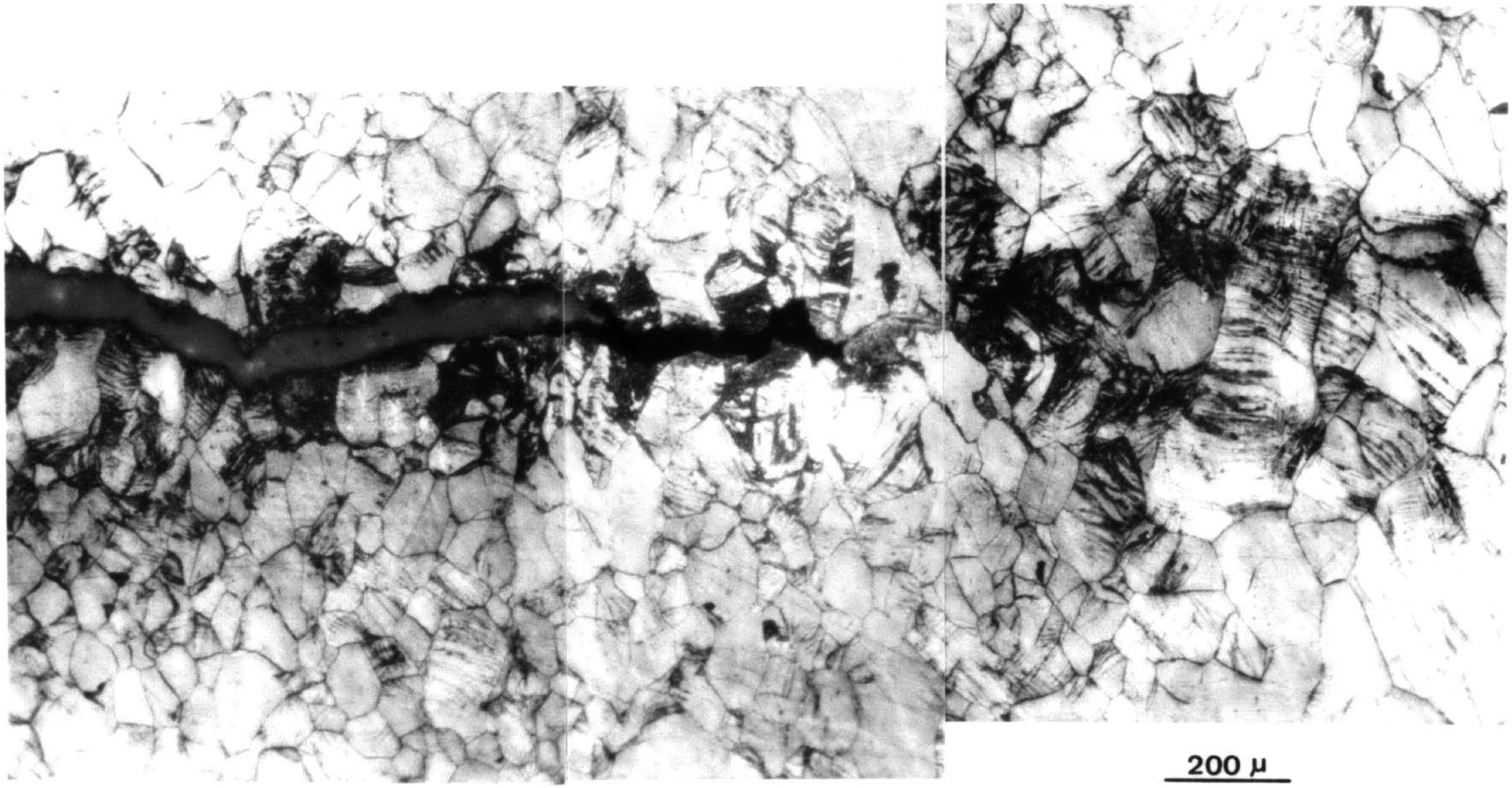

Fig. 5-35 Lath martensite formed around the crack in the 0.5Mn-0 alloy during bend test at 125ºC. Etchant : 167ml methanal, 33ml water, 0.5g sodium metasulfite.

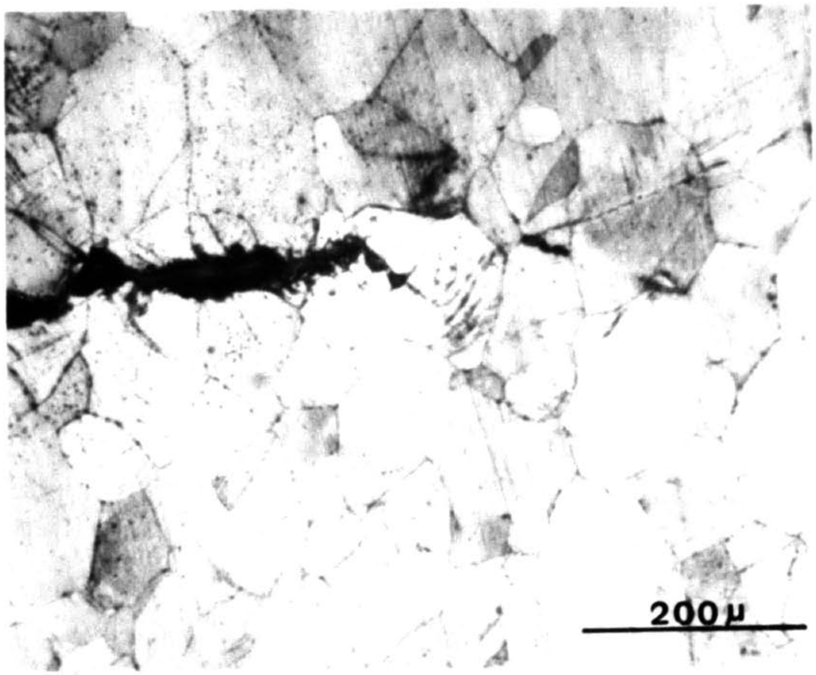

Fig. 5-36 Only few martensitic laths were found in a very small region around a crack in the 0.5Mn-0 alloy tested at 200ºC. Etchant : 167ml methanal, 33ml water, 0.5g sodium metasulfite.

extension such that the region of non-proportional plastic loading is small, i.e., the parameter $\omega = b/J_{Ic} \cdot dJ/d\Delta a >> 1$. The minimum permissible value of ω is suggested to be on the order of 10. Fig.5-37 shows the temperature dependence of $dJ/d\Delta a$ for the three alloys. The calculated values of ω are in the range of 1.5 to 6 so that the crack growth may not be entirely J-controlled. However, the variation of $dJ/d\Delta a$ is basically consistent with the crack width seen in metallographic observation. The resistance of crack growth was improved by the presence of strain-induced lath martensite, but became poor as a large amount of plate martensite formed ahead of the crack-tip or as intergranular fracture occurred.

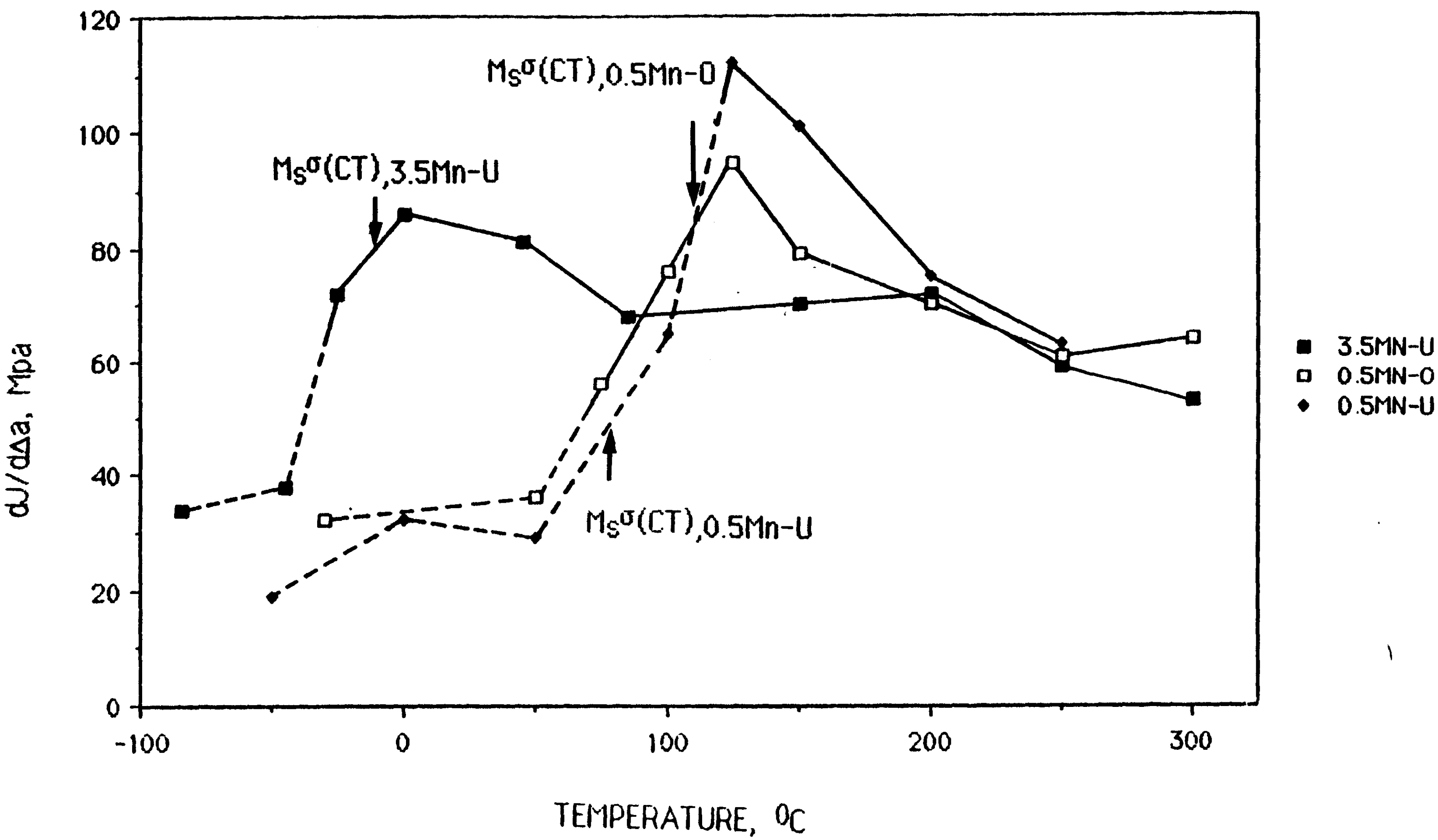

Fig. 5-37 Temperature dependence of dJ/dΔa.

5-3-3. Quantitative Assessment of Ductility

Despite the influence of brittle fracture, the highest possible values of uniform strain and fracture strain for the phosphocarbide-strengthened alloys occurred between the relevant M_s^σ and M_d temperatures, where the strain-induced martensitic transformation is dominant. In fact, that is the most appropriate temperature range for tha application of TRIP steels considering the rapid drop of yield stress below M_s^σ(UT) as well as the variation of toughness. Based on analysis of the shape of stress-strain curves, two factors were reported to contribute to the ductility enhancement [61]. One is the well-known static-hardening effect associated with forming the stronger martensite; the other is the dynamic softening effect arising from the operation of the martensitic transformation as a deformation mechanism. Comparing the plastic flow properties of metastable austenite, stable austenite, and martensite, Narutani et al. [30] were able to estimate these two effects and derive an empirical constitutive relation for the metastable austenite in the strain-induced regime. From the observed strain-induced transformation kinetics in Section 5-2-2 and the flow relations of γ and α' phases, the enhancement of uniform elongation and fracture strain for the 0.5Mn-0 alloy can be understood by applying the Narutani relation suitable with criteria for flow instability and ductile fracture.

a. Flow Relations

The relations between true stress and true plastic strain for the austenite and the martensite in the 0.5Mn-0 alloy were determined by uniaxial compressive testing rather than tensile testing in order to avoid the interference of necking. Comparing the yield stresses in tension and in compression at temperatures higher than 150°C in Fig.5-11, the strength-differential effect is small for the 0.5Mn-0 alloy so that the $\sigma-\varepsilon_p$ relation of the austenite in tension can be considered to be the same as that in compression. A similar assumption was adopted for the martensite. The $\sigma-\varepsilon_p$ data of the austenite and martensite were fitted to a power equation :

$$\sigma = \sigma_0 \cdot (\varepsilon_0 + \varepsilon_p)^n \qquad (5-7)$$

where the temperature dependence of stress is only taken into account in the parameter σ_0, and the strain-hardening exponent n and parameter ε_0 are assumed to be independent of temperature within the investigated temperature range of 50 to 200°C. Fig.5-38 shows the fitted results at 160°C. The $\sigma-\varepsilon_p$ relations of the austenite were first fitted using the true plastic uniform strain in tension, 0.06, as the n value. Since the 0.5Mn-0 alloy is too stable to transform spontaneously even at -196°C, a tensile stress was applied at -70°C to produce 92% martensite within the gage length of the tensile specimen from which the compressive specimens were made. Note that the tensile prestraining was performed until a Luders band had propagated through the whole gage length. At that stage, the imposed stress was even lower than the yield stress of the parent phase and hence strain-hardening due to deformation by slip might not occur in the martensite. Using the rule of mixtures and the austenitic $\sigma-\varepsilon_p$ relation, the measured compressive stress and strain data of the two-phase alloy at 160°C were converted to those of martensite, and then were fitted to Eq.5-7 in Fig.5-38. In addition to the higher strength level, the martensitic phase

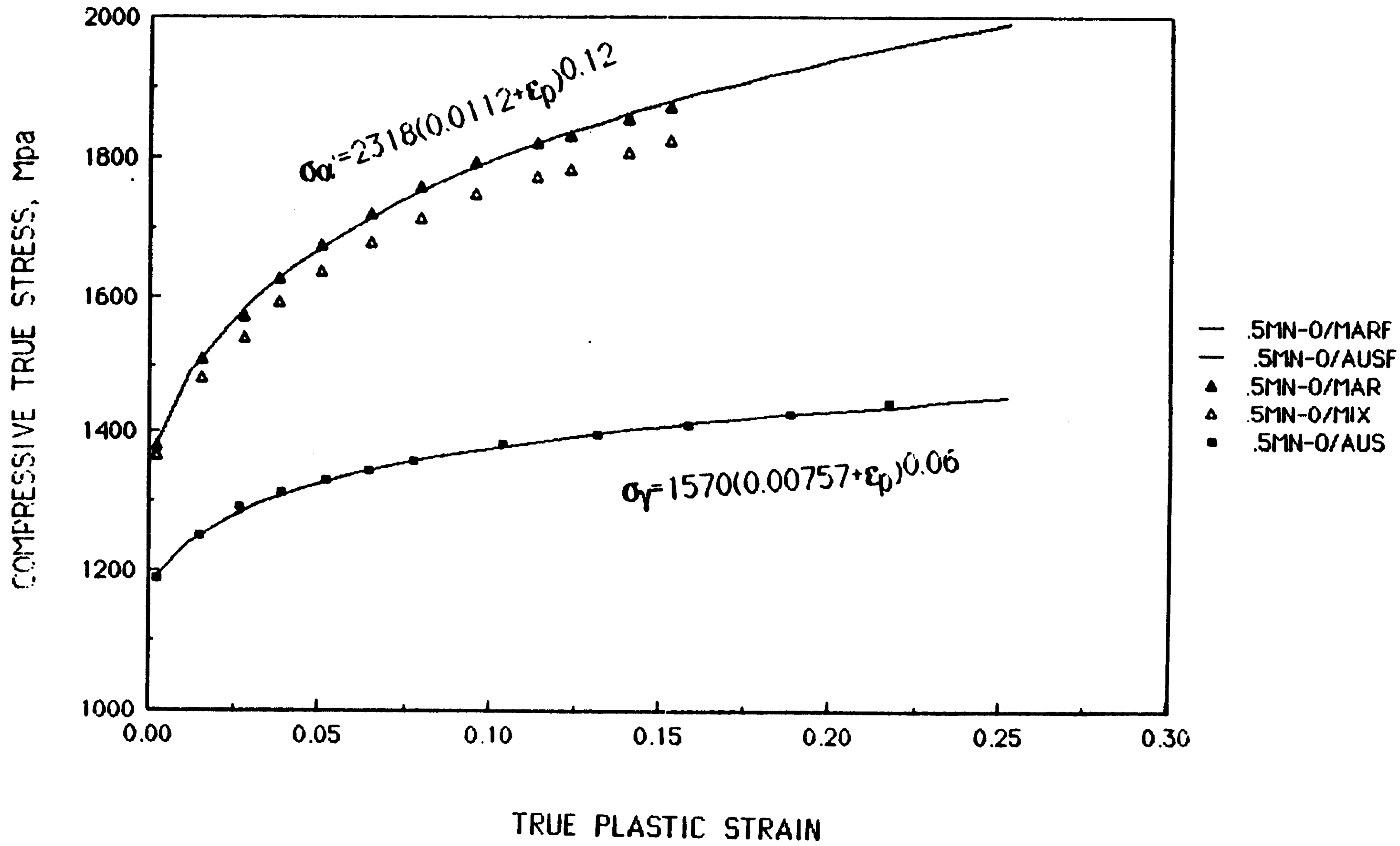

Fig. 5-38 Compressive true stress-strain curves of austenite and martensite for the 0.5Mn-0 alloy at 160°C. Open triangles represent the stresses corresponding to a mixture of 92% martensite and 8% austenite.

shows a stronger tendency toward strain-hardening than does the austenitic phase, with the hardening exponent being comparable to that of martensitic steels, such as AISI4340 [86].

In general, the 0.2% yield stresses of both phases increase linearly with temperature in the range of 0 to 200°C, but with different slopes, as shown in Fig.5-39. The martensite strength is more susceptible to temperature change than the austenite because of its different crystallographic structure. Besides the transformation kinetics, the variation of strength difference with temperature will also provide a minor effect on the shape of the stress-strain curve. Considering the influence of temperature, the σ–ε_p relations of two phases for the 0.5Mn-0 alloy can be expressed as :

$$\sigma_\gamma = (1690-0.74T)\cdot(0.00757+\varepsilon_p)^{0.06} \qquad (5\text{-}8)$$

and

$$\sigma_{\alpha'} = (2587-1.68T)\cdot(0.0112+\varepsilon_p)^{0.12} \qquad (5\text{-}9)$$

Using the measured transformation kinetics in the Section 5-2-2 and Eqs.(5-8) and (5-9), the constitutive relations dealing with the strain-induced martensitic transformation for the 0.5Mn-0 alloy are predicted from the Narutani relation, as introduced in Section 2-1-2. Eq.2-10 is rewritten here :

$$\sigma = \{[1-f_{\alpha'}]\cdot\sigma_\gamma(\varepsilon_p-\alpha'\cdot f_{\alpha'}) + f_{\alpha'}\cdot\sigma_{\alpha'}(\varepsilon_p-\alpha'\cdot f_{\alpha'})\}\cdot(1-\beta'\cdot df_{\alpha'}/d\varepsilon_p) \quad -(2\text{-}10)$$

An upper limit of the coefficient α' for the 0.5Mn-0 alloy equals 0.08 from the slope of the observed $f_{\alpha'}$ vs. ε_p line in the stress-assisted regime shown

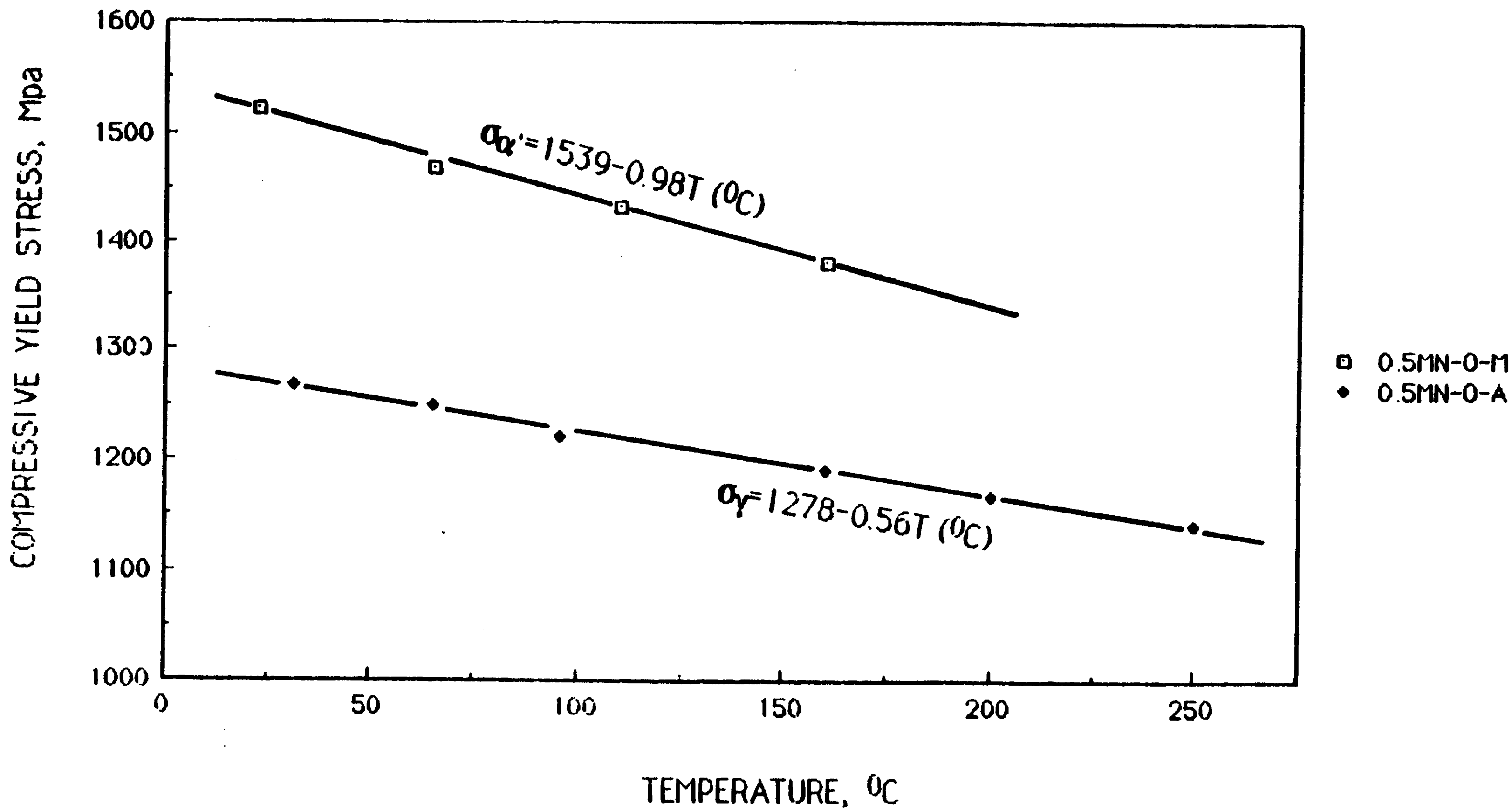

Fig. 5-39 Temperature dependence of 0.2% compressive yield stress of martensite and austenite in the 0.5Mn-0 alloy.

in Fig.5-17. Taking the derivative of σ in Eq.2-10 with respect to ε_p, the strain-hardening rate can be expressed in terms of $f_{\alpha'}$, σ_γ, $\sigma_{\alpha'}$, and their derivatives as a function of ε_p, $\dot{\varepsilon}_p$, and T.

The coefficient β' is so far the only unknowm in Eq.2-10 for the 0.5Mn-0 alloy. Because of the material shortage, the coefficient β' could not be evaluated from the prestrain tensile tests. As an alternative, it was determined by fitting Eq.5-12 to the measured tensile true stress vs. true plastic strain curves along with the fitted kinetics and the flow relations of two phases. The tensile σ - ε_p curve at 65ºC (> M_s^σ(UT)) is the best one for this purpose. Not only can the alloy sustain the largest (uniform) deformation (and hence transformation) under a constant stress-state of uniaxial tension, but also the local change of specimen dimension caused by the Luders band phenomenon at low strains is negligible. Fig.5-40 shows the best fitting result for which β'=0.015 was used. Though the calculated flow stress is in good agreement with the observed value, the slope (or strain-hardening rate) tends to be overestimated in the strain range of 0.20 to 0.26, but underestimated at strains beyond 0.26. The latter leads to an underestimate of the the uniform strain, as represented by point "a" in Fig.5-40, by 0.08. Such a minor mismatch may result mainly from the local discrepancy betweem the measured kinetic data and the values fitted by the Olson-Cohen model, as can be seen in Fig.5-17. Considering the complex interaction of general slip and transformation in the strain-induced mode, the agreement of the predicted flow relation is acceptable.

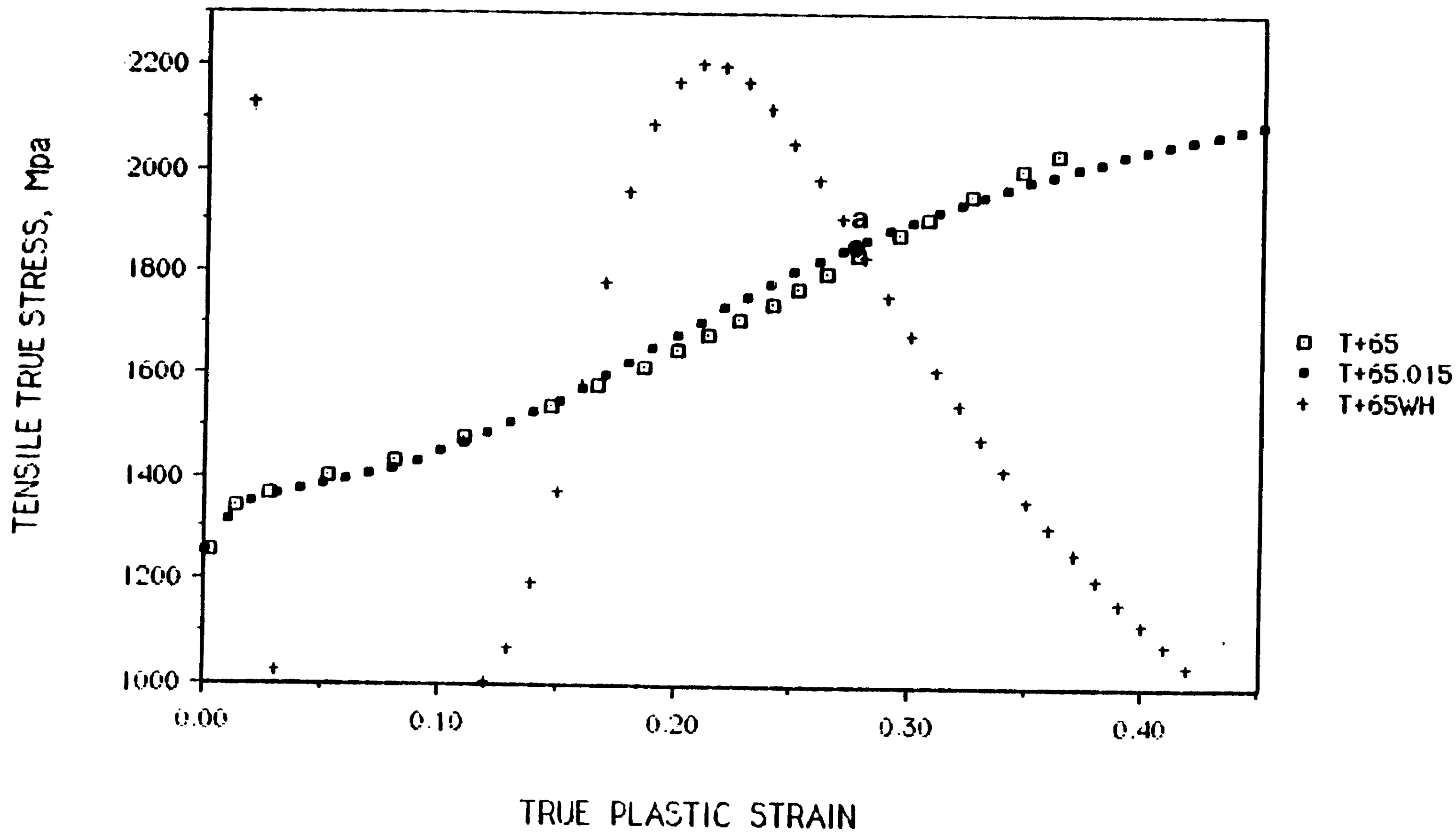

Fig. 5-40 The measured stress-strain curve (open squares) is fitted to the Narutani equation as shown by the solid squares. The values of strain-hardening rate are also calculated for the fitted curve as marked by crosses.

b. Criteria for Plastic-Flow Instability and Shear-Instability-Controlled Fracture

The best way to understand the ductility enhancement due to the strain-induced transformation is by examining the deformation dependence of a normalized strain-hardening rate, $h/\boldsymbol{\sigma}$, where h is the effective strain-hardening rate ($= d\boldsymbol{\sigma}/d\varepsilon_p$), $\boldsymbol{\sigma}$ are ε_p the effective stress and plastic strain. A good example for this purpose is shown in Fig.5-41, in which the $h/\boldsymbol{\sigma}$ values of a γ'-strengthed metastable austenite 31Ni(L) were calculated at both $\theta=1(=M_d)$ and $\theta=0.6$ ($M_s^{\sigma}<T<M_d$) using the method described earlier. The $h/\boldsymbol{\sigma}$ of stable austenite decreases monotonically as represented by the dashed curve, while the $h/\boldsymbol{\sigma}$ value for the transforming austenite (at $\theta=0.6$) follows a "S" shape curve as a result of the combined effect of dynamic softening and static hardening. These two effects are mainly controlled by both the shape of the sigmoidal $f_{\alpha'}-\varepsilon_p$ curve and the strength difference between α' and γ phases. At low strains, the dynamic softening (proportional to $d^2f_{\alpha'}/d\varepsilon_p^2$) is the dominant factor and causes the decrease of $h/\boldsymbol{\sigma}$ even faster than for the stable austenite in this case. By increasing the plastic strain, the softening effect becomes weaker and finally ceases until negative $d^2f_{\alpha'}/d\varepsilon_p^2$ is found. In the mean time, the static-hardening rate (proportional to $df_{\alpha'}/d\varepsilon_p$) becomes faster than the softening rate and results in the increase of $h/\boldsymbol{\sigma}$ to a peak value. Afterwards, the static-hardening effect decreases because of slower transformation rate and $h/\boldsymbol{\sigma}$ begins to drop.

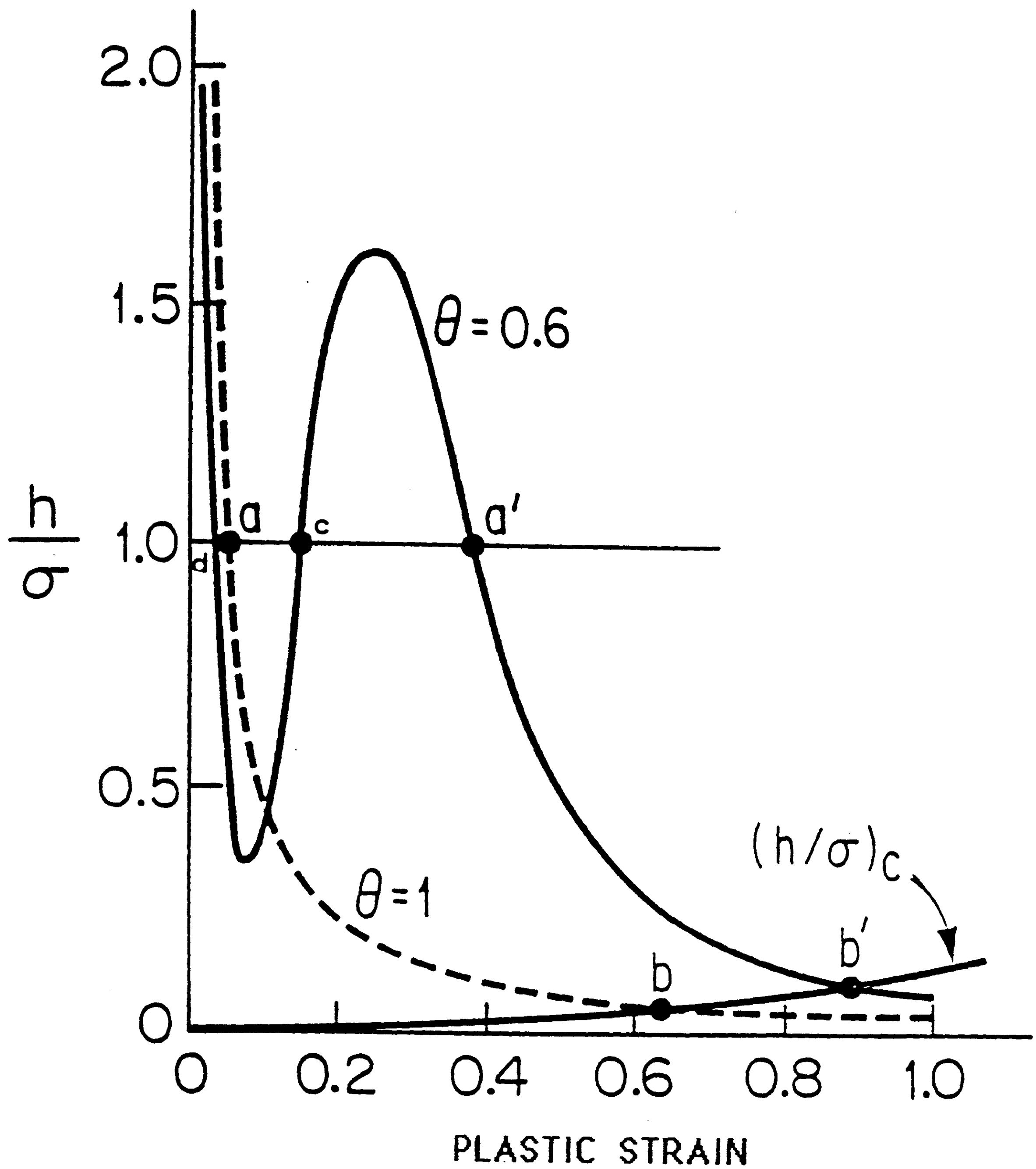

Fig. 5-41 Normalized strain-hardening rate h/σ vs. plastic strain for a γ'-strengthened metastable austenite at $\theta=1$ ($T=M_d$) and $\theta=0.6$ ($M_s^{\sigma}<T<M_d$). Horizontal line, $h/\sigma=1$, corresponds to tensile necking condition, while $(h/\sigma)_c$ is condition for shear-instability-controlled fracture in tensile neck.

For a constant volume material, the minimum strain-hardening rate required to maintain stable flow in uniaxial tension is equal to the flow stress [89]:

$$d\boldsymbol{\sigma}/d\varepsilon_p = \boldsymbol{\sigma}$$

or

$$h/\boldsymbol{\sigma} = (d\boldsymbol{\sigma}/d\varepsilon_p)/\boldsymbol{\sigma} = 1 \qquad (5\text{-}10)$$

Considering the volume change arising from the martensitic transformation, Eq.5-10 can be expressed as a function of the dilatation, $\delta = \Delta V/V_\gamma$, the martensite volume fraction, $f_{\alpha'}$, and the slope of the transformation curve, $df_{\alpha'}/d\varepsilon_p$:

$$d\boldsymbol{\sigma}/d\varepsilon_p = \boldsymbol{\sigma} \cdot \{1 - [(\delta/(1+\delta \cdot f_{\alpha'})) \cdot (df_{\alpha'}/d\varepsilon_p)]\}$$

or

$$h/\boldsymbol{\sigma} = 1 - [(\delta/(1+\delta \cdot f_{\alpha'})) \cdot (df_{\alpha'}/d\varepsilon_p)] \qquad (5\text{-}11)$$

which is less than 1 because the term in brackets is alway positive. Eq.5-11 indicates that dilatation allows further delay of the onset of unstable flow or necking. Substituting the numerical data of $f_{\alpha'}$, and $df_{\alpha'}/d\varepsilon_p$ at 65°C and δ for the 0.5Mn-0 alloy in Eq.5-11, the $h/\boldsymbol{\sigma}$ values are in the range of 0.927 to 0.989 with ε_p from 0.2 to 0.4. At higher temperatures, the value of $h/\boldsymbol{\sigma}$ in Eq.5-11 is even closer to 1 because of the less-steep transformation curve. Therefore, for the sake of simplicity, the criterion for necking will be taken as Eq. 5-10 as shown by a horizontal line in Fig.5-41. For the stable austenite, stable plastic flow can only be maintained at strains below point "a". On the other hand, there are three intersection points "d", "c", and "a'" between the the h/σ vs. ε_p curve at θ=0.6 and the h/σ = 1 line. A transient instability or Luders band phenomenon occurs at "d", but disappears at "c" which is the Luders strain. Final necking will not occur until the strain reaches point a' and the enhancement of uniform strain at θ=0.6 corresponds to the line segment a-a'. The maximum ε_{pu} can be found at a certain temperature $\theta > 0.6$ at which the local maximum of the h/σ vs. ε_p curve just touches the h/σ = 1 line. At still higher temperatures, the h/σ value is unable to exceed above 1 again and the enhancement of uniform strain is almost absent.

The topography of the fracture surface showed that the 0.5Mn-0 alloy failed by shear instability due to microvoid formation around the fine alumina particles in the temperature range between $M_s^\sigma(n)$ and $M_d(n)$. As proposed by Needleman and Rice [47], the hardening rate of a porous material must be maintained above a critical value, $(h/\sigma)_c$, to prevent shear localization induced by void-softening. Furthermore, Knott [41] pointed out that once the shear localization occurs, the material will fail with a very small strain increment. Hence, the fracture strain can be estimated from the comparison of the h/σ vs. ε_p curve and the proposed critical hardening-rate in Eq.2-11. Assuming that the shear localization is controlled by void growth with an approximation of void volume fraction linearly proportional to ε_p, the Needleman-Rice criterion in Eq.2-11 can be simplified as :

$$(h/\sigma)_c = k\varepsilon_p \cdot \cosh(1.5 \cdot \sigma_h/\sigma) \sinh(1.5 \cdot \sigma_h/\sigma) \qquad (5-12)$$

where coefficient k is a material parameter related to void growth rate with respect to plastic strain. The criterion in Eq.5-12 implies that the matrix requires a higher minimum strain-hardening rate to resist the onset of fracture when the material contains more voids and/or is subjected to a higher triaxial stressing. Using the Bridgman correction to calculate the variation of stress-state σ_h/σ with ε_p during tensile necking, and fitting the parameter k to the measured fracture strain of the stable austenite, this gives the $(h/\sigma)_c$ curve in Fig.5-41. When h/σ drops below $(h/\sigma)_c$, the material fails because of shear localization. As can be seen in Fig.5-41, the fracture strain of 31Ni(L) alloy at θ=0.6 was improved from point b to point b' due to the strain-induced transformation.

c. Predicted Uniform Strain and Fracture Strain

The normalized strain-hardening rate vs. true plastic strain curves at temperatures from 65 to 250°C were calculated for the 0.5Mn-0 alloy from Eqs.5-8, 9, 12, and the fitted kinetic data. After necking, the influence of triaxiality on the transformation kinetics was also taken into account through the β coefficient in Eq.5-5. According to the distribution curve of triaxiality along the specimen axis numerically calculated by Argon and Needleman [90], the region within about $0.3a_i$ away from the plane of the minimum cross-section maintains at a nearly constant triaxiality, where a_i is the minimum radius of the neck. This means the correction of kinetics due to triaxiality change is valid for an appreciable volume of material adjacent to the position with minimum cross-section, where fracture takes place. The consideration of triaxiality dramatically alters the shape of the transformation curve and the martensite volume fraction, as demonstrated in Fig.5-42, and also the shape of h/σ curve. The h/σ curves at 100 to 250°C together with the $(h/\sigma)_c$ curve are summarized in Fig.5-43. In this

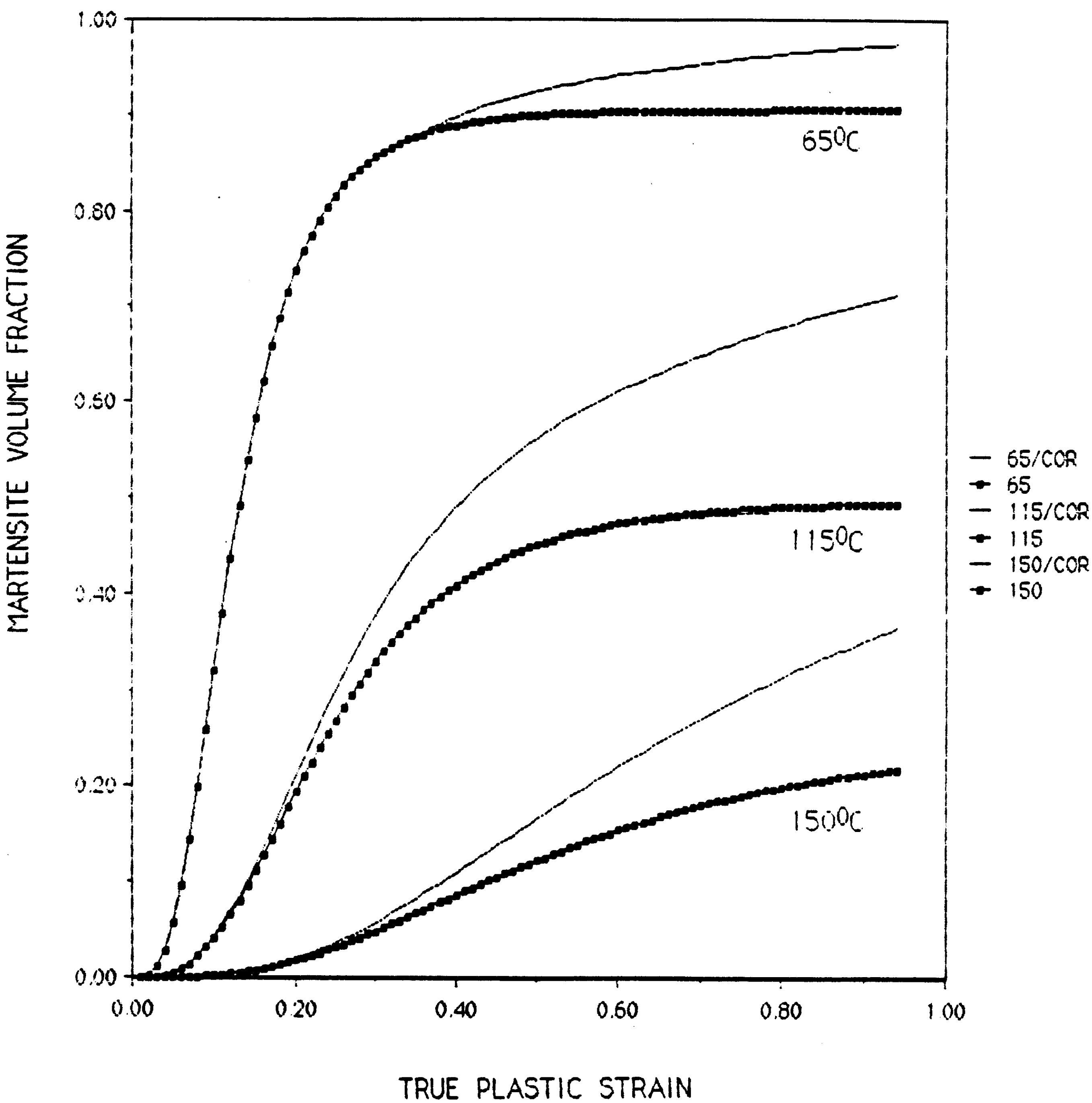

Fig. 5-42 The increment of triaxiality due to tensile necking causes faster transformation rate and hence more martensite in the 0.5Mn-0 alloy, as demonstrated from the comparisions of the light (with correction) and the heavy transformation curves (without correction) at 65, 115, and 150°C.

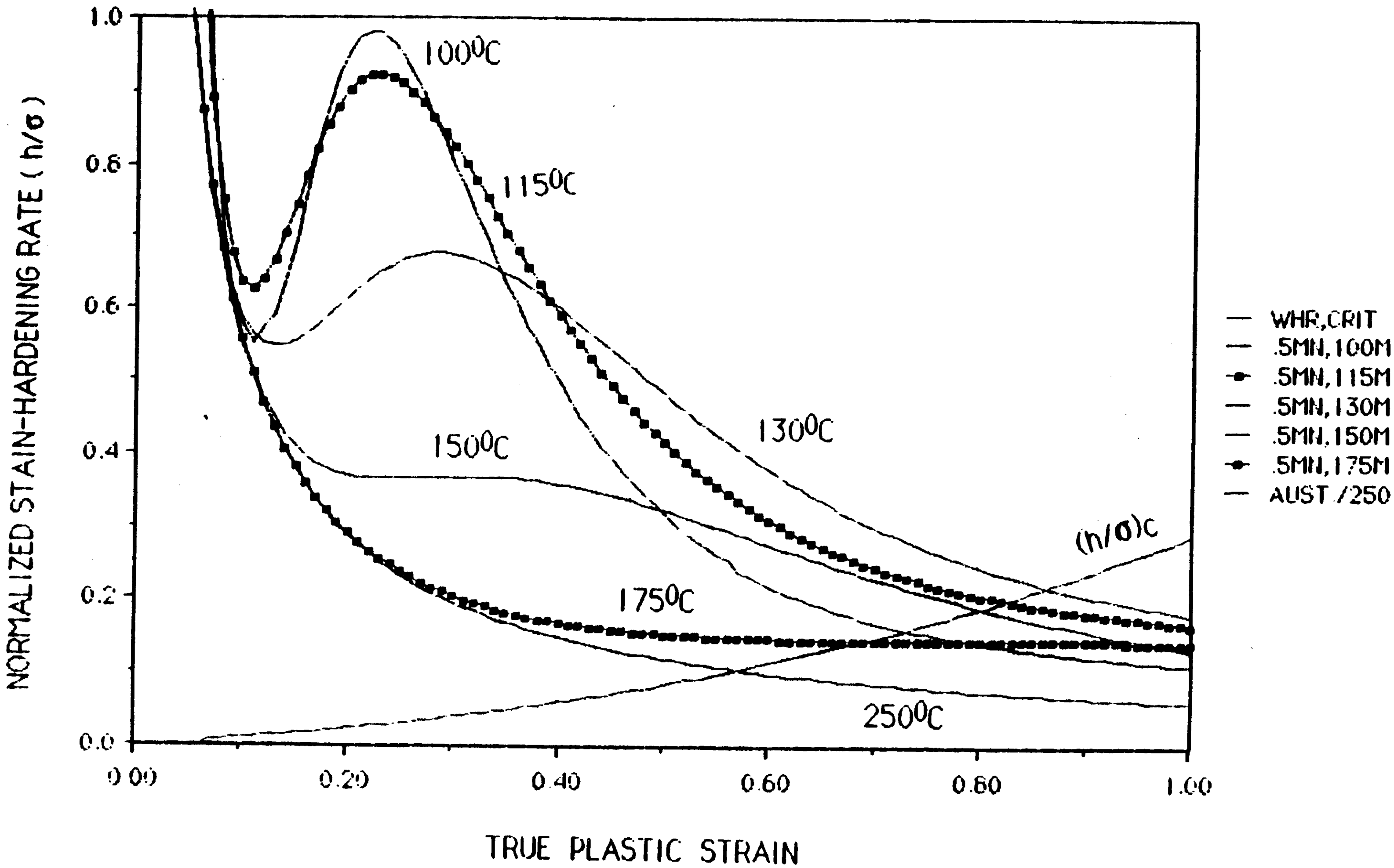

Fig. 5-43 Calculated values of the normalized strain-hardening rate for the 0.5Mn-0 alloy at temperatures from 100 to 250^{0}C. The fracture strain is defined as the intersection of each h/σ curve and the $(h/\sigma)_C$ curve fitted to the observed fracture strain of the austenite.

temperature range, the uniform strains keep closely to that of the parent phase, but the fracture strains do not. The enhancement of fracture strain is controlled by the shape of the h/σ curve rather than by the relative magnitude of h/σ. The maximum ε_{pf} is found at 130°C corresponding to the best transformation rate in the neck. At lower temperatures, h/σ can reach a higher value at low strains but decreases at a faster rate, and thus the alloy fails at lower ε_{pf}. A lower ε_{pf} is obtained at temperatures above 130°C, but it simply arises from insufficient h/σ associated with a very slow transformation rate.

The calculated values of ε_{pu} and ε_{pf} for the 0.5Mn-0 alloy are compared with the measured values in Fig.5-44. The predicted peak ε_{pu} is lower than the measured one and occurs at higher temperature by 15°C due to the small local mismatch between the fitted and the observed kinetic curves as mentioned before, but both curves of ε_{pu} basically reveal the same shape. The currently refined kinetic model [84] for the strain-induced transformation may improve this inconsistency.

For the fracture strain, the predicted values are in surprisingly good agreement with the experimental data even though the applied fracture criterion is not as well-defined as the necking condition. Considering that the coefficient k is determined by fitting to the observed ε_{pf} of stable austenite, this fracture criterion should actually be ragarded as a mathematical model. Nevertheless, the calculation does demonstrate one way in which the strain-induced martensitic transformation can delay the occurrence of failure caused by void-softening.

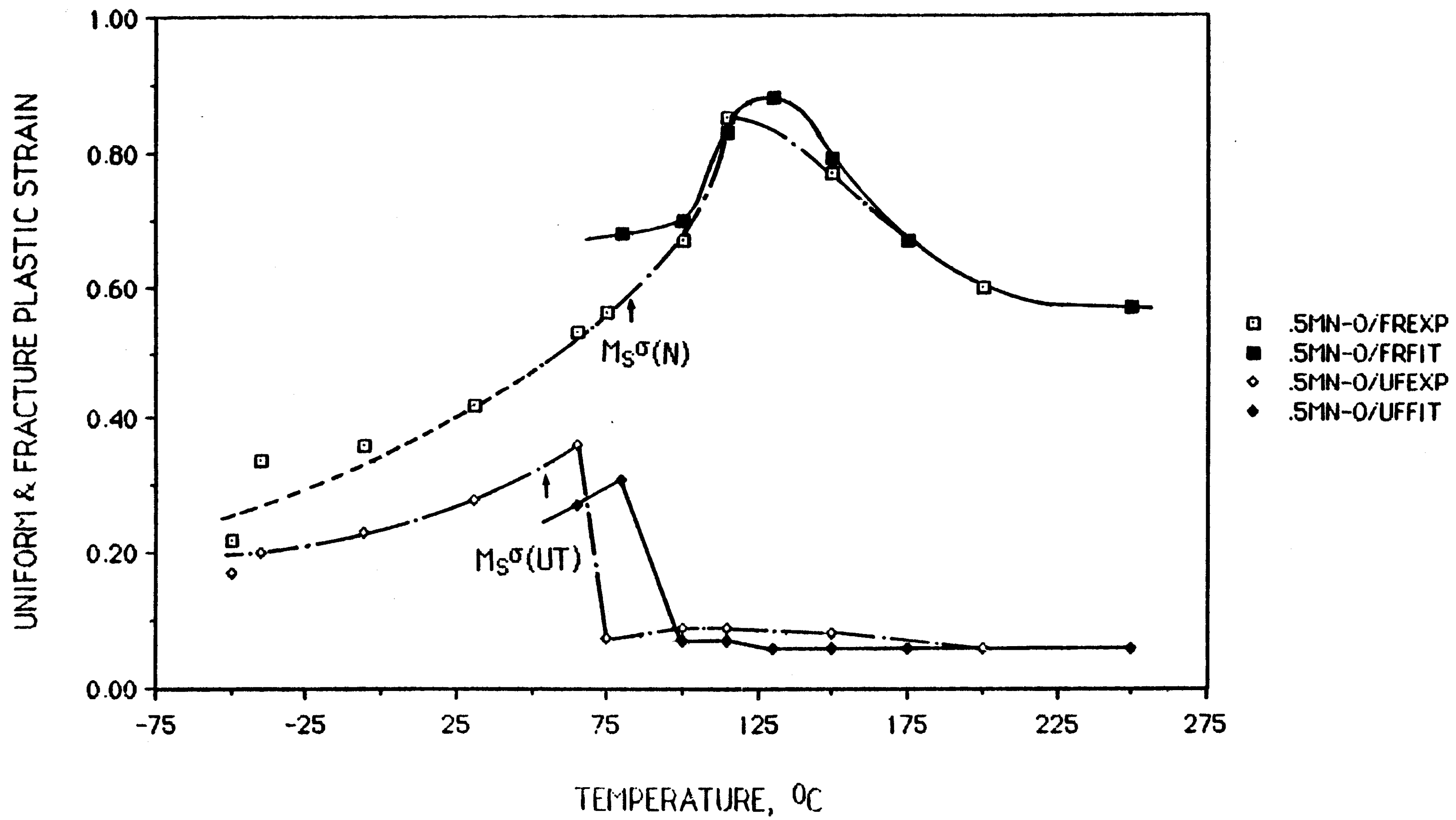

Fig. 5-44 Comparison of the predicted (solid points) and the observed (open points) uniform strains and fracture strains at various temperatures for the 0.5Mn-0 alloy.

Thus far, the effect of dilatation has not been explicitly treated in our calculations. In the case of fracture-strain prediction, the main contribution of dilatation has been taken into account through the stress-state sensitivity of the transformation kinetics. The high strain-hardening rate associated with transformation can slow down the radial growth rate of a neck and force its longitudinal propagation. The neck, thus, becomes less sharply localized as can be seen by comparing the neck contours of the 0.5Mn-0 alloy fractured at 115 and 250°C in Fig.5-45. The triaxiality at the fracture surface of the 0.5Mn-0 alloy at 115°C was reduced by only 13% according to a numerical calculation [78] in which the dilatation effect was neglected. A small further decrease of triaxiality is expected if the stress-state sensitivity of transformation kinetics is considered. Two opposing effects will be caused by the delocalization in the neck on the assessment of fracture strain : first, $(h/\sigma)_c$ is reduced because of the decrease of σ_h/σ; on the other hand, h/σ is also reduced since the extra strain-hardening due to the stress-state dependence of transformation becomes less. The net effect is difficult to estimate, but will not significantly change the predicted fracture strains.

d. Microstructural Evidence of Transformation in Delaying Void Formation

The analysis of tensile fracture was accomplished in a simplified way from a macroscopic view in the present work. Even for a non-transforming material, a quantitative correlation between the apparent properties (elongation or toughness) and the micromechanisms of ductile fracture is still undergoing development. The benefit of the deformation-induced martensitic transformation showing up in the increments of fracture strain

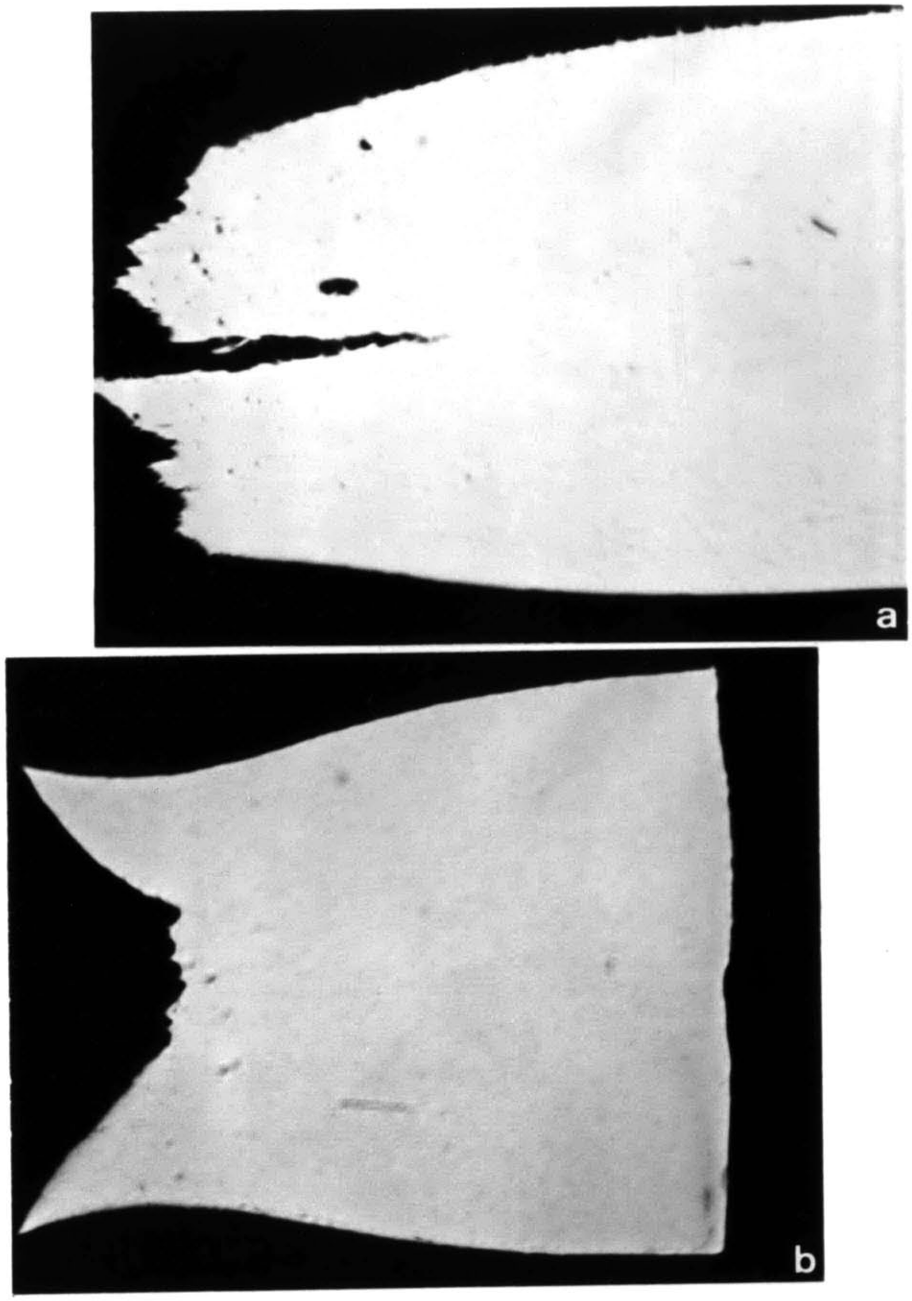

Fig. 5-45 The contour of the tensile neck becomes less localized due to the deformation-induced martensitic transformation. (a). 0.5Mn-0 alloy at 115°C, (b). 0.5Mn-0 alloy at 250°C.

and toughness certainly comes from delaying the microscopic processes of ductile fracture, as illustrated by the microstructure of the tensile-deformed 0.5Mn-0 alloy in the following. TEM micrographs of a foil with low martensite content (f_{α}'=0.029 by ε_{pu}=0.09 at 115ºC) in Fig.5-46 shows that the martensite phase preferentially formed in the local high-triaxiality region surrounding an alumina particle. This indicates that the void nucleation will not occur until a higher strain (or stress) because deformation by slip is more difficult to operate in the stronger martensite; and more important, the volume expansion associated with the martensitic transformation is able to accommodate the strain differentials between the matrix and the particle caused by the remoted stress and consequently reduce the normal stress (or local triaxiality) encountered at the interfaces. The low contrast image displayed by the crystalline alumina particle corresponds to a very low density of defects within it and so the underforming assumption is reasonable.

Tracey [40] has reported that interaction between voids can accelerate the void-growth rate, and likewise the nucleation rate possiblly. Some important information concerning this topic may be shown in Fig.5-47, which was taken from a foil cut longitudinally from the tensile neck with ε_p = 0.40 to 0.50 (f_{α}' ~ 0.15) at 150ºC. Directional martensitic laths formed around particles. In the region between two particles (one of them is cut by the upper side of the micrograph), a "coarser" lath is found to grow from one particle to the other. It is believed that this arrangement of martensitic laths is related to the direction of remote stress and is also influenced by the interaction of plastic flows around the two particles. At least, Fig.5-47 indicates that the growth of martensite may follow a specific way to minimize the factors promoting void formation.

Further information on the void formation can be obtained from Fig.5-48. The foil was prepared from the transverse cross-section of the uniformly elongated portion (ε_p = 0.36) tested at 65°C, and contained about 75% martensite in volume. Examining the dark-field image formed by a martensite diffraction spot, a small pore is found at the interface between the matrix and a sharp corner of the particle, as indicated by four arrows at its edge. In the TEM dark-field image, the pores correspond to the darkest region of a micrograph because absolutely no electrons can be reflected from them. Now, a question, whether that pore is formed by deformation or electropolishing, has to be answered. The former may be the right answer in this case. The electrolyte and the thinning conditions (voltage, current, and temperature) for the 0.5Mn-0 alloy has been carefully selected and tested. It did not attack the alumina/matrix interfaces too preferentially even at sharp coners of particles, as demonstrated by the well-bonded interfaces in Fig.5-46 and 5-47, although the skinning effect of electric current may introduce higher current density and hence a higher thinning rate around a sharper corner. The earlier formation of voids for the 0.5Mn-0 alloy at 65°C results from the exhaustion of austenite in the region adjacent to the particle and is consistent with the lower observed fracture strain.

The above microstructural observations illustrate that the strain-induced transformation with an appropriate rate can effectively delay the void formation, and so void nucleation seems to play a more important role in promoting the ductile fracture of these RSP alloys than void growth.

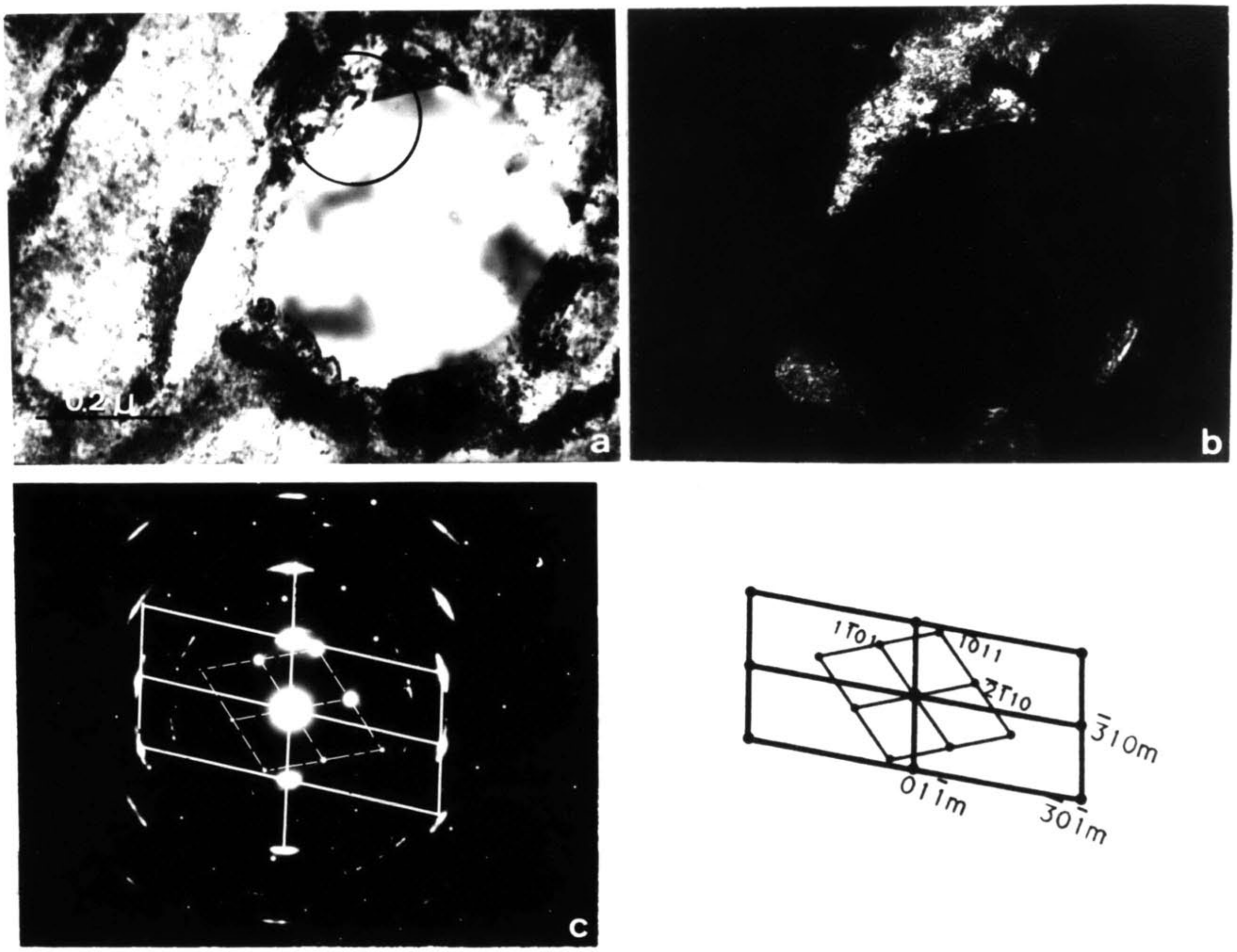

Fig. 5-46 TEM micrographs show the preferential formation of martensite around an alumina particle in the deformed 0.5Mn-0 alloy with 3% martensite (ε_p=0.09, at 115°C). a).Bright-field image, b). Dark-field image from the diffraction spot (0$\bar{1}$1) of martensite, c). Seleacted-area diffraction patterm from the circled region in a), and d). Analysis of diffraction pattern showing $[133]_{\alpha'}//[01\bar{1}1]_{\alpha\text{-}Al_2O_3}$.

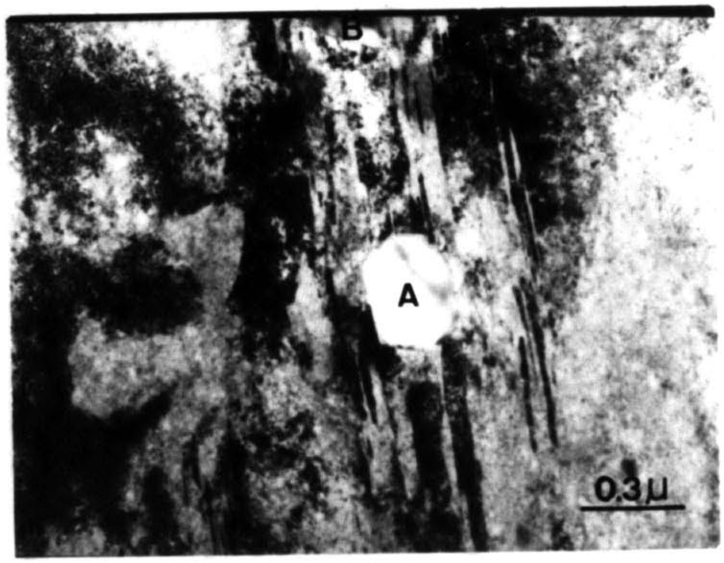

Fig. 5-47 Directional lath martensite formed between two alumina particles A and B. The foil with about 0.15 martensite volume fraction was cut from a tensile neck of the 0.5Mn-0 alloy tested at 150ºC along the loading axis.

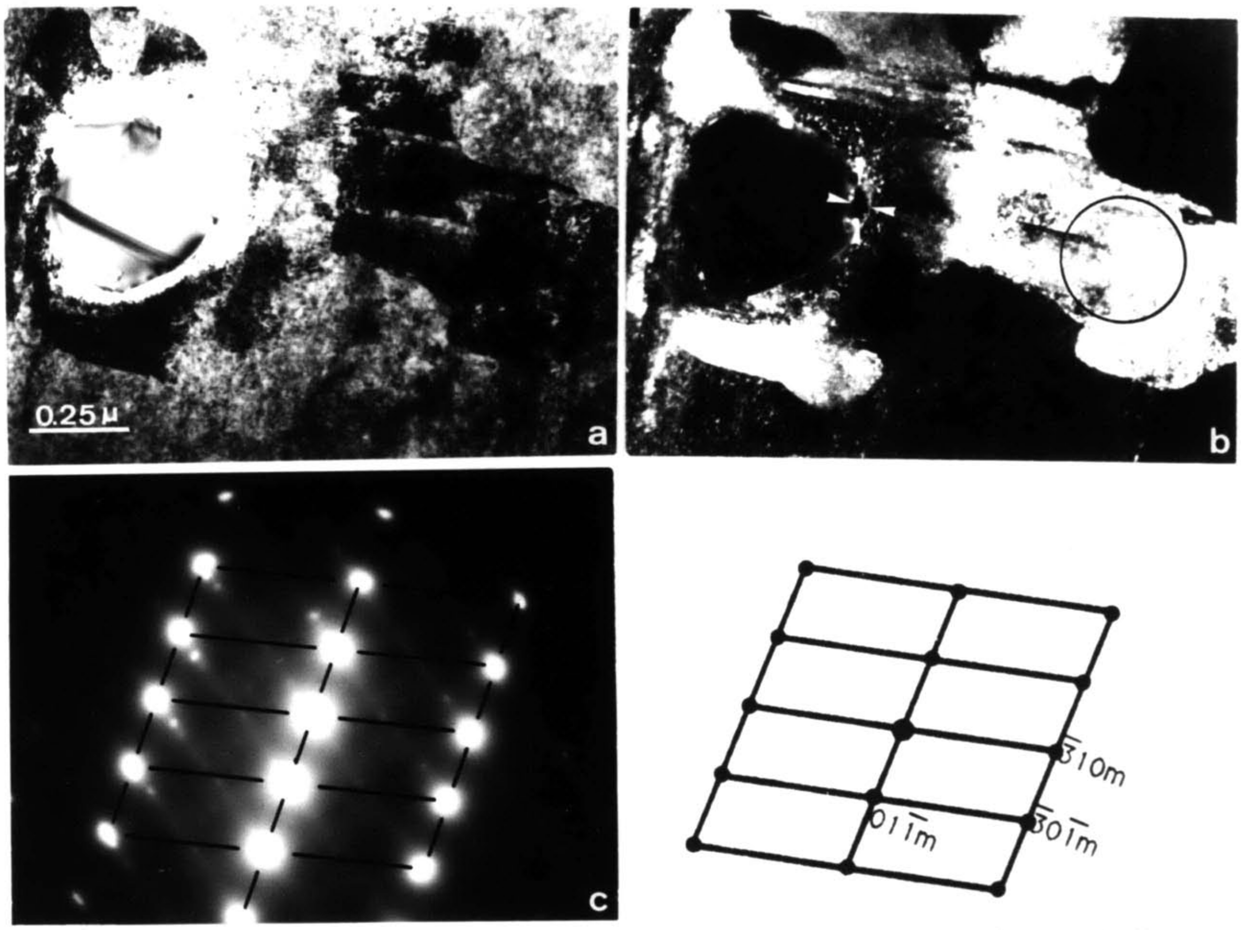

Fig.5-48 A pore, indicated by four arrows surrounding it, was found at the interface between the matrix and the sharp corner of the particle. The foil was cut from the deformed 0.5Mn-0 alloy at 65°C normal to the loading axis with 0.75 martensite volume fraction (ε_p=0.36). a). Bright-field image, b). Dark-field image from martensite diffraction spot ($01\bar{1}$), c). and d). are the diffraction pattern of the circled region in b). and the indexing, $[113]_{\alpha'}$

5-3-4 The Roles of Strength Difference and Dilatation in Transformation Toughening

Ductility enhancement associated with the strain-induced martensitic transformation in the 0.5Mn-0 alloy has been predicted as a result of retarding the occurrence of void-softening-induced shear localization due to both the extra strain-hardening rate and dilatation. The TEM observations suggest that the void formation can be suppressed by forming martensitic laths preferentially at the interfaces of alumina particles, which are the typical void-nucleation sites. A concept similar to that used in the prediction of fracture strain could be also applied for calculating the critical J or COD values at crack initiation in a transforming material. However, a complex transformation configuration is expected since both the stress and strain fields are functions of position and crack-tip geometry. All of these factors would not be known without employing sophisticated numerical methods, and are currently being studied [78]. In this section, we will place emphasis on exploring how the hardness difference (ΔH_V) between the α' and γ phases and the transformation volume change ($\Delta V/V_\gamma$) influence the toughness from the experimental standpoint.

In the temperature range from M_s^σ(CT) to M_d(CT), the most accessible transformation parameter around a crack-tip is the height of the transformation zone instead of the volume fraction of martensite because of the fine lath morphology. After the three-point bend test, the specimen was firmly bonded to a flat metal surface by ultilizing a glue for metal-metal adhesion, then ground, polished and etched to show the contour of the crack-tip. A surface layer at least 2mm in thickness was removed to ensure that the material on the observed plane had been under plane-strain condition during test. In order to correlate the observed J_{IC} increments, the zone height (H) was measured at a very early stage of crack advance, as demonstrated in Fig.5-49 for the 3.5Mn-U alloy tested at 0ºC : 1). The boundary of the transformation zone is defined as the farthest position away from the crack at which the martensite laths still can be found, and is shown by the dashed curves on the lightly etched surface in Fig.5-49. 2). The COD value (δ_i) corresponding to the J_{IC} is calculated by using $\delta_i = J_{IC}/1.6\sigma_y$, which equals 75µm for the 3.5Mn-U alloy at 0ºC. 3). The initial crack tip position, indicated as line a-a' in Fig.5-49, can be determined because no martensite exists beyond this point. 4). The zone height is measured at a distance of $2\delta_i$ away from line a-a' and is indicated by the summation of segments b-b' and c-c' in Fig.5-49. The measurement is selected at $2\delta_i$ partly because the variation of zone height with crack extension beyond $2\delta_i$ becomes less. Furthermore, the relative difference between ΔJ_{IC} and ΔJ_I (= $J_I - \Delta J_{I,aust.}$) at crack extension $2\delta_i$ is less than 1%. Table 5-7 summarizes all the measurements and the related parameters for two groups of alloys with low ΔH_v and high ΔH_v according to the classification in Section 3-4.

Before comparing the contributions of ΔH_v and $\Delta V/V_\gamma$ on the toughness enhancement, the half-height of the transformation zone is plotted vs. a nondimensional temperature scale θ (=[T-M_s^σ(CT)]/[M_d(CT)-M_s^σ(CT)]), which is used to correct the austenite stability arising from the difference of chemical compositions at a given triaxiality, in Fig.5-50. With θ increasing or austenite becoming more stable, H/2 monotonically decreases for all alloys. There is no consistent evidence to indicate that ΔH_v and $\Delta V/V_\gamma$ strongly affect the zone height. A similar conclusion may also be drawn for

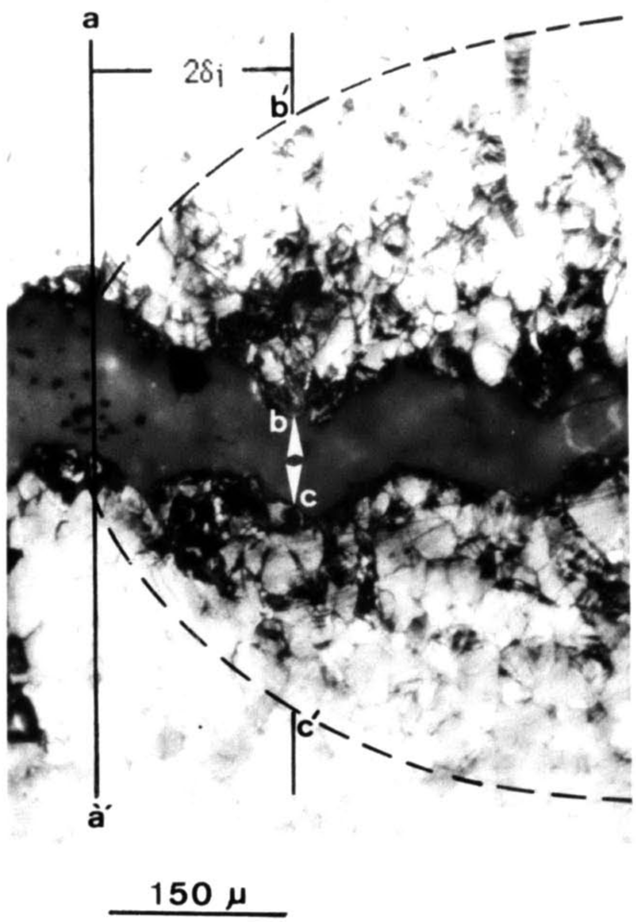

Fig.5-49. Optical micrograph illustrating the measurement of transformation-zone height. 3.5Mn-U alloy, bend tested at 0°C.

Table 5-7 Half-Height of Transformation Zone

Alloys	H/2 (μm)	J/ΔJ (KJ/m^2)	θ	(H/2)/J
0.5Mn-0	210	179/120	-0.05	1.17
0.5Mn-0	180	162/105	0.18	1.11
0.5Mn-0	50	93/25	0.43	0.54
0.5Mn-0	20	85/8	0.74	0.24
31Ni-5Cr	200	306/100	0.12	0.65
31Ni-5Cr	100	249/45	0.43	0.40
31Ni-5Cr	25	206/20	0.63	0.12
31Ni	200	206/48	0.05	0.97
31Ni-9Co	100	118/19	0.40	0.85
3.5Mn-U	245	151/100	-0.07	1.65
3.5Mn-U	220	136/88	0.15	1.62
3.5Mn-U	20	52/5	0.76	0.38
0.5Mn-U	70	179/110	0.5	0.39
0.5Mn-U	40	140/72	0.71	0.29

*θ is the nondimensional temperature.

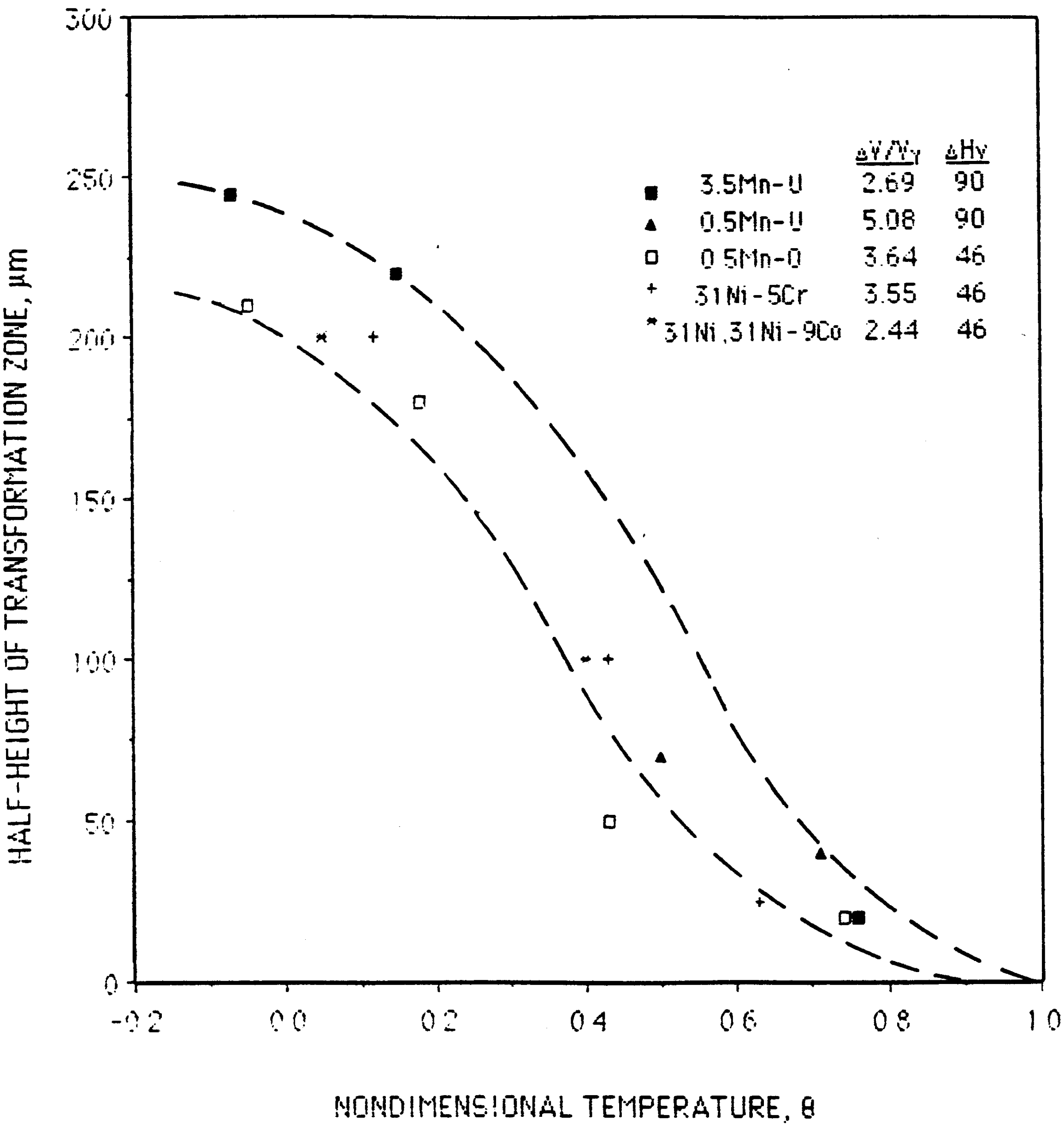

Fig. 5-50 Half-height of transformation zone vs. nondimensional temperature.

the average martensite volume fraction ($f_{\alpha'}$) in the transformation zone. Therefore, both H/2 and $f_{\alpha'}$ seem to depend on the austenite stability only and can be expressed as functions of θ as $H(\theta)$ and $f_{\alpha'}(\theta)$, respectively.

The half-height of the transformation zone is plotted vs. the increment of J_I at $2\delta_i$ due to transformation in Fig.5-51(a) and (b) for the phosphocarbide- and γ'-strengthened steels. For each alloy, the ΔJ_I vs. H/2 curve can be approximately represented by a line passing through the origin, but with a slope (S) depending on the values of ΔH_V and $\Delta V/V_\gamma$, as depicted in Fig.5-52. Assuming that the effects of ΔH_V and $\Delta V/V_\gamma$ on the toughness enhancement are independent, the slopes are represented by an equation :

$$\begin{aligned} S &= S_{\Delta H_V} + S_{\Delta V/V_\gamma} \\ &= A \quad + B \cdot (\Delta V/V_\gamma)^N \end{aligned} \tag{5-13}$$

where A is a function of ΔH_V, and the coefficients B and N are constants. Fitting all values of slopes to Eq.5-16, two expressions are obtained :

$$\text{Low-}\Delta H_V \text{ alloys---} S = 0.0989 + 7.48 \cdot 10^{-3} \cdot (\Delta V/V_\gamma)^{3.2} \tag{5-14}$$

$$\text{High-}\Delta H_V \text{ alloys---} S = 0.243 \quad + 7.48 \cdot 10^{-3} \cdot (\Delta V/V_\gamma)^{3.2} \tag{5-15}$$

Eqs.5-14 and 15 are shown by the solid lines in Fig.5-52. From Fig.5-51 and Eq.5-13, ΔJ_I is linearly related to the product of $H(\theta)$ and S. The average martensite volume fraction may also influence ΔJ_I. Since no experimental results are available at present, a multiplying factor, $F_{\alpha'}$, is assumed to account for the latter effect. $F_{\alpha'}$ is a function of θ through $f_{\alpha'}$. Thus, ΔJ_I can be written as :

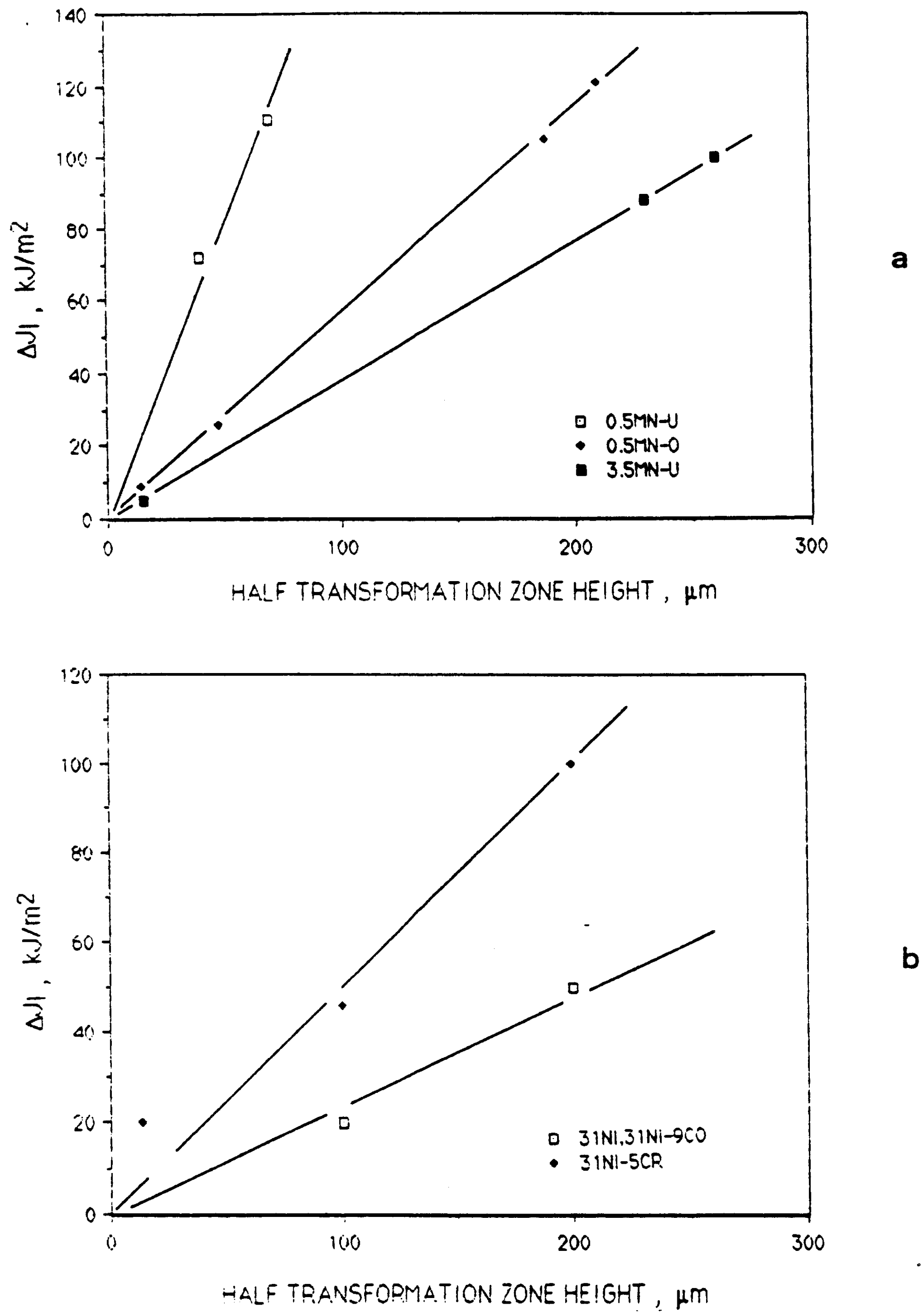

Fig. 5-51. Half-height of transformation zone vs. J_I increment corresponding to a very small crack extension ($=2J_{IC}/1.6\sigma_y$). a). phosphocarbide-strengthened steels, b). γ'-strengthened steels.

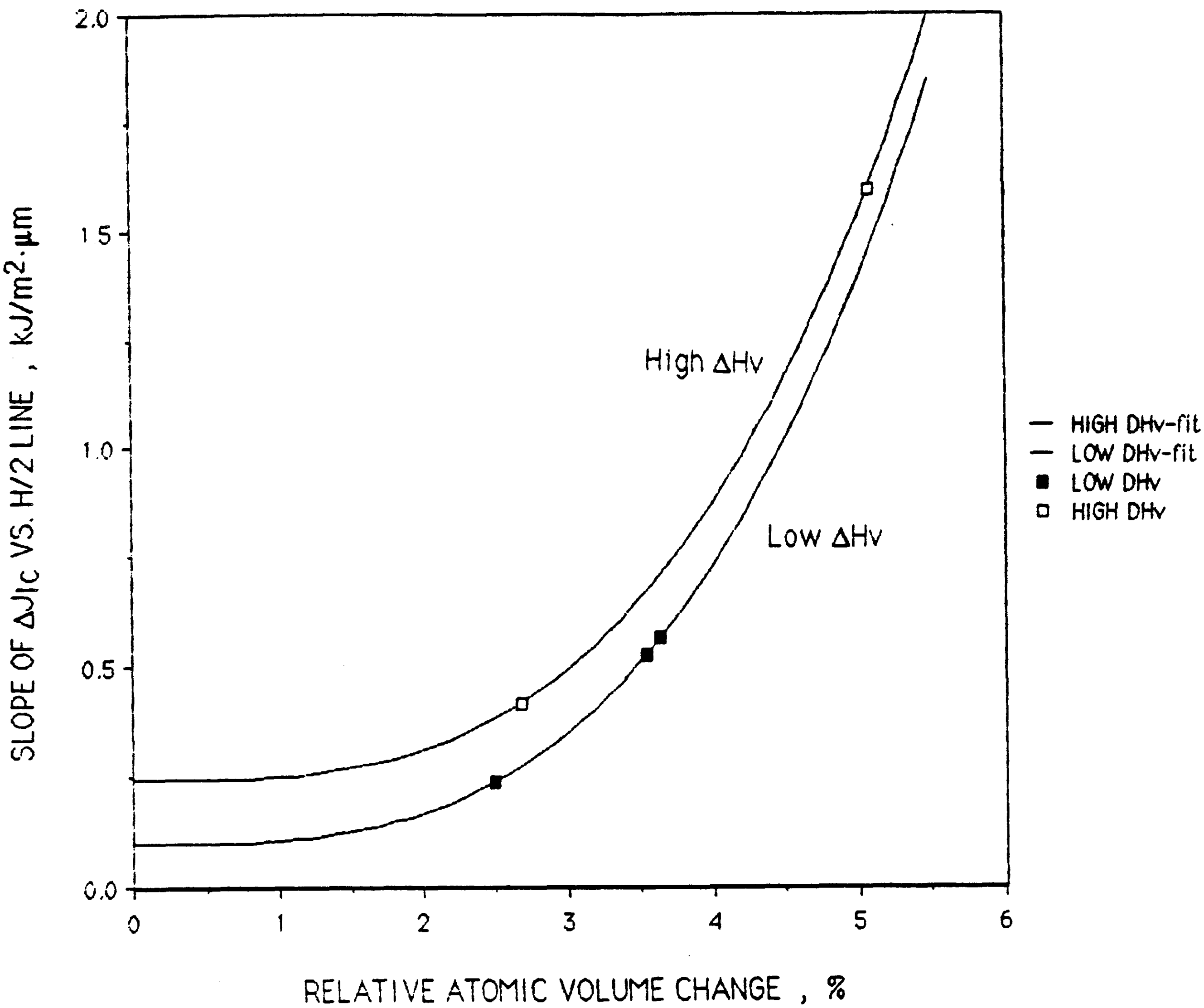

Fig. 5-52 Slopes of half-height of transformation zone vs. J_I increment lines are plotted transformation volume change for both high- and low-Δ'Hv alloys, and then fitted to power equations as shown by solid lines.

$$\Delta J_I = F_\alpha'(\theta) \cdot H(\theta) \cdot [S_{\Delta Hv} + S_{\Delta V/V_\gamma}]$$
$$= \Delta J_{I,\Delta Hv} + \Delta J_{I,\Delta V/V_\gamma}$$

This gives :

$$(\Delta J_{I,\Delta V/V_\gamma})/(\Delta J_{I,\Delta Hv}) = (S_{\Delta V/V_\gamma})/(S_{\Delta Hv})$$
$$= 0.076 \cdot (\Delta V/V_\gamma)^{3.2} \quad \text{--Low-}\Delta H_V \text{ alloys} \qquad (5\text{-}16)$$
$$= 0.031 \cdot (\Delta V/V_\gamma)^{3.2} \quad \text{--High-}\Delta H_V \text{ alloys} \qquad (5\text{-}17)$$

where $\Delta J_{I,\Delta V/V_\gamma}$ and $\Delta J_{I,\Delta Hv}$ are the toughness increments from the dilatation and hardness difference. Using Eqs.5-16 and 17, the ratios of $\Delta J_{I,\Delta V/V_\gamma}$ and $\Delta J_{I,\Delta Hv}$ to ΔJ_I are listed in Table 5-8 for the low-ΔH_V and high-ΔH_V alloys.

The hardness difference can be essential in transformation toughening for a low-dilatant alloy and vice versa. The two high-ΔH_V alloys, 3.5Mn-U and 0.5Mn-U, represent an extreme case. Only 42% Of the total toughness enhancement results from the transformation volume change for the former alloy, while 85% for the later. From the observed peak ΔJ_{Ic} (=100KJ/m^2) of the 3.5Mn-U alloy at -25°C, $\Delta J_{Ic,\Delta Hv}$ is found to be 55KJ/m^2. Because of the same hardness difference, the $\Delta J_{Ic,\Delta Hv}$ value of the 0.5Mn-U alloy at the corresponding θ is also equal to 55KJ/m^2. Using this value and the ratio of $\Delta J_{I,\Delta Hv}$ to ΔJ_I in Table 5-8, the highest J_{Ic} of the 0.5Mn-U alloy would be expected to reach 380KJ/m^2 at about 75°C if the intergranular fracture did not intervene in the failure of this alloy.

Table 5-8 Contributions of Hardness Difference and Dilatation to Toughness Enhancement

	Low-ΔH_V Alloys			High-ΔH_V Alloys	
	31Ni,31Ni-9Co	31Ni-5Cr	0.5Mn-0	0.5Mn-U	3.5Mn-U
$\Delta V/V_{\gamma}$, %	2.44	3.55	3.64	2.69	5.08
$\Delta J_{I,\Delta Hv}/\Delta J_I$	0.43	0.19	0.17	0.58	0.15
$\Delta J_{I,\Delta V/V_{\gamma}}/\Delta J_I$	0.57	0.81	0.83	0.42	0.85

In the last section, dilatation was also involved in prediction of fracture strain for the 0.5Mn-0 alloy by considering the decrease of austenite stability after necking. The fracture strain was predicted to be 0.87 at 130°C with this consideration, while it decreased to 0.79 by neglecting the effect of dilatation. Comparing with the fracture strain of the austenite, 0.60 at 150°C, dilatation and hardness difference contribute to the fracture strain increments by 0.08 and 0.19, or 30% and 70%, respectively. On the other hand, 83% of fracture toughness enhancement arises from dilatation and 17% from hardness difference in the 0.5Mn-0 alloy, referring to Table 5-8. The analysis suggests that dilatation plays a more important role when the material is subjected to high triaxiality in the sharp crack-tip and may possiblly explain the higher relative enhancement of fracture toughness than that of fracture strain ($\Delta J_{Ic,max.}/J_{Ic,aust.}$=2 vs. $\Delta\varepsilon_{pf,max.}/\varepsilon_{pf,aust.}$=0.45). At present, the benificial effects of deformation-induced martensitic transformation can be only interpretated as a consequence of retarding the void nucleation and growth processes. The stronger martensitic phase makes the deformation by slip more difficult, while the dilatation associated with transformation can reduce the normal stress and hence the local triaxiality at the interface of inclusion particle. The toughness increments arising from strength difference and dilatation may be possiblly analyzed through a continuum-mechanics modeling by coupling the measured transformation kinetics and flow relations with an appropriate ductile fracture criterion.

Chapter 6. Conclusions

1. Rapid solidification processing is shown to be successful in forming high-phosphorus steels with phosphorus incorporated in the carbides; the latter then precipitate uniformly instead of preferentially at austenitic grain boundaries. These coherent fine (< 80Å) phosphocarbide particles, $(Cr,Fe,P)_{23}C_6$, effectively strengthen the carbon-containing austenitic steels, and the yield stress can achieve the desired 1250 Mpa (180 ksi) at room temperature. However, a warm-rolling operation is required to eliminate the embrittling effect of helium-gas contamination introduced during the rapid solidification process.

2. Although these new phosphocarbide-strengthened austenitic steels show considerable temperature dependence of properties due to deformation-induced transformation, the temperature range corresponding to the best combination of strength and toughness can be controlled by changing the stability of the matrix through aging treatments.

3. The stronger tendency toward brittle intergranular fracture shown by underaging is considered to result from the higher phosphorus content still remaining in the matrix, and then the advantage of deformation-induced martensitic transformation cannot be fully utilized. Despite such effects, the transformation can increase J_{Ic} by 100~120 KJ/m^2 for both the underaged and overaged alloys.

4. In addition to experimental measurements, the M_s^σ temperatures under various stress-states are predicted from calculation of the effect of stress

on the isothermal martensitic transformation. A relatively large inconsistency between the observed and predicted values of M_s^σ is found, possibIly because of using a constant mechanical driving force in the calculations.

5. The transformation kinetics at temperatures from -196 to 150°C have been measured in uniaxial tension and compression. In the strain-induced regime, the overall shape of the transformation curves is fitted well by the Olson-Cohen model, in which the β parameter is expressed as a function of stress-state to account for the sensitivity of austenite stability to triaxiality due to dilatation in the transformation.

6. A quantitative assessment of ductility in the overaged 0.5Mn alloy was accomplished by calculating the influence of strain-induced transformation on the strain-hardening rates and applying suitable criteria. The predicted temperature dependence of uniform and fracture strains is in good agreement with the observations. As clearly demonstrated by the analysis, the extra high strain-hardening rate in the transforming alloy can delay the onset of flow instability and void-induced ductile fracture, thus enhancing the uniform and fracture strains. The magnitude of enhancement depends on the variation of strain-hardening rate with strain, which is mainly controlled by the transformation kinetics. Compared to the effect of dilatation, the strength difference provides the major part of ductility enhancement under the moderate triaxiality encountered in the tensile test.

7. Microstructural observation in the tensile-deformed 0.5Mn overaged alloy shows that void formation can be inhibited even after severe deformation by

forming fine martensitic laths preferentially at the interfaces of alumina particles. This further confirms the beneficial effect of deformation-induced martensitic transformation in retarding the microscopic processes of ductile fracture.

8. The enhancement of fracture toughness is found to be proportional to the third power of the transformation volume change according to measurements of transformation zone height. Both dilatation and hardness difference may be important in transformation toughening. For instance, the hardness difference supplies 58% of the toughness increment for the high-ΔH_V, low-$\Delta V/V_\gamma$ 0.5Mn overaged alloy, whereas only 15% for the high-ΔH_V, high-$\Delta V/V_\gamma$ 3.5Mn underaged alloy. However, dilatation becomes more important as the triaxiality increases for a given alloy. In the 0.5Mn overaged alloy, the dilatation contributes only 30% of the tensile fracture-strain enhancement, but 83% of the toughness increment. Based on this analysis, the potentially highest ΔJ_{Ic} of the 0.5Mn-U alloy is expected to reach 325 KJ/m^2 if not circumvented by intergranular fracture.

Chapter 7. Recomendations for Future Research

1). Measurements of phosphorus segregation at grain boundaries after various aging conditions by using STEM microanalysis in the thin-foil specimen or AES technique at the intergranular fracture surface are required to explain the stronger tendency towards intergranular fracture shown by underaging. The relationships between aging, phosphorus content at grain boundary, and intergranular fracture can be employed to determine the optimum aging condition by which the alloy exhibits the best toughness enhancement and avoids the interference of intergranular fracture above M_s^σ(CT). For instance, the optimum aging treatment of the 0.5Mn alloy should lie between the underaged and overaged conditions used in this work.

2). Because of the outstanding precipitation-hardening ability, it is still worth to study the transformation toughening behavior of the solution and aging treated alloy (without any warm-working), in case a gas-free alloy can be obtained. A conventional argon-atomization technique may be more approprite to avoid the mechanical entrapment of the atomizing gas than the Pratt and Whitney process [59]. The influence of C/P ratio on the strengthening and transformation toughening phenomena is also an interesting topics.

3). The triaxiality sensitivity of the M_s^σ temperature in the stress-state range of that corresponding to uniaxial tension and a crack-tip can be further investigated with plane-strain and circumferentially-notched tensile specimens.

4). The effect of transformation amount on toughness enhancement in the strain-induced temperature regime can be studied by loading the three-point bend specimen until a small crack extension (such as 2 times COD) is found. Thin slices could then be cut parallel to the crack advance direction for measurement of martensite volume fraction using the magnetization technique.

References

1. Leal, R. H., "Transformation Toughening of Metastable Austenitic Steels.", Ph. D. Thesis, M.I.T., 1984.
2. Banerjee, B. R., Dulis, E. J., and Hauser, J. J., "Role of Phosphorus in $M_{23}C_6$ Precipitation in an Austenitic Stainless Steel.", Trans. ASM, Vol.61, 1968, pp.103.
3. Olson. G.B. and Cohen, M., "A Mechanism for the Strain-Induced Nucleation of Martensitic Transformations", J. of Less-Common Metals, Vol. 28, 1972, pp.107.
4. Richman, R. H., and Bolling, G. F., "Stress, Deformation and Martensitic Transformation", Met. Trans. Vol. 2, 1971, pp. 2451.
5. Olson, G. B., and Azrin, M., "Transformation Behavior of TRIP Steels", Met. Trans., Vol. 9A, 1978, pp. 713.
6. Maxwell, P. C., Goldberg, A., and Shyne, J. C., "Stress-Assisted and Strain-Induced Martensite in Fe-Ni-C Alloys", Met. Trans., 1974, Vol. 5, pp.1319.
7. Olson, G. B." Transformation Plasticety and the Stability of Plastic Flow", in "Deformation, Processing, and Structure" ASM Material Science Seminar, 1982.
8. Zackay, V. F., Parker, E. R., Fahr, D., and Busch, R., "The Enhancement of Ductility in High-Strength Steels", Trans. ASM, Vol. 60, 1967, pp.223.
9. Chanani, G. R., Zackay, V. F., and Parker, E. R., " Tensile Properties of 0.05 to 0.20 Pct TRIP Steels", Met. Trans. Vol. 2, 1971, pp.133.
10. Tamura, I., Maki, T., and Hato, H., " On the Morphology of Strain-Induced Martensite and the Transformation-Induced Plasticity in Fe-Ni and Fe-Cr-Ni alloys", J. japan Inst. Metals, Vol. 33, 1969, pp.1376.
11. Fahr, D. " Stress- and Strain-Induced Formation of Martensite and its Effect on Strength and Ductility of Metastable Austenitic Stainless steels", Met. Trans. Vol. 2, 1971, pp.1883.
12. Azrin, M., Olson, G. B., and Gagne R. A., " Warm Extrusion of TRIP Steels : Process Control and Tensile Properties", Material Sci. Eng. vol. 40, 1979, pp. 175.
13. Tamura, I., Maki, T., Hato, H., and Okada M., "Strength and Ductility of Austenitic Steels Accompanying Strain-Induced Martensite", in Pro. Second Conf. on the Strength of Metals and Alloys, Asilomar, CA, 1970, pp.900.

14. Bhandarkar, D, Zackay, V. F., and Parker, E. R., " Stability and Mechanical Properties of Some Metastable Auetenitic Steels", Met. Trans., Vol. 3, 1972, pp.2619.
15. Gerberich, W. W., Hemmings, P. L., Merz, M. D., and Zackay, V. F., "Preliminary Toughness Results on TRIP Steel", Trans. Am. Soc. Metals, Vol. 61, 1968, pp. 847.
16. Antolovich, S. D., "Fracture Toughness and Strain-Induced Phase Transformation", Trans. TMS-AIME, Vol. 242, 1968, pp. 2371.
17. Antolovich, S. D., and Singh, B., " On the Toughness Increment Associated with Martensite Phase Transformation in TRIP Steels", Met. Trans., vol. 2., 1971, pp.2135.
18. Parker, E. R., and D, Zackay, V. F., "Enhancement of Fracture Toughness in High Strength Steel by Microstructure Control", Eng. Fract. Mech., Vol. 5, 1973, pp. 147.
19. Birat, J. B., and Gerberich, W. W., "A Metastable Austenite with Plans-Stress Fracture Toughness Near 500,000 $lb/in^2\text{-}in^{1/2}$", Int. J. Fract. Mech. Vol. 7, 1971, pp. 108.
20. Chanani, G. R., Antolovich, S. D., and Gerberich, W. W., "Fatigue Propergation in TRIP Steels", Met. Trans., Vol. 3, 1972, pp. 2661.
21. Pineau, A. G. and Pelloux, R. M., "Influence of Strain-Induced Martensitic Transformation on Fatigue Crack Growth Rate in Stainless Steels", Met. Trans., Vol. 5, 1974, pp. 1103.
22. Olson, G. B., Chait, R., Arzin, M., and Cagne, R. A., " Fatigue Strength of TRIP Steels", Met. Trans., Vol. 11A, 1980, pp. 1069.
23. Pati, S. R., and Cohen, M., "Nucleation of the Isothermal Martensitic Transformation", Acta Met. 17, 1969, pp.189.
24. Raghavan, V., and and Cohen, M., "Measurement and Interpretation of Isothermal Martensitic Kinetics", Met. Trans., Vol. 2, 1971, pp. 2409.
25. Patel, J. R., and Cohen, M., "Criterion for the Action of Applied Stress in the Martensitic Transformation", Acta Met. Vol. 1, 1953, pp.531.
26. Olson, G. B., and Cohen, M., "Stress-Assisted Isothermal Martensitic Transformation : Application to TRIP Steels", Met. Trans. Vol. 13A, 1982, pp. 1907.
27. Angel, T., J. of Iron Stel Inst., vol. 177, 1954, pp. 165.

28. Gerberich, W. W., Thomas, G., Parker, E. R., and D, Zackay, V. F., "Metastable Austenite : Decomposition and Strength", in in Pro. Second Conf. on the Strength of Metals and Alloys, Asilomar, CA, 1970, pp.900.
29. Olson, G. B., and Cohen, M., "Kinetics of Strain-Induced Martensitic Transformation", Met. Trans., Vol. 6A, 1975, pp. 791.
30. Narutani, T., Olson, G. B., Cohen, M., "Constitutive Flow Relations for Austenite Steels During Strain-Induced Martensitic Transformation", J. Phsique, vol.43, 1982, pp.C4-429.
31. Brown, F. M., and Stobbs, W. M., "The Work-Hardening of Copper-Silica - The Role of Plastic Relaxation", Phil. Mag. 23, 1971, pp.1201.
32. Gurland, J., and Plateau, J.,"The Mechanism of Ductile Rupture of Metals Containing Inclusions", Trans. ASM, Vol. 56, 1963, pp.442.
33. McClintock, F. A., " On the Mechanics of Fracture from Inclusions", in Dcutility., ASM, 1968, pp. 255.
34. Goods, S. H., and Brown, L. M., "The Nucleation of Cavities by Plastic Deformation", Acta Met.,vol. 27, 1979, pp. 1.
35. Argon, A. S., Im, J., and Safoglu, R.,"Cavity Formation from Inclusions in Ductile Fracture", Met.Trans., Vol. 5A, 1975, pp.825.
36. Argon, A. S., and Im, J.,"Separation of Second Phase Particles in Spheroidized 1045 Steels, Cu-0.6Pct Cr Alloys, and Maraging Steel in Plastic Straining", Met. Trans., Vol.6A, 1975, pp. 839.
37. Ashby, M. F., Phil. Mag. Vol. 14, 1966, pp.1157.
38. McClintock, F. A., "A Criterion for Ductile Fracture by the Growth of Holes", J. Appl. Mech. Vol. 35, 1968, pp. 363.
39. Rice, J. R., and Tracy, D. M., " On the Ductile Enlargement of Voids in Triaxial Stress Fields", J. Mech. Phys. Solids., Vol. 17, 1969, pp. 201.
40. Tracy, D. M., "Strain-Hardening and Interaction Effects on the Growth of Voids in Ductile Fracture", Eng. Fract. Mech., Vol. 3, 1971, pp.301.
41. Knott, J. F., "Micromechanisms of Fibrous Crack Extension in Engineering Alloy", Mat. Sci., Vol. 14, 1980, pp. 237.
42. Clayton, J. C., and Knott, J. F., "Observations of Fibrous Fracture Modes in a Prestrained Low- Alloy Sreel", Mat. Sci., Vol. 10, 1976, pp. 63.
43. Rice, J. R., and Johnson, M. A., "The Role of Large Crack Tip Geometry Changes in Plane Strain Fracture", in Elastic Behavior of Solids, Ed. M. F. Kanninen et al. McGraw-Hill, New York, 1970, pp. 641.

44. Cox, T. B., and Low, J. R., "An Investigation of the Plastic Fracture of AISI4340 and 18Nickel -200 Grade Maraging Steels" Met. Trans., Vol. 5,1974, pp. 1457.
45. Beachem, C. D., and Yode G. R., "Elastic-Plastic Fracture by Homogeneous Microvoid Coalscence Tearing Along Alternating Shear Planes", Met. Trans. Vol. 4, 1973, pp. 1145.
46. Rice, J. R., " The Localization of Plastic Deformation", Proc. 14th Int. Cong. on Theoretical and Applied Mechanics, Ed. W. T. Koiter, North-Holland Pub. Co., 1976, pp. 207.
47. Needleman, A., and Rice, J. R., "Limits to Ductility Set by Plastic Flow Localization", in Mechanics of Metal Sheet Forming, Ed. D. P. Koistinen and N. W. Wang, Plenum Publ. Co., 1978, pp. 237.
48. Saje, M., Pan, J., and Needleman, A., "Void Nucleation Effects on Shear Localization in Plastic Solids", Int. J. Fract. Vol. 19, 1982, pp. 163.
49. Pan, J., Saje, M., and Needleman, A., " Localization of Deformation in Rate Sensitive Porous Plastic Solids", Int. J. Fract. Vol. 21, 1983, pp. 261.
50. Tvergaard, "Influence of Voids on Shear-band Instability Under Plain Strain Conditions" Int. J. Fract. Vol. 17, 1981, pp. 389.
51. Gurson, A. L., " Continuum Theory of Ductile Rupture by Void Nucleation and Growth", J. Eng. Mat. and Tech., Trans. ASME. 99, 1977, pp. 2.
52. Aravas, N, and McMeeking, R. M., J. Mech. Phys. Solids, Vol. 33, 1985, pp.1.
53. Garrison, W. M., Jr., and Handerhan, K. J., "Fracture Toughness : Particle-Dispersion Correlations", Department of Metallurgical Engineering and Materials Science, Carnegie Mellon University (to be published).
54. Olson, G. B., Private Communication.
55. Cox, A. R., Moore, J. B., and Van Reuth, E. C., "On the Rapid Solidification of Superalloys.", in The Proceedings of the Third International Symposium on Superalloys, Clator's, Baton Rouge, 1976.
56. Kear, B. H., Holiday, P. R., and Cox, A. R., "On the Microstructure of Rapidly Solidified IN-100 Powdwers.", Met. Trans., Vol. 10A, 1979, pp.191.
57. Watton, J. F.," Phosphorus Gettering in a Rapidly Solidified Ni-Mo-La Steel.", Ph. D. Thesis, M.I.T., 1987.
58. Libera, M. R., "Solidification Structures in Rapidly Solidified Powders of an Iron-Chromium-Nickel Alloy.", M. S. Thesis, M.I.T., 1982.
59. Libera, M. R., "Heterogeneous Crystal Nucleation in Atomized Iron-Nickel Droplets.", Ph. D. Thesis, M.I.T., 1987.

60. Grant, N. J., "A Review of Various Atomization Processes.", in Rapid Solidification Processing Principles and Technologies, Ed. by Mehrabian, R., Kear, B. H., and Cohen, M., Clator's, Bator Rouge, 1978.
61. Olson, G. B., "Transformation Plasticity and the Stability of Plastic Flow." in ASM Materials Science Seminar : Deformation, Processing, and Structure., 1982.
62. Clark, G. A., Andrews, W. R., Paris, P. C., and Schmidt, D. W., "Single Specimen Tests for J_{Ic} Determination.", ASTM STP 590, 1976, pp. 27.
63. Willoughby, A. A., and Garwood, S. J., "On the Unloading Compliance Method of Deriving Single-Specimen R-curves in Three-Point Bending.", ASTM STP 803, Vol. II, 1983, pp. 372.
64. Faucher, B., Tyson, W. R.; "A Comparison of Crack-Mouth Opening and Load-Line Displacement for J-Integral Evaluation Using Bend Specimen." ASTM STP 856, 1985, pp.278.
65. Albrecht, P., Andrews, W. R., Gudas, I. P., Joyce, J. A., Loss, F. J., McCabe, D. E., Schmidt, D. W., and VanDerSluy, W. A., "Tentative Test Procedure for Determining the Plane Strain J_I-R Curve.", Journal of Testing and Evaluayion, Vol. 10, No. 6, 1982, pp. 245.
66. Clark, G. A., "Single Specimen Test for J_{Ic} Determination -- Revisited", ASTM STP 743, 1981, pp. 553.
67. Tada, H., Paris, P. C., and Irwin, G. R., in The Stress Analysis of Crack Analysis, Del Research Corporation, PA., 1973.
68. Bucci, R. J., Paris, P. C., Lander, J. D., and Rice, J. R., "J Integral Estimation Procedures", ASTM STP 514, 1972, pp. 40.
69. Rice, J. R., Paris, P. C., and Merkle, J. G., ASTM STP 536, 1973, pp.231.
70. Dieter, G. E., in Mechanical Metallurgy, 2nd Ed. 1976, pp. 545.
71. Mangonon, P. L. Jr., and Thomas, G., "Structure and Properties of Thermal-Mechanically Treated 304 Stainless Steel", Met. Trans. Vol.1, 1970, pp.1587.
72. Hecker, S. S., Stout, M. G., Staudhammer, K. P., and Smith, J. L., "Effect of Strain Rate and Strain State on Deformation Induced Transformation in 304 Stainless Steel : Part I. Magnetic Measurements and Mechanical Behavior", Met. Trans. Vol. 13A, 1982, pp.619.
73. Porter, D. A., and Easteling, K. E., in Phase Transformation in Metals and Alloys,1981, Pub. by Van Nostrand Reinhold Co. Ltd., pp.303-308.
74. Hsu, C. Y., "Grain-Growth Mechanisms in Rapidly Solidified Matrix Steels", Ph.D. Thesis, 1984, M.I.T., Cambridge, MA.

75. Olson, G. B., Ling, H. C., Montgomery, J. S., Vander Sande, J. B., and Cohen, M., "Grain-Coarsenong Resistance and the Stabolity of Second-Phase Dispersions in Rapidly Solidified Steels", Rapidly Solidified Amorphous and Crystalline Alloys, North-Holland, NY, 1982,pp. 355.
76. Hancock, J. W., and Mackenzie, A. C., "On the Mechanisms of Ductile Failure in High-Strength Steels Subjected To Multi-Axial Stress-States", J. Mech. Phys. Solid, Vol.24. 1976, pp.146.
77. Bridgman, P. W., Trans. Am. Soc. Met., Vol. 32, 1944, pp.553.
78. Strinsfellow, R., Doctoral Research in Progress, MIT
79. Kaufman, L. Manlab-N.P.L. Thermochemical Databanks, Manlab, Inc., Cambridge, MA, 1980.
80. Olson, G. B., and Cohen, M., "Dislocation Theory of Martensitic Transformation", in Dislocation in Solids, Ed. F. R. N. Nabarro, North-Holland, 1986. pp. 380
81. Korenko, M. K., "Martensitic Transformation in High Magnetic Fields", Sc. D. Thesis, MIT, 1973.
82.. Olson, G. B., Tsuzaki, K., and Cohen, M., "Statistical Aspects of Martensitic Nucleation", in Mat. Res. Soc. Symp. Proc., Vol. 57, 1987, pp.129.
83. Backofen, W. A., "Deformation Processing", Addison Wesley Publishing Co., Inc. 1972, pp. 250-261.
84. Haezebrouk, D. M., Research in Progress, MIT, 1988.
85. McMeeking, R. M., and Parks, D. M., "On Criteria for J Dominance od Crack-Tip Fields in Large Scale Yielding", in Elastic-Plastic Fracture, ASTM STP 668, 1979, pp. 175.
86. Paris, P. C., Tada, H., Zahoor, A., and Ernst, H., "Instability of the Tearing Mode of Elastic-Plastic Crack Growth", in Elastic-Plastic Fracture, ASTM STP 668, 1979, pp. 5.
87. Hutchinson, J. W., and Paris, P. C., "The Theory of Stability Analysis of J-Controlled Crack Growth", in Elastic-Plastic Fracture, ASTM STP 668, 1979, pp. 375.
88. Van Den Avyle, J. A., "Correlation of Fractography, Microstructure and Fracture Toughness Behavior of High Strength Alloys", Ph. D. Thesis, Department of Materials Science and Engineering, MIT, 1975.
89. Backofen, W. A., "Deformation Processing", Addison Wesley Publishing Co., Inc. 1972, pp.201.

90. Argon, A. S., and Needleman, A.,"Distribution of Plastic Strain and Negative Pressure in Necked Steel and Copper Bars", Met. Trans. Vol.6A, 1975, pp. 815.
91. Shea, M. M., and Sachdev, A. K., "Influence of Strain Rate on the Mechanical Behavior of a High Carbon Iron-Nickel Austenite", Scr. Met., Vol.18, 1984, pp.1181.

Biographical Note

The author was born on April 18, 1953 in Tainan, Taiwan, R.O.C.. He was raised at the same city. At age 18, he began college education in National Taiwan University, Taipei, and graduated in 1975 with the degree of Bachelor of Science in Mechanical Engineering. He continued his graduate study in the same university and received the degree of Master of Science in Materials Science in 1977. He then joined the Chun-Shan Institute of Science and Technology as an assistant scientist, making numerous contributions in the research projects concerning the property-structure-process relationships of metallic materials, ultrahigh strength steels and nickle-base superalloys in particular. He married Mara Chiang, a skillful English-Chinese translator and also an expert in Chinese food, in 1978. They have two lovely sons, Chian (8) and Chikuang (5). Since1984, he has been sponsored by the Institute in pursuit of the doctorate in metallurgy at M.I.T..